

Synchronized Memory-Dependent Intracellular Oscillations for a Cell-Bulk ODE-PDE Model in \mathbb{R}^2

Merlin Pelz*

Michael J. Ward*[†]

September 4, 2024

Abstract

For a cell-bulk ODE-PDE model in \mathbb{R}^2 , a hybrid asymptotic-numerical theory is developed to provide a new theoretical and computationally efficient approach for studying how oscillatory dynamics associated with spatially segregated dynamically active “units” or “cells” are regulated by a PDE bulk diffusion field that is both produced and absorbed by the entire cell population. The study of oscillator synchronization in a PDE diffusion field was one of the initial aims of Yoshiki Kuramoto’s foundational work. For this cell-bulk model, strong localized perturbation theory, as extended to a time-dependent setting, is used to derive a new integro-differential ODE system that characterizes intracellular dynamics in a memory-dependent bulk-diffusion field. For this nonlocal reduced system, a novel fast time-marching scheme, relying in part on the *sum-of-exponentials method* to numerically treat convolution integrals, is developed to rapidly and accurately compute numerical solutions to the integro-differential system over long time intervals. For the special case of Sel’kov reaction kinetics, a wide variety of large-scale oscillatory dynamical behavior including phase synchronization, mixed-mode oscillations, and quorum-sensing are illustrated for various ranges of the influx and efflux permeability parameters, the bulk degradation rate and bulk diffusivity, and the specific spatial configuration of cells. Results from our fast algorithm, obtained in under one minute of CPU time on a laptop, are benchmarked against PDE simulations of the cell-bulk model, which are performed with a commercial PDE solver, that have run-times that are orders of magnitude larger.

1 Introduction

Over the past four decades, the Kuramoto model [35]

$$\dot{\theta}_i = \omega_i + \frac{K}{N} \sum_{j=1}^N \sin(\theta_j - \theta_i), \quad (1.1)$$

and its variants have provided the primary theoretical modeling framework for analyzing the synchronization properties of a collection of N nonlinear oscillators. In (1.1), θ_i is the phase of the i^{th} oscillator, ω_i is its natural frequency, and K is the coupling strength. Key quantities for analyzing the synchronization behavior for (1.1) are the Kuramoto order parameters $r(t)$ and $\psi(t)$ defined by $re^{i\psi} = N^{-1} \sum_{j=1}^N e^{i\theta_j}$. In the mean field limit $N \rightarrow \infty$, phase transitions to complete phase synchronization $r = 1$ as K is increased above a threshold have been characterized. For a survey of results see [64], [2] and [12].

One key aspect of Kuramoto-type phase oscillator systems is that they can be formally derived from nonlinear dynamical systems of coupled oscillators by using asymptotic phase reduction methods that are valid in the limit of weak coupling (cf. [49], [39] and [38]). An important current research theme is the study of oscillator synchronization on networks, as surveyed in [56], owing to their many diverse applications such as power grids [27] and cortical brain activity [10], among others.

*Dept. of Mathematics, Univ. of British Columbia, Vancouver, B.C., Canada.

[†]corresponding author, ward@math.ubc.ca

With the aim of incorporating diffusive effects, in [37] Kuramoto emphasized the need for characterizing synchronization behavior for a collection of coupled oscillators or “cells”, each fixed in space, in which an extra substance secreted from each cell can diffuse over the entire space and effectively mediate the inter-cell interaction. His phenomenological model in [37] of this interaction has the form

$$\mathbf{u}'_j = \mathbf{F}(\mathbf{u}_j) + \mathbf{g}(A(\mathbf{x}_j, t)), \quad \varepsilon A_t = D\Delta A - \eta A + \sum_{k=1}^N h(\mathbf{u}_k)\delta(\mathbf{x} - \mathbf{x}_k), \quad (1.2)$$

where \mathbf{g} and h are prescribed coupling functions. For $\mathbf{x} \in \mathbb{R}^1$ and in the limit $\varepsilon \rightarrow 0$, (1.2) reduces to

$$\mathbf{u}'_j = \mathbf{F}(\mathbf{u}_j) + \mathbf{g}\left(\sum_{k=1}^N \sigma(|\mathbf{x}_j - \mathbf{x}_k|)h(\mathbf{u}_k)\right). \quad (1.3)$$

where $\sigma(r) = Ce^{-r\sqrt{\eta/D}}$ is the 1-D quasi-static Green’s function for some $C > 0$. Further approximating (1.3) near a Hopf bifurcation point of the uncoupled dynamics $\mathbf{u}'_j = \mathbf{F}(\mathbf{u}_j)$ by using a weakly nonlinear analysis, the normal form of the underlying dynamics leads to a nonlocally coupled Complex Ginzburg-Landau (CGL) system. These nonlocal CGLs yield a wide variety of highly intricate spatio-temporal dynamics, commonly known as *chemical turbulence* ([36], [37], [48]). More recently, in a series of articles ([63], [4] and [11]) there has been a renewed focus on analyzing synchronization properties for phase oscillator systems with coupling as in (1.2), with the main emphasis being for the $\varepsilon \rightarrow 0$ limit (1.3).

Two primary limitations of the phenomenological model (1.2) is that $A(\mathbf{x}, t)$ has a singularity at $\mathbf{x} = \mathbf{x}_j$ in \mathbb{R}^2 and \mathbb{R}^3 , and that it is not clear how to choose the coupling functions g and h for a specific application. For many problems in biology and chemical physics, it is essential to *explicitly* model the diffusive coupling of dynamically active units, without incorporating extraneous coupling functions. In particular, for many microbial systems, cell-cell communication occurs through the diffusion of extracellular signaling molecules, referred to as autoinducers, that are both produced and absorbed by the entire collection of cells (cf. [17], [67], [14]). For a colony of *Dictyostelium discoideum*, it is known that the autoinducer cyclic adenosine monophosphate (cAMP) triggers intracellular oscillations that initiate the process of the spatial aggregation of the colony in low nutrient environments (cf. [26], [50], [19]). In addition, the autoinducer acetaldehyde (Ace) leads to glycolytic oscillations in a colony of yeast cells (cf. [13], [14], [15], [29]), while acylated homoserine lactones (AHLs) are implicated in triggering bioluminescence behavior associated with the marine bacterium *Aliivibrio fischeri* that resides in the light organ of certain species of tropical squid (cf. [67]). For these microbial systems, one key aspect is to characterize quorum-sensing behavior, whereby collective dynamics can only occur if the cell population exceeds a threshold (cf. [60], see [55] for a survey). In a chemical physics context, collective oscillatory dynamics of catalyst loaded pellets can occur owing to the diffusive coupling of Belousov-Zhabotinsky (BZ) reagents in a chemical mixture (cf. [62], [69], [68], [71], [70]). In addition, certain microemulsions of dynamically active surface-stabilized BZ droplets that are immersed in oil lead to synchronized oscillatory dynamics (cf. [72]). More recently, chaotic oscillations have been observed for a compartmentalized surface reaction nanosystem [57].

An ideal modeling framework to investigate collective dynamics arising from the coupling of a bulk diffusion field are the cell-bulk models originating from [46] and [47] in a 3-D setting and from [24] and [33] in 2-D domains. From a mathematical viewpoint, cell-bulk models are compartmental-reaction diffusion (RD) systems with rich dynamics that can be used for analyzing how intracellular oscillations associated with spatially segregated dynamically active “units” or “cells” are mediated by one or more diffusing substances that are both produced and absorbed by the entire cell population. This modeling framework is also well-aligned with Kuramoto’s original aims of investigating oscillator synchronization through the effect of diffusive coupling as discussed in [37]. The survey article [62] has also emphasized the need for theoretical modeling frameworks that couple discretely interacting dynamical units.

Previous studies of synchronization or pattern-forming properties of cell-bulk systems, i.e., systems that involve a cell membrane connected to a diffusion field (the bulk), include the 1-D analysis in

[21] with oscillatory FitzHugh-Nagumo kinetics on the diffusively coupled boundaries and the bulk-membrane analysis of [40] in disk-shaped domains. In a 1-D context, and with one bulk diffusing species, this compartmental-RD system modeling paradigm has been shown to lead to triggered oscillatory instabilities for various reaction kinetics involving conditional oscillators (cf. [23], [25], [22]). Amplitude equations characterizing the local branching behavior for these triggered oscillations have been derived in [52] using a weakly nonlinear analysis. Extensions of this framework incorporating time-delay effects have been used to model intracellular polarization and oscillations in fission yeast (cf. [76]). In a 2-D domain, cell-bulk models with one diffusing bulk species have been formulated and used to model quorum-sensing behavior (cf. [24], [33], [59], [20]). In a 2-D bounded domain with no-flux boundary conditions, and in the limit of large bulk diffusivity and small cell radii, the study of intracellular dynamics for cell-bulk models can be asymptotically reduced to the study of an ODE system with global coupling (cf. [33], [32]), where the global mode arises from the approximately spatially uniform bulk diffusion field. With two-bulk diffusing species, and as inspired by the trans-membrane signal transduction study in [58], in 1-D [53] and in 2-D [54] domains it has been shown that a symmetry-breaking bifurcation leading to a linearly stable asymmetric pattern can occur for equal bulk diffusivities when the ratio of reaction rates across the cell boundaries for the two bulk species is sufficiently large.

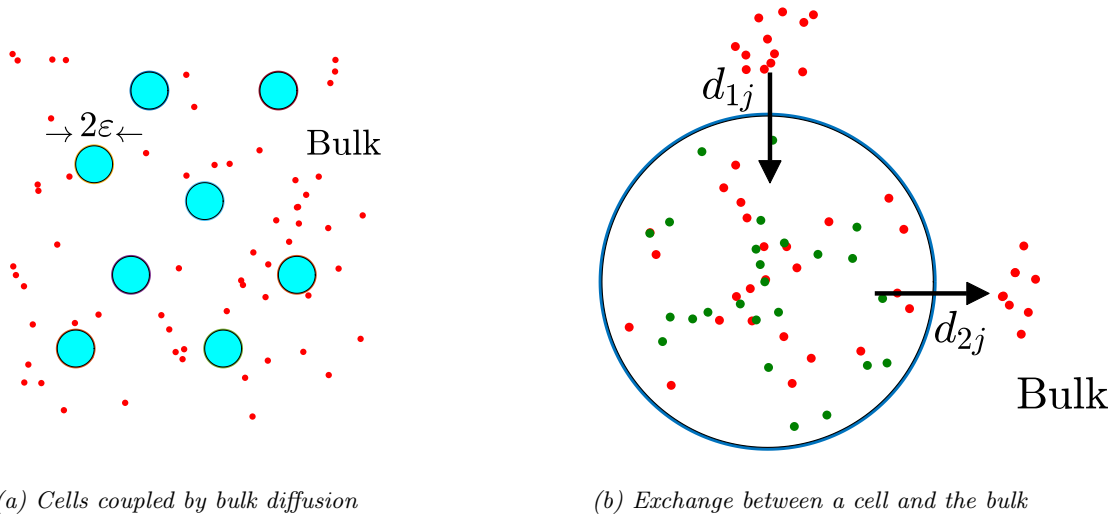


Figure 1: Left: Dynamically active circular signaling compartments (in cyan) coupled through a bulk diffusion field (red dots) in \mathbb{R}^2 . Right: Zoom of the chemical exchange between the bulk and any given cell when there are two intracellular species (green and red dots). Only the red species is secreted into the extracellular bulk region, while the bulk species can bind to the cell membrane. A Robin boundary condition models this chemical exchange.

We now formulate the coupled dimensional cell-bulk ODE-PDE model of [24] and [33], as inspired by [46] and [47], with one bulk species in \mathbb{R}^2 . We assume that there are N dynamically active cells, modeled by a collection of disks of a common radius R_0 , denoted by Ω_j and centered at $\mathbf{x}_j \in \mathbb{R}^2$ for $j \in \{1, \dots, N\}$. In the bulk, or extracellular, region $\mathbb{R}^2 \setminus \cup_{j=1}^N \Omega_j$, the concentration $\mathcal{U}(\mathbf{X}, T)$ of the autoinducer or bulk signal, with diffusivity D_B and bulk degradation k_B , is assumed to satisfy

$$\partial_T \mathcal{U} = D_B \Delta \mathcal{U} - k_B \mathcal{U}, \quad T > 0, \quad \mathbf{X} \in \mathbb{R}^2 \setminus \cup_{j=1}^N \Omega_j, \quad (1.4a)$$

$$D_B \partial_{n_{\mathbf{x}}} \mathcal{U} = \beta_{1j} \mathcal{U} - \beta_{2j} \mu_{1j}, \quad \mathbf{x} \in \partial \Omega_j, \quad j \in \{1, \dots, N\}. \quad (1.4b)$$

The permeabilities $\beta_{1j} > 0$ and $\beta_{2j} > 0$ control the influx and efflux into and out of the j^{th} cell, respectively, while $\partial_{n_{\mathbf{x}}}$ is the outer normal derivative pointing into the bulk region.

Inside each cell we assume that there are m species $\mu_j \equiv (\mu_{1j}, \dots, \mu_{mj})^T$ that undergo interactions with the local reaction kinetics \mathbf{F}_j , and that one species, labeled by μ_{1j} , can permeate across the cell boundary. The cells are assumed to be sufficiently small so that we can neglect any spatial gradients in the intracellular species within each cell. The intracellular dynamics in the j^{th} cell are coupled to the

bulk diffusion field (1.4) via an integration of the diffusive flux across the cell membrane as

$$\frac{d\mu_j}{dT} = k_R \mu_c \mathbf{F}_j(\mu_j/\mu_c) + \mathbf{e}_1 \int_{\partial\Omega_j} (\beta_{1j} \mathcal{U} - \beta_{2j} \mu_{1j}) dS_{\mathbf{x}}, \quad j \in \{1, \dots, N\}. \quad (1.4c)$$

In (1.4c), $\mathbf{e}_1 \equiv (1, 0, \dots, 0)^T$, $k_R > 0$ is the dimensional intracellular reaction rate and $\mu_c > 0$ is a typical magnitude of the vector μ_j . In this formulation, μ_{1j} can permeate the cell membrane with an efflux rate β_{2j} per unit length. The influx rate β_{1j} controls the feedback into the j^{th} cell from the global bulk diffusion field that is produced by the entire collection of spatially segregated cells.

For our asymptotic limit, we will assume that the common radius R_0 of the signaling compartments is small relative to the minimum inter-cell separation distance L , and so we introduce a small parameter $\varepsilon \equiv R_0/L \ll 1$. From the non-dimensionalization of the cell-bulk model (1.4) given in Appendix A we obtain that the dimensionless bulk field $U(\mathbf{x}, t)$ satisfies (see Fig. 1 for a schematic)

$$\partial_t U = D \Delta U - \sigma U, \quad t > 0, \quad \mathbf{x} \in \mathbb{R}^2 \setminus \cup_{j=1}^N \Omega_{\varepsilon_j}; \quad U(\mathbf{x}, 0) = 0, \quad (1.5a)$$

$$\varepsilon D \partial_n U = d_{1j} U - d_{2j} u_{1j}, \quad \mathbf{x} \in \partial\Omega_{\varepsilon_j}, \quad j \in \{1, \dots, N\}, \quad (1.5b)$$

which is coupled to the dimensionless intracellular dynamics within the j^{th} cell by

$$\frac{d\mathbf{u}_j}{dt} = \mathbf{F}_j(\mathbf{u}_j) + \frac{\mathbf{e}_1}{\varepsilon} \int_{\partial\Omega_{\varepsilon_j}} (d_{1j} U - d_{2j} u_{1j}) dS_{\mathbf{x}}, \quad j \in \{1, \dots, N\}. \quad (1.5c)$$

Here $\mathbf{u}_j = (u_{1j}, \dots, u_{mj})^T$ is the dimensionless vector of intracellular species in the j^{th} cell, labeled by $\Omega_{\varepsilon_j} \equiv \{\mathbf{x} \mid |\mathbf{x} - \mathbf{x}_j| \leq \varepsilon\}$. We assume that the centers of the cells are well-separated in the sense that $\text{dist}(\mathbf{x}_j, \mathbf{x}_k) = \mathcal{O}(1)$ for $j \neq k$. In (1.5), the key dimensionless parameters are

$$D \equiv \frac{D_B}{k_R L^2}, \quad d_{1j} \equiv \varepsilon \frac{\beta_{1j}}{k_R L} = \mathcal{O}(1), \quad d_{2j} \equiv \varepsilon \frac{\beta_{2j} L}{k_R} = \mathcal{O}(1), \quad \sigma \equiv \frac{k_B}{k_R}. \quad (1.6)$$

Here D and σ are the effective bulk diffusivity and bulk degradation rate. In (1.6), the ratios $\beta_{1j}/(k_R L)$ and $\beta_{2j} L/k_R$ are chosen as $\mathcal{O}(\varepsilon^{-1})$ so that there is an $\mathcal{O}(1)$ transport across the cell membrane.

Our goal for the conceptual cell-bulk model (1.5) is to develop a hybrid asymptotic-numerical approach to study how intracellular oscillations are both initiated and synchronized by the bulk diffusion field that is created by the entire collection of cells. In contrast to the study in [33] that focused only on the steady-state problem and the spectral properties of the linearization of the steady-state, the main goal in this paper is to use a hybrid approach to study the *large-scale* intracellular dynamics for (1.5) that occur away from stable steady-states.

In §3 we will extend the strong localized perturbation theory, as surveyed in [74], to the time-dependent setting of (1.5) in order to derive, in the limit $\varepsilon \rightarrow 0$ of small cell radii, a new integro-differential ODE system that characterizes how intracellular dynamics are coupled to the bulk diffusion field that is produced by the entire cell population. This reduced integro-differential system, as described in Proposition 1, is asymptotically accurate to all orders in $\nu = -1/\log \varepsilon$. As discussed in Remark 1 below, the “outer problem” in our analysis shares some common features with Kuramoto’s original model (1.2).

Assuming that $U(\mathbf{x}, 0) = 0$, in §2 we analyze the short-time behavior of the cell-bulk system on the time-scale $\tau = \varepsilon^2 t$ within an $\mathcal{O}(\varepsilon)$ neighborhood of each cell. This transient solution, involving Ramanujan’s integral, is essential for providing the initial behavior for the integro-differential ODE system in Proposition 1 that is valid on the $\mathcal{O}(1)$ time-scale. In §4, we show that the steady-states of the cell-bulk model (1.5), as obtained from strong localized perturbation theory, coincide with the steady-state limiting values of the integro-differential ODE system. In addition, the linear stability properties of the steady-states are shown to be characterized by the roots of a nonlinear matrix eigenvalue problem, referred to as the globally coupled eigenvalue problem (GCEP).

We emphasize that a direct numerical study of the integro-differential system in Proposition 1 is highly challenging owing to the fact that $N(N+1)/2$ memory-dependent convolution integrals, each with integrable singularities, would have to be computed numerically up to time t in order to advance the solution one time step to time $t + \Delta t$. To overcome this difficulty, in §5 we develop a fast time-marching numerical scheme, which relies significantly on the *sum-of-exponentials* method of [34] and [7] (see also [8]) together with Duhamel’s principle, that allows us to both rapidly and accurately compute solutions to the integro-differential system for arbitrary reaction kinetics over long time intervals.

In §6 we illustrate our hybrid asymptotic-numerical theory for the choice of Sel’kov reaction dynamics, which have been used previously in simple models of glycolysis oscillations (cf. [50], [61]). With Sel’kov kinetics the steady-state solution branches of (1.5) have no transcritical or fold bifurcations and, as a result, steady-states are destabilized only via Hopf bifurcations. For various specific spatial configurations of cells, phase diagrams in the $1/\sigma$ versus D parameter plane, as computed from the winding-number of the determinant of the nonlinear matrix eigenvalue problem, are provided to identify the number of destabilizing modes of the linearization of the steady-state. The corresponding eigenvector of the GCEP is shown to encode both the relative magnitude of the signaling gradient near each cell, as well as the phase shift in small amplitude oscillations between cells that occur near an unstable steady-state. Quorum-sensing and diffusion-sensing behavior, as well as the key effects on intracellular oscillations of varying the influx and efflux permeabilities, are examined for various spatial configurations of cells. In particular, we show that a single oscillating cell can trigger coherent intracellular oscillations in an entire collection of cells. Moreover, by computing the Kuramoto order parameter, we show an apparent phase transition to complete phase coherence as the bulk diffusivity is increased for a one-shell hexagonal arrangement of identical cells. These cells would be in a quiescent state without any cell-bulk coupling. Finally, in §7 we discuss several related cell-bulk problems that are now tractable to study with our hybrid approach.

2 Transient analysis near the cells

We first analyze the transient solution near the j^{th} cell, which is valid for $t = \mathcal{O}(\varepsilon^2)$ when $U(\mathbf{x}, 0) = 0$ and for arbitrary initial values $\mathbf{u}_j(0)$ for $j \in \{1, \dots, N\}$. This short-time analysis will provide the initial conditions for the long-time dynamics studied in §3.

We first assume that $u_{1j}(0) \neq 0$. In the j^{th} inner region we let $\mathbf{y} = \varepsilon^{-1}(\mathbf{x} - \mathbf{x}_j)$ with $\rho = |\mathbf{y}|$ and we introduce the short time-scale τ , defined by $t = \varepsilon^2\tau$. From (1.5a) and (1.5b), we obtain that $V(\rho, \tau) = U(\mathbf{x}_j + \varepsilon\mathbf{y}, \varepsilon^2\tau)$ satisfies, to leading-order, the local problem

$$\begin{aligned} \partial_\tau V &= D \left(\partial_{\rho\rho} V + \frac{1}{\rho} \partial_\rho V \right), \quad \rho > 1, \quad \tau \geq 0; \quad V(\rho, 0) = 0, \\ D\partial_\rho V &= d_{1j}V - d_{2j}u_{1j}(0), \quad \text{on } \rho = 1. \end{aligned} \tag{2.7}$$

By taking the Laplace transform of (2.7), we calculate $\hat{V}(\rho, s) = \mathcal{L}[V(\rho, \tau)] \equiv \int_0^\infty V(\rho, \tau)e^{-s\tau}d\tau$ as

$$\hat{V}(\rho, s) = u_{1j}(0) \frac{d_{2j}}{s} \left(\frac{K_0(\rho\sqrt{s/D})}{d_{1j}K_0(\sqrt{s/D}) + \sqrt{sD}K_1(\sqrt{s/D})} \right), \tag{2.8}$$

where the branch cut is taken along $\text{Re}(s) \leq 0$ with $\text{Im}(s) = 0$. Here $K_0(z)$ and $K_1(z)$ are modified Bessel functions of the second kind.

Since the singularity of (2.8) with the largest real part is at $s = 0$, to determine the large τ behavior of V for fixed $\rho > 1$ we must first determine the behavior of (2.8) as $s \rightarrow 0$. Upon using $K_0(z) \sim -\log z - \gamma_e + \log 2 + o(1)$ and $K_1(z) \sim z^{-1} + o(1)$ as $z \rightarrow 0$, where γ_e is Euler’s constant, we get

$$\hat{V}(\rho, s) \sim \frac{d_{2j}u_{1j}(0)}{d_{1j}s} + \frac{2d_{2j}u_{1j}(0)}{d_{1j}} \left(\log \rho + \frac{D}{d_{1j}} \right) \frac{1}{s \log(\kappa_{0j}s)}, \quad \text{as } s \rightarrow 0, \tag{2.9a}$$

where κ_{0j} is defined by

$$\kappa_{0j} \equiv \frac{1}{4D} e^{2(\gamma_e - D/d_{1j})}. \quad (2.9b)$$

To determine $V(\rho, \tau)$ for $\tau \gg 1$ and $\rho = \mathcal{O}(1)$, we must determine a function whose Laplace transform is analytic in $\text{Re}(s) > 0$ and where its singularity with the largest real part occurs at $s = 0$ with the leading-order local behavior $[s \log(\kappa_{0j}s)]^{-1}$ as $s \rightarrow 0$. We emphasize that $\hat{V}(\rho, s)$ in (2.8) is analytic in $\text{Re}(s) > 0$, and that the pole at $s = 1/\kappa_{0j}$ in the local behavior as $s \rightarrow 0$ in (2.9a) is spurious. As shown in [41], and summarized in Appendix B, for any $\kappa_{0j} > 0$ we have the exact relation

$$\mathcal{L}[N(\tau/\kappa_{0j})] = \frac{1}{s - 1/\kappa_{0j}} - \frac{1}{s \log(s\kappa_{0j})}, \quad (2.10)$$

where $N(x)$ for $x > 0$ is Ramanujan's integral defined by

$$N(x) \equiv \int_0^\infty \frac{e^{-x\xi}}{\xi [\pi^2 + (\log \xi)^2]} d\xi. \quad (2.11)$$

It is readily shown that $s = 1/\kappa_{0j}$ is a removable singularity for (2.10) and that $\mathcal{L}[N(\tau/\kappa_{0j})]$ is analytic in $\text{Re}(s) > 0$ and the singularity with the largest real part satisfies $\mathcal{L}[N(\tau/\kappa_{0j})] \sim -[s \log(s\kappa_{0j})^{-1}] + \mathcal{O}(1)$ as $s \rightarrow 0$. By using the well-known integral asymptotics (cf. [75], [9], [41])

$$N(x) \sim \frac{1}{\log x} - \frac{\gamma_e}{(\log x)^2} + \mathcal{O}((\log x)^{-3}), \quad \text{as } x \rightarrow +\infty, \quad (2.12)$$

where γ_e is Euler's constant, we absorb the second term into the leading-order approximation to obtain

$$N(x) \sim \frac{1}{\log(xe^{\gamma_e})} - \mathcal{O}([\log(xe^{\gamma_e})]^{-3}), \quad \text{as } x \rightarrow +\infty. \quad (2.13)$$

By using this result and (2.9b), we readily obtain for $\tau \gg 1$ and $\rho > 1$ fixed that

$$V(\rho, \tau) \sim u_{1j}(0) \frac{d_{2j}}{d_{1j}} + \frac{B_j}{2\pi D} \left(\log \rho + \frac{D}{d_{1j}} \right), \quad (2.14a)$$

where B_j satisfies

$$B_j \sim -u_{1j}(0) \frac{4\pi D d_{2j}}{d_{1j} \log(\tau/[\kappa_{0j}e^{-\gamma_e}])} + \mathcal{O}\left([\log(\tau/(\kappa_{0j}e^{-\gamma_e}))]^{-2}\right), \quad \text{for } \tau \gg 1. \quad (2.14b)$$

A similar analysis can be done for the case where $u_{1j}(0) = 0$. By evaluating (1.5c) at $t = 0$, and using $U(\mathbf{x}, 0) = 0$ and $u_{1j}(0) = 0$, we conclude for $\tau = \mathcal{O}(1)$ that

$$u_{1j} \sim \varepsilon^2 \tau u'_{1j}(0), \quad \text{where } u'_{1j}(0) = \mathbf{e}_1^T \mathbf{F}_j(\mathbf{u}_j(0)). \quad (2.15)$$

As a result, we replace $u_{1j}(0)$ in the boundary condition on $\rho = 1$ in (2.7) with $\varepsilon^2 \tau u'_{1j}(0)$ to derive, in place of (2.8), that

$$\hat{V}(\rho, s) = d_{2j} \varepsilon^2 u'_{1j}(0) \left(\frac{K_0(\rho\sqrt{s/D})}{s^2 [d_{1j} K_0(\sqrt{s/D}) + \sqrt{sD} K_1(\sqrt{s/D})]} \right). \quad (2.16)$$

To determine the large τ behavior for $\rho > 1$ fixed, we let $s \rightarrow 0$ in (2.16) to conclude that

$$V(\rho, \tau) \sim \varepsilon^2 \tau u'_{1j}(0) \frac{d_{2j}}{d_{1j}} + 2\varepsilon^2 u'_{1j}(0) \frac{d_{2j}}{d_{1j}} \left(\log \rho + \frac{D}{d_{1j}} \right) \mathcal{L}^{-1} \left[\frac{1}{s^2 \log(\kappa_{0j}s)} \right], \quad (2.17)$$

where κ_{0j} is given in (2.9b). By convolving $\mathcal{L}^{-1}[(s \log(\kappa_{0j}s)^{-1}] = -N(\tau/\kappa_{0j})$ and $\mathcal{L}^{-1}[s^{-1}] = 1$, we obtain from (2.17) for $\tau \gg 1$ and $\rho = \mathcal{O}(1)$ that

$$V(\rho, \tau) \sim \varepsilon^2 \tau u'_{1j}(0) \frac{d_{2j}}{d_{1j}} + \frac{B_j}{2\pi D} \left(\log \rho + \frac{D}{d_{1j}} \right), \quad (2.18a)$$

where, in terms of Ramanujan's integral $N(x)$ in (2.11) and with $u'_{1j}(0) = \mathbf{e}_1^T \mathbf{F}_j(\mathbf{u}_j(0))$, B_j now satisfies

$$B_j \sim -\varepsilon^2 u'_{1j}(0) \frac{4\pi D d_{2j}}{d_{1j}} \int_0^\tau N(\xi/\kappa_{0j}) d\xi, \quad \text{for } \tau \gg 1. \quad (2.18b)$$

Finally, to estimate B_j for the range $\mathcal{O}(1) \ll \tau \ll \mathcal{O}(\varepsilon^{-2})$, we observe that since $\int_0^\infty N(\xi/\kappa_{0j}) d\xi$ is not integrable, the dominant contribution to the integral in (2.18b) arises from the upper endpoint $\xi = \tau \gg 1$ where we can use the asymptotics (2.13). Upon integrating by parts, we calculate that

$$\int_0^\tau \frac{1}{\log(\xi/(\kappa_{0j}e^{-\gamma_e}))} d\xi = -\kappa_{0j} E_1[-\log(\tau/(\kappa_{0j}e^{-\gamma_e}))] \sim \frac{\tau}{\log(\tau/(\kappa_{0j}e^{-\gamma_e}))}, \quad \text{as } \tau \rightarrow \infty, \quad (2.19)$$

where we used $E_1(z) \sim e^{-z}/z$ for $z \rightarrow +\infty$. In this way, we obtain from (2.13), (2.18b) and (2.19) that

$$B_j \sim -\varepsilon^2 \int_0^\tau \frac{u'_{1j}(0)\gamma_j}{\log(\xi/(\kappa_{0j}e^{-\gamma_e}))} d\xi = -\varepsilon^2 \frac{u'_{1j}(0)\gamma_j\tau}{\log(\tau/(\kappa_{0j}e^{-\gamma_e}))}, \quad \mathcal{O}(1) \ll \tau \ll \mathcal{O}(\varepsilon^{-2}). \quad (2.20)$$

The explicit far-field behavior of the transient solution given in (2.14b) and (2.20), valid for $\mathcal{O}(1) \ll \tau \ll \mathcal{O}(\varepsilon^{-2})$ and $\rho = \mathcal{O}(1)$, is essential for providing the initial behavior for the integro-differential system, derived below in §3, that is valid on long time scales.

3 Derivation of ODE system for intracellular kinetics

We now derive a reduced ODE system with memory for the intracellular kinetics valid that is valid for $t \gg \mathcal{O}(\varepsilon^2)$.

For $t = \mathcal{O}(1)$, in the j^{th} inner region we let $\mathbf{y} = \varepsilon^{-1}(\mathbf{x} - \mathbf{x}_j)$ with $\rho = |\mathbf{y}|$, to obtain from (1.5a) and (1.5b) that $V(\mathbf{y}, t) = U(\mathbf{x}_j + \varepsilon\mathbf{y}, t)$ satisfies the leading-order quasi-steady problem

$$\Delta_{\mathbf{y}} V = 0, \quad \text{for } \rho > 1; \quad D\partial_\rho V = d_{1j}V - d_{2j}u_{1j}, \quad \text{on } \rho = 1. \quad (3.21)$$

In terms of some $B_j(t)$ to be found, the radially symmetric solution to (3.21) is

$$V(y, t) = \frac{B_j(t)}{2\pi D} \log |\mathbf{y}| + \frac{B_j(t)}{2\pi d_{1j}} + \frac{d_{2j}}{d_{1j}} u_{1j}(t). \quad (3.22)$$

By calculating the flux as $\varepsilon^{-1} \int_{\Omega_j} (d_{1j}U - d_{2j}u_{1j}) dS_{\mathbf{x}} = B_j(t)$, we obtain from (1.5c) that

$$\frac{d\mathbf{u}_j}{dt} = \mathbf{F}_j(\mathbf{u}_j) + B_j(t)\mathbf{e}_1, \quad j \in \{1, \dots, N\}. \quad (3.23)$$

Next, by asymptotically matching (3.22) to the outer solution U , we conclude that U must satisfy

$$\begin{aligned} \partial_t U &= D\Delta U - \sigma U, \quad \mathbf{x} \in \mathbb{R}^2 \setminus \{\mathbf{x}_1, \dots, \mathbf{x}_N\}; \quad U(\mathbf{x}, 0) = 0, \\ U &\sim \frac{B_j}{2\pi D} \log |\mathbf{x} - \mathbf{x}_j| + \frac{B_j}{2\pi D\nu} + \frac{B_j}{2\pi d_{1j}} + \frac{d_{2j}}{d_{1j}} u_{1j}, \quad \text{as } \mathbf{x} \rightarrow \mathbf{x}_j, \quad j \in \{1, \dots, N\}, \end{aligned} \quad (3.24)$$

with $U(\mathbf{x}, t) \rightarrow 0$ as $|\mathbf{x}| \rightarrow \infty$ for each $t > 0$. Here $\nu \equiv -1/\log \varepsilon$, $B_j = B_j(t)$, and $u_{1j} = u_{1j}(t)$.

Remark 1. The “outer” problem (3.23) coupled to the bulk diffusion field via (3.24) will self-consistently lead to an integro-differential ODE system for $B_j(t)$ and $\mathbf{u}_j(t)$ for $j \in \{1, \dots, N\}$. For the cell-bulk model, (3.23) together with (3.24) replaces the phenomenological diffusive coupling model of [37] as given in (1.2).

To solve (3.24) we first consider an auxiliary problem for $v_k(\mathbf{x}, t)$ given by

$$\begin{aligned} \partial_t v_k &= D\Delta v_k - \sigma v_k - B_k(t)\delta(\mathbf{x} - \mathbf{x}_k); \quad v_k \rightarrow 0 \quad \text{as } |\mathbf{x}| \rightarrow \infty; \quad v_k(\mathbf{x}, 0) = 0, \\ v_k(\mathbf{x}, t) &\sim \frac{B_k(t)}{2\pi D} \log|\mathbf{x} - \mathbf{x}_k| + R_k(t) + o(1), \quad \text{as } \mathbf{x} \rightarrow \mathbf{x}_k, \end{aligned} \quad (3.25)$$

where $R_k(t)$ is to be determined in terms of $B_k(t)$. As shown in our analysis of the transient solution in §2, we must impose that $B_k(t) \rightarrow 0$ as $t \rightarrow 0^+$.

By taking the Laplace transform of (3.25) we obtain that $\hat{v}_k(\mathbf{x}, s) = \mathcal{L}[v_k(\mathbf{x}, t)]$ satisfies

$$\begin{aligned} \Delta \hat{v}_k - \frac{(\sigma + s)}{D} \hat{v}_k &= \frac{\hat{B}_k(s)}{D} \delta(\mathbf{x} - \mathbf{x}_k); \quad \hat{v}_k \rightarrow 0 \quad \text{as } |\mathbf{x}| \rightarrow \infty, \\ \hat{v}_k &\sim \frac{\hat{B}_k(s)}{2\pi D} \log|\mathbf{x} - \mathbf{x}_k| + \hat{R}_k(s), \quad \text{as } \mathbf{x} \rightarrow \mathbf{x}_k, \end{aligned} \quad (3.26)$$

where $\hat{B}_k(s) = \mathcal{L}[B_k(t)]$ and $\hat{R}_k(s) = \mathcal{L}[R_k(t)]$. By decomposing $\hat{v}_k = -\hat{B}_k \hat{G}_k$, we find that \hat{G}_k satisfies

$$\Delta \hat{G}_k - \frac{(\sigma + s)}{D} \hat{G}_k = -\frac{1}{D} \delta(\mathbf{x} - \mathbf{x}_k); \quad \hat{G}_k \rightarrow 0 \quad \text{as } |\mathbf{x}| \rightarrow \infty. \quad (3.27)$$

In terms of the modified Bessel function $K_0(z)$ of the second kind of order zero, the solution to (3.27) is

$$\hat{G}_k(\mathbf{x}, s) = \frac{1}{2\pi D} K_0 \left(\sqrt{\frac{s + \sigma}{D}} |\mathbf{x} - \mathbf{x}_k| \right). \quad (3.28)$$

In (3.28) we specify the principal branch of the square root, so that \hat{G}_k is analytic in the complex s plane except along the branch cut where $\text{Re}(s) \leq -\sigma$ and $\text{Im}(s) = 0$.

Upon using $K_0(z) \sim -\log z - \gamma_e + \log 2$ as $z \rightarrow 0$, where γ_e is Euler’s constant, we can calculate $\hat{v}_k(\mathbf{x}, s)$ as $\mathbf{x} \rightarrow \mathbf{x}_k$ and enforce that this limiting behavior agrees with that required in (3.26). By specifying the principal branch of $\log(s + \sigma)$, this determines that

$$\hat{R}_k(s) = \frac{1}{4\pi D} \hat{B}_k(s) \log(s + \sigma) + \frac{\hat{B}_k(s)}{2\pi D} \left(\gamma_e - \log(2\sqrt{D}) \right). \quad (3.29)$$

Then, by using the well-known inverse Laplace transform (cf. [1])

$$\mathcal{L}^{-1} [K_0(a\sqrt{s})] = \frac{1}{2t} e^{-a^2/(4t)} \quad \text{for } a > 0,$$

together with the shift property of the Laplace transform, we conclude from (3.27) that

$$G_k(\mathbf{x}, t) = \mathcal{L}^{-1} [\hat{G}_k(\mathbf{x}, s)] = \frac{1}{4\pi D t} e^{-\sigma t} e^{-|\mathbf{x} - \mathbf{x}_k|^2/(4Dt)}, \quad (3.30)$$

which is simply the fundamental solution of the heat equation with bulk degradation. By using the convolution property we calculate $v_k(\mathbf{x}, t) = -\mathcal{L}^{-1} [\hat{B}_k \hat{G}_k]$ as

$$v_k(\mathbf{x}, t) = - \int_0^t B_k(\tau) G_k(\mathbf{x}, t - \tau) d\tau = - \int_0^t \frac{B_k(\tau) e^{-\sigma(t-\tau)}}{4\pi D(t-\tau)} e^{-|\mathbf{x} - \mathbf{x}_k|^2/(4D(t-\tau))} d\tau. \quad (3.31)$$

Next, we invert (3.29) under the assumption that $B_k(0) = 0$ to derive that

$$R_k(t) = \frac{1}{4\pi D} \mathcal{L}^{-1} \left[s \hat{B}_k(s) \left(\frac{\log(s + \sigma)}{s} \right) \right] + \frac{B_k(t)}{2\pi D} \left(\gamma_e - \log(2\sqrt{D}) \right). \quad (3.32)$$

From the inverse transforms $B'_k(t) = \mathcal{L}^{-1} [s\hat{B}_k(s)]$ and $\mathcal{L} [s^{-1} \log(s + \sigma)] = E_1(\sigma t) + \log \sigma$ for $\sigma > 0$ (cf. [1]), we obtain from the convolution property and $B_k(0) = 0$ that

$$\mathcal{L}^{-1} [\hat{B}_k \log(s + \sigma)] = \int_0^t B'_k(\tau) E_1(\sigma(t - \tau)) d\tau + B_k(t) \log \sigma. \quad (3.33)$$

In this way, in terms of the exponential integral $E_1(z)$, we conclude from (3.32) that

$$R_k(t) = \frac{B_k(t)}{2\pi D} \left[\gamma_e - \log \left(2\sqrt{\frac{D}{\sigma}} \right) \right] + \frac{1}{4\pi D} \int_0^t B'_k(\tau) E_1(\sigma(t - \tau)) d\tau. \quad (3.34)$$

We represent the solution to (3.24) as the superposition $U(\mathbf{x}, t) = \sum_{k=1}^N v_k(\mathbf{x}, t)$. By letting $\mathbf{x} \rightarrow \mathbf{x}_j$, and enforcing that the limiting behavior of $U(\mathbf{x}, t)$ agrees with that required in (3.24), we conclude that

$$R_j(t) + \sum_{\substack{k=1 \\ k \neq j}}^N v_k(\mathbf{x}_j, t) = \frac{B_j(t)}{2\pi D} \left(\frac{1}{\nu} + \frac{D}{d_{1j}} \right) + \frac{d_{2j}}{d_{1j}} u_{1j}(t), \quad j \in \{1, \dots, N\}. \quad (3.35)$$

Upon using (3.34) for $R_j(t)$, we observe that (3.35) determines $B_j(t)$ in terms of $u_{1j}(t)$.

Finally, upon combining (3.35) with the intracellular dynamics (3.23) we obtain an integro-differential system for the intracellular species $\mathbf{u}_j(t)$ that is coupled to the time-history of the source strengths $B_j(t)$. We summarize our result in the following formal proposition.

Proposition 1. *For $\varepsilon \rightarrow 0$, and with the initial condition $U(\mathbf{x}, 0) = 0$, the solution $U(\mathbf{x}, t)$ and $\mathbf{u}_j(t)$, for $j \in \{1, \dots, N\}$, to the cell-bulk model (1.5) is approximated for $t \gg \mathcal{O}(\varepsilon^2)$ by*

$$\frac{d\mathbf{u}_j}{dt} = \mathbf{F}_j(\mathbf{u}_j) + \mathbf{e}_1 B_j(t), \quad (3.36a)$$

$$\int_0^t B'_j(\tau) E_1(\sigma(t - \tau)) d\tau = \eta_j B_j(t) + \gamma_j u_{1j}(t) + \sum_{\substack{k=1 \\ k \neq j}}^N \int_0^t \frac{B_k(\tau) e^{-\sigma(t-\tau)}}{t - \tau} e^{-|\mathbf{x}_j - \mathbf{x}_k|^2 / (4D(t-\tau))} d\tau, \quad (3.36b)$$

for $j \in \{1, \dots, N\}$. In this integro-differential system η_j and γ_j are defined by

$$\eta_j \equiv 2 \left(\frac{1}{\nu} + \frac{D}{d_{1j}} + \log \left(2\sqrt{\frac{D}{\sigma}} \right) - \gamma_e \right) = -\log(\varepsilon^2 \kappa_{0j} \sigma), \quad \gamma_j \equiv \frac{4\pi D d_{2j}}{d_{1j}}, \quad (3.36c)$$

where κ_{0j} is defined in (2.9b). In terms of $B_j(t)$, the approximate solution in the bulk region is

$$U(\mathbf{x}, t) \sim -\frac{1}{4\pi D} \sum_{j=1}^N \int_0^t \frac{B_j(\tau) e^{-\sigma(t-\tau)}}{t - \tau} e^{-|\mathbf{x} - \mathbf{x}_j|^2 / (4D(t-\tau))} d\tau, \quad (3.37)$$

while in the vicinity of the j^{th} cell we have for $\rho = \varepsilon^{-1} |\mathbf{x} - \mathbf{x}_j| = \mathcal{O}(1)$ that

$$U \sim \frac{B_j(t)}{2\pi D} \log \rho + \frac{B_j(t)}{2\pi d_{1j}} + \frac{d_{2j}}{d_{1j}} u_{1j}(t). \quad (3.38)$$

3.1 Matching to the Transient Solution

We now study the limiting behavior as $t \rightarrow 0^+$, but with $t \gg \mathcal{O}(\varepsilon^2)$, for $B_j(t)$ in (3.36), which satisfies $B_j \rightarrow 0$ as $t \rightarrow 0$. Our small time analysis is based on taking the Laplace transform of (3.36b) and letting $s \rightarrow \infty$. More specifically, we will derive that

$$B_j(t) \sim \begin{cases} -u'_{1j}(0) \gamma_j t / \log(t / (\kappa_j e^{-\gamma_e})), & \text{as } t \rightarrow 0^+ \text{ if } u_{1j}(0) = 0, \\ -u_{1j}(0) \gamma_j / \log(t / (\kappa_j e^{-\gamma_e})), & \text{as } t \rightarrow 0^+ \text{ if } u_{1j}(0) \neq 0, \end{cases} \quad (3.39)$$

where $\kappa_j = \varepsilon^2 \kappa_{0j}$ with κ_{0j} defined in (2.9b). These limiting results agree with those derived in §2 from the far-field behavior of the transient solution. Moreover, we have

$$B'_j(t) \sim \begin{cases} -\frac{u'_{1j}(0)\gamma_j}{\log(t/(\kappa_j e^{-\gamma_e}))} \left(1 - \frac{1}{\log(t/(\kappa_j e^{-\gamma_e}))}\right), & \text{as } t \rightarrow 0^+ \text{ if } u_{1j}(0) = 0, \\ u_{1j}(0)\gamma_j / \left(t [\log(t/(\kappa_j e^{-\gamma_e}))]^2\right), & \text{as } t \rightarrow 0^+ \text{ if } u_{1j}(0) \neq 0. \end{cases} \quad (3.40)$$

Therefore, $B'_j(t) \rightarrow 0$ as $t \rightarrow 0^+$ if $u_{1j}(0) = 0$, while $|B'_j(t)| \rightarrow \infty$ as $t \rightarrow 0^+$ if $u_{1j}(0) \neq 0$.

To derive (3.39), we will first assume that $u_{1j}(0) = 0$. Setting $B_j(0) = 0$, we obtain from (3.36a) that $u_{1j}(t) \sim t u'_{1j}(0)$ as $t \rightarrow 0^+$, where $u'_{1j}(0) = \mathbf{e}_1^T \mathbf{F}(\mathbf{u}_j(0))$. By taking the Laplace transform of (3.36b) and by using $\mathcal{L}[B'_j(t)] = s \hat{B}_j(s)$ and $\mathcal{L}[E_1(\sigma t)] = \log(1 + s/\sigma)/s$ we readily calculate that

$$\hat{B}_j [\log(1 + s/\sigma) - \eta_j] - 2 \sum_{\substack{k=1 \\ k \neq j}}^N \hat{B}_k K_0 \left(\sqrt{\frac{s + \sigma}{D}} |\mathbf{x}_j - \mathbf{x}_k| \right) = \hat{u}_{j1} \gamma_j. \quad (3.41)$$

By using the exponential decay of K_0 and $\hat{u}_{j1} \sim u'_{1j}(0)/s^2$ for $s \rightarrow \infty$, (3.41) becomes

$$\hat{B}_j \left[\log \left(\frac{s e^{-\eta_j}}{\sigma} \right) + \mathcal{O}(s^{-1}) \right] \sim \frac{\gamma_j}{s^2} u'_{1j}(0), \quad \text{as } s \rightarrow \infty. \quad (3.42)$$

By neglecting the $\mathcal{O}(s^{-1})$ term, we use (3.36c) for η_j to calculate from (3.42) that

$$\hat{B}_j \sim \frac{u'_{1j}(0)\gamma_j}{s^2 \log(\kappa_j s)}, \quad \text{as } s \rightarrow \infty, \quad \text{where } \kappa_j \equiv \frac{e^{-\eta_j}}{\sigma} = \varepsilon^2 \kappa_{0j}. \quad (3.43)$$

As a result, for $t \rightarrow 0^+$, but with $t \gg \mathcal{O}(\varepsilon^2)$, we use the convolution property and $\kappa_j = \varepsilon^2 \kappa_{0j}$ to obtain

$$B_j(t) \sim -u'_{1j}(0)\gamma_j \int_0^t N \left(\frac{\xi}{\varepsilon^2 \kappa_{0j}} \right) d\xi, \quad \text{for } \mathcal{O}(\varepsilon^2) \ll t \ll \mathcal{O}(1), \quad (3.44)$$

where $N(x)$ is Ramanujan's integral (2.11), κ_{0j} is defined in (2.9b) and $u'_{1j}(0) = \mathbf{e}_1^T \mathbf{F}_j(\mathbf{u}_j(0))$. This limiting result matches identically with the result derived in (2.18b) of §2. Moreover, by setting $t = \varepsilon^2 \tau$ in (2.20) we obtain the first result in (3.39).

A very similar short-time analysis can be done when $u_{1j}(0) \neq 0$. In place of (3.43), we obtain that

$$\hat{B}_j \sim \frac{u_{1j}(0)\gamma_j}{s \log(\kappa_j s)}, \quad \text{as } s \rightarrow \infty. \quad (3.45)$$

By inverting (3.45), and recalling that $\gamma_j = 4\pi D d_{2j}/d_{1j}$, we obtain the second result in (3.39). This result matches identically with the far-field behavior (2.14b) as obtained from our transient analysis in §2.

4 Steady-state and linear stability analysis

In this section, we first classify the long-time dynamics of (3.36) for solutions that tend to limiting values as $t \rightarrow \infty$. We show that this limiting dynamics coincides with the steady-state solution, which is constructed using strong localized perturbation theory from the steady-state of the cell-bulk PDE system (1.5). We also formulate the linear stability problem for steady-state solutions. We begin with the following lemma:

Lemma 4.1. *Suppose that $B_j(0) = 0$, $B_j(t)$ is bounded for $t > 0$ and that $B_j(t) \rightarrow B_{j\infty}$ as $t \rightarrow \infty$ for $j \in \{1, \dots, N\}$, where $B_{j\infty}$ are constants for $j \in \{1, \dots, N\}$. Then,*

$$\lim_{t \rightarrow \infty} C_{jk}(t) = 2B_{j\infty}K_0 \left(\sqrt{\frac{\sigma}{D}} |\mathbf{x}_j - \mathbf{x}_k| \right), \quad \lim_{t \rightarrow \infty} D_j(t) = 0, \quad (4.46a)$$

$$\text{where } C_{jk}(t) \equiv \int_0^t \frac{B_j(\tau) e^{-\sigma(t-\tau)}}{t-\tau} e^{-|\mathbf{x}_j - \mathbf{x}_k|^2/(4D(t-\tau))} d\tau, \quad (4.46b)$$

$$\text{and } D_j(t) \equiv \int_0^t B_j'(\tau) E_1(\sigma(t-\tau)) d\tau. \quad (4.46c)$$

Proof. To establish the first limit in (4.46a), we take the Laplace transform of (4.46b) to obtain

$$\hat{C}_{jk}(s) = \mathcal{L} \left[\frac{e^{-\sigma t}}{t} e^{-|\mathbf{x}_j - \mathbf{x}_k|^2/(4Dt)} \right] \hat{B}_j(s) = 2K_0 \left(\sqrt{\frac{s+\sigma}{D}} |\mathbf{x}_j - \mathbf{x}_k| \right) \hat{B}_j(s). \quad (4.47)$$

To determine the long-time behavior of $C_{jk}(t)$, we will use the Tauberian theorem. Since $B_j(t)$ is bounded for $t > 0$ and satisfies $B_j(t) \rightarrow B_{j\infty}$ as $t \rightarrow \infty$, it follows that $\hat{B}_j(s)$ is analytic for $\text{Re}(s) > 0$ and that the singularity with the largest real part is a simple pole at $s = 0$ for which $\hat{B}_j(s) \sim B_{j\infty}/s$ as $s \rightarrow 0$. As a result, the singularity of $\hat{C}_{jk}(s)$ with the largest real part is a simple pole at $s = 0$ and we have

$$\lim_{t \rightarrow \infty} C_{jk}(t) = \lim_{s \rightarrow 0} s \hat{C}_{jk}(s) = 2K_0 \left(\sqrt{\frac{\sigma}{D}} |\mathbf{x}_j - \mathbf{x}_k| \right) \lim_{s \rightarrow 0} s \hat{B}_j(s), \quad (4.48)$$

where $\lim_{s \rightarrow 0} s \hat{B}_j(s) = B_{j\infty}$. This proves the first result in (4.46a).

The second result in (4.46a) is established in a similar way. Upon taking the Laplace transform of $D_j(t)$ in (4.46c), we use $B_j(0) = 0$ to obtain that

$$\hat{D}_j(s) = \mathcal{L} [B_j'(t)] \mathcal{L} [E_1(\sigma t)] = s \hat{B}_j(s) \frac{\log(1+s/\sigma)}{s} = \hat{B}_j(s) \log(1+s/\sigma), \quad (4.49)$$

where the branch cut for $\log(1+s/\sigma)$ occurs for $\text{Re}(s) \leq -\sigma < 0$ and $\text{Im}(s) = 0$. To establish that $D_j(t) \rightarrow 0$ as $t \rightarrow \infty$ it suffices to show that $\hat{D}_j(s)$ is analytic in $\text{Re}(s) \geq 0$. This follows since from (4.49) we observe that, although $\hat{B}_j \sim B_{j\infty}/s$ as $s \rightarrow 0$, the point $s = 0$ is a removable singularity for $\hat{D}_j(s)$. \square

With this lemma, we can readily characterize those solutions to (3.36) that tend to limiting values as $t \rightarrow \infty$. We summarize this result as follows:

Proposition 2. *Suppose that $B_j(0) = 0$ and that $B_j(t)$ and $\mathbf{u}_j(t)$ are bounded for $t \geq 0$ with limiting values $B_j(t) \rightarrow B_{j\infty}$ and $\mathbf{u}_j \rightarrow \mathbf{u}_{j\infty}$ as $t \rightarrow \infty$ for each $j \in \{1, \dots, N\}$. Then, with η_j and γ_j as defined in (3.36c), $B_{j\infty}$ and $\mathbf{u}_{j\infty}$ satisfy the $N(m+1)$ dimensional nonlinear algebraic system (NAS)*

$$\mathbf{F}_j(\mathbf{u}_{j\infty}) + \mathbf{e}_1 B_{j\infty} = 0, \quad j \in \{1, \dots, N\}, \quad (4.50a)$$

$$\eta_j B_{j\infty} + 2 \sum_{\substack{k=1 \\ k \neq j}}^N B_{k\infty} K_0 \left(\sqrt{\frac{\sigma}{D}} |\mathbf{x}_j - \mathbf{x}_k| \right) = -\gamma_j \mathbf{e}_1^T \mathbf{u}_{j\infty}, \quad j \in \{1, \dots, N\}. \quad (4.50b)$$

We now show that the limiting NAS (4.50) is precisely the same system as can be derived from a strong localized perturbation analysis for steady-state solutions of (1.5) by following the methodology of [33]. In the limit $\varepsilon \rightarrow 0$, the steady-state problem for the outer bulk solution $U_s(\mathbf{x})$ is

$$D\Delta U_s - \sigma U_s = 0, \quad \mathbf{x} \in \mathbb{R}^2 \setminus \{\mathbf{x}_1, \dots, \mathbf{x}_N\},$$

$$U_s \sim \frac{B_{js}}{2\pi D} \log |\mathbf{x} - \mathbf{x}_j| + \frac{B_{js}}{2\pi D\nu} + \frac{B_{js}}{2\pi d_{1j}} + \frac{d_{2j}}{d_{1j}} u_{1js}, \quad \text{as } \mathbf{x} \rightarrow \mathbf{x}_j, \quad j \in \{1, \dots, N\}, \quad (4.51)$$

where $\nu \equiv -1/\log \varepsilon$. This system is coupled to the steady-state of the intracellular kinetics, given by

$$\mathbf{F}_j(\mathbf{u}_{js}) + \mathbf{e}_1 B_{js} = 0, \quad j \in \{1, \dots, N\}. \quad (4.52)$$

In terms of the modified Bessel function $K_0(z)$, the solution to (4.51) is

$$U_s(\mathbf{x}) = - \sum_{k=1}^N \frac{B_{ks}}{2\pi D} K_0 \left(\sqrt{\frac{\sigma}{D}} |\mathbf{x} - \mathbf{x}_k| \right). \quad (4.53)$$

To determine B_{js} , for $j \in \{1, \dots, N\}$, we enforce that the local behavior of $U_s(\mathbf{x})$ as $\mathbf{x} \rightarrow \mathbf{x}_j$ agrees with that required in (4.51). Upon using $K_0(z) \sim -\log(z/2) - \gamma_e + o(1)$ as $z \rightarrow 0$, this condition yields

$$\eta_j B_{js} + \gamma_j u_{1js} + 2 \sum_{\substack{k=1 \\ k \neq j}}^N B_{ks} K_0 \left(\sqrt{\frac{\sigma}{D}} |\mathbf{x}_j - \mathbf{x}_k| \right) = 0, \quad j \in \{1, \dots, N\}. \quad (4.54)$$

The coupled system (4.54) and (4.52) characterizing the steady-state solution is identical to that in (4.50).

4.1 Linear Stability Analysis

We now derive a globally coupled eigenvalue problem (GCEP) for the linearization of the cell-bulk model (1.5) around the steady-state solution. To derive the GCEP we first perturb around the steady-state solution by introducing the eigen-perturbation

$$U = U_s(\mathbf{x}) + e^{\lambda t} \Phi(\mathbf{x}), \quad \mathbf{u}_j = \mathbf{u}_{js} + e^{\lambda t} \zeta_j, \quad j \in \{1, \dots, N\}, \quad (4.55)$$

into (1.5). Upon linearizing, we obtain the eigenvalue problem

$$\Delta \Phi - \frac{(\lambda + \sigma)}{D} \Phi = 0, \quad \mathbf{x} \in \mathbb{R}^2 \setminus \cup_{j=1}^N \Omega_{\varepsilon_j}, \quad (4.56a)$$

$$\varepsilon D \partial_n \Phi = d_{1j} \Phi - d_{2j} \zeta_{j1}, \quad \mathbf{x} \in \partial \Omega_{\varepsilon_j}, \quad j \in \{1, \dots, N\}, \quad (4.56b)$$

which is coupled to the linearized intracellular dynamics within the j^{th} cell by

$$\lambda \zeta_j = J_j \zeta_j + \frac{\mathbf{e}_1}{\varepsilon} \int_{\partial \Omega_{\varepsilon_j}} (d_{1j} \Phi - d_{2j} \zeta_{j1}) dS_{\mathbf{x}}, \quad j \in \{1, \dots, N\}. \quad (4.56c)$$

Here $J_j \equiv D_{\mathbf{u}_j} \mathbf{F}_j$ is the Jacobian of the intracellular kinetics evaluated at $\mathbf{u}_j = \mathbf{u}_{js}$.

For $\varepsilon \rightarrow 0$, we now analyze (4.56) using strong localized perturbation theory. In the inner region near the j^{th} cell, we have to leading-order from (4.56a) and (4.56b) that

$$\Delta_{\mathbf{y}} \Phi = 0, \quad \text{for } \rho > 1; \quad D \Phi_\rho = d_{1j} \Phi - d_{2j} \zeta_{j1}, \quad \text{on } \rho = 1. \quad (4.57)$$

In terms of some c_j to be found, (4.57) has the radially symmetric solution

$$\Phi = \frac{c_j}{2\pi D} \log |\mathbf{y}| + \frac{c_j}{2\pi d_{1j}} + \frac{d_{2j}}{d_{1j}} \zeta_{j1}. \quad (4.58)$$

By calculating the surface integral $\varepsilon^{-1} \int_{\Omega_j} (d_{1j} \Phi - d_{2j} \zeta_{j1}) dS_{\mathbf{x}} = c_j$, we obtain that (4.56c) becomes

$$(\lambda I - J_j) \zeta_j = \mathbf{e}_1 c_j, \quad j \in \{1, \dots, N\}, \quad (4.59)$$

where I is the $m \times m$ identity matrix. Upon assuming that $\lambda I - J_j$ is invertible, we calculate ζ_{j1} as

$$\zeta_{j1} = K_j c_j \quad \text{where} \quad K_j \equiv \mathbf{e}_1^T (\lambda I - J_j)^{-1} \mathbf{e}_1. \quad (4.60)$$

By writing (4.58) in terms of the outer variable, the asymptotic matching condition shows that in the outer region Φ satisfies

$$\Delta\Phi - \frac{(\lambda + \sigma)}{D}\Phi = 0, \quad \mathbf{x} \in \mathbb{R}^2 \setminus \cup_{j=1}^N \Omega_{\varepsilon_j}, \quad (4.61a)$$

$$\Phi \sim \frac{c_j}{2\pi D} \log |\mathbf{x} - \mathbf{x}_j| + \frac{c_j}{2\pi D\nu} + \frac{c_j}{2\pi d_{1j}} + \frac{d_{2j}}{d_{1j}} \zeta_{j1}, \quad \text{as } \mathbf{x} \rightarrow \mathbf{x}_j, \quad (4.61b)$$

for $j \in \{1, \dots, N\}$, where $\nu \equiv -1/\log \varepsilon$. The solution to (4.61) is

$$\Phi(\mathbf{x}) = - \sum_{k=1}^N \frac{c_k}{2\pi D} K_0 \left(\sqrt{\frac{\sigma + \lambda}{D}} |\mathbf{x} - \mathbf{x}_k| \right). \quad (4.62)$$

Upon enforcing that the limiting behavior of $\Phi(\mathbf{x})$ as $\mathbf{x} \rightarrow \mathbf{x}_j$ agree with that required in (4.61b), and where ζ_{j1} is given in terms of c_j by (4.60), we conclude for $j \in \{1, \dots, N\}$ that

$$2 \left(\frac{1}{\nu} + \frac{D}{d_{1j}} - \gamma_e + \log \left(2\sqrt{\frac{D}{\sigma + \lambda}} \right) \right) c_j + \frac{4\pi D d_{2j}}{d_{1j}} \zeta_{j1} + 2 \sum_{\substack{k=1 \\ k \neq j}}^N c_k K_0 \left(\sqrt{\frac{\sigma + \lambda}{D}} |\mathbf{x}_j - \mathbf{x}_k| \right) = 0. \quad (4.63)$$

Finally, upon writing (4.63) and (4.60) in matrix form, we obtain that the discrete eigenvalues λ of the linearization around a steady-state solution of (1.5) are obtained from a nonlinear matrix eigenvalue problem, which we refer to as the GCEP. Our result is summarized as follows:

Proposition 3. *For $\varepsilon \rightarrow 0$, the discrete eigenvalues λ associated with the linearization around a steady-state solution to (1.5), for which $\det(\lambda I - J_j) \neq 0$ for any $j \in \{1, \dots, N\}$, are the set of values*

$$\Lambda(\mathcal{M}) \equiv \{\lambda \mid \det \mathcal{M}(\lambda) = 0\}, \quad (4.64a)$$

where the $N \times N$ dimensional matrix $\mathcal{M}(\lambda)$ is defined by

$$\mathcal{M}(\lambda) \equiv I + 2\pi\nu \mathcal{G}_\lambda + \nu D P_1 + 2\pi\nu D P_2 \mathcal{K}(\lambda), \quad (4.64b)$$

with $\nu = -1/\log \varepsilon$. In (4.64b), P_1 , P_2 and \mathcal{K} are the diagonal matrices

$$P_1 \equiv \text{diag}\left(\frac{1}{d_{11}}, \dots, \frac{1}{d_{1N}}\right), \quad P_2 \equiv \text{diag}\left(\frac{d_{21}}{d_{11}}, \dots, \frac{d_{2N}}{d_{1N}}\right), \quad (4.65a)$$

$$\mathcal{K}(\lambda) \equiv \text{diag}(K_1, \dots, K_N), \quad \text{where } K_j \equiv \mathbf{e}_1^T (\lambda I - J_j)^{-1} \mathbf{e}_1. \quad (4.65b)$$

In addition, \mathcal{G}_λ is the eigenvalue-dependent Green's matrix with matrix entries

$$(\mathcal{G}_\lambda)_{ij} = (\mathcal{G}_\lambda)_{ji} \equiv \frac{1}{2\pi} K_0 \left(\sqrt{\frac{\sigma + \lambda}{D}} |\mathbf{x}_j - \mathbf{x}_i| \right), \quad i \neq j, \quad (4.66)$$

$$(\mathcal{G}_\lambda)_{jj} = R_{\lambda j} \equiv \frac{1}{2\pi} \left(\log \left(2\sqrt{\frac{D}{\sigma + \lambda}} \right) - \gamma_e \right). \quad (4.67)$$

For any specific $\lambda_0 \in \Lambda(\mathcal{M})$, we have $\det \mathcal{M}(\lambda_0) = 0$, and so $\mathcal{M}(\lambda_0)\mathbf{c} = \mathbf{0}$ has a nontrivial solution $\mathbf{c} = (c_1, \dots, c_N)^T$ that can be normalized as $|\mathbf{c}| = 1$. We conclude that the steady-state is linearly stable if, whenever $\lambda \in \Lambda(\mathcal{M})$, we have $\text{Re}(\lambda) < 0$.

We remark that the normalized nullvector $\mathbf{c} = (c_1, \dots, c_N)^T$ encodes the relative magnitude of the perturbation of the spatial gradient of the bulk signal near the cell boundaries. It also can be used to predict the relative magnitude and phase shift of intracellular oscillations for the permeable species u_{1j}

that can arise from bifurcations of the steady-state. To see this, we use the steady-state solution $U_s(\mathbf{x})$ and the perturbation (4.55) to calculate for the j^{th} cell that

$$D\partial_\rho U|_{\rho=1} \sim \frac{1}{2\pi} \left(B_{js} + \sum_{\lambda_0 \in \Lambda(\mathcal{M})} c_j e^{\lambda_0 t} \right), \quad j \in \{1, \dots, N\}, \quad (4.68a)$$

$$u_{1j} \sim u_{1js} + \sum_{\lambda_0 \in \Lambda(\mathcal{M})} K_j(\lambda_0) c_j e^{\lambda_0 t}, \quad j \in \{1, \dots, N\}, \quad (4.68b)$$

where $K_j(\lambda_0) = \mathbf{e}_1^T (\lambda_0 I - J_j)^{-1} \mathbf{e}_1$. From (4.68b) we observe that if λ_0 is complex-valued, the real and imaginary parts of the j^{th} component of the complex-valued matrix-eigenvector product $\mathcal{K}\mathbf{c}$ encode both the relative magnitude and phase shift of oscillations for the permeable species u_{1j} in the cell population. Moreover, from (4.68a), the components of the eigenvector \mathbf{c} determine the strength and phase shift of the eigen-perturbation of the signaling gradients near the cells.

5 Time-marching scheme for the integro-differential system

A direct numerical approach to solve (3.36) would require at each time step a numerical quadrature of $\mathcal{O}(N^2)$ memory-dependent convolution integrals. This naive approach would be prohibitively expensive for large N and would also require storing the full time history of each $B_j(t)$ in order to advance one time-step.

As such, we now develop a time-marching algorithm to compute solutions to (3.36). This approach is based on a highly accurate approximation of the kernels in the nonlocal terms of (3.36b) by a sum of exponentials, which leads naturally to an exponential time differencing marching scheme. Rigorous results for the *sum-of-exponentials* approximation, together with the development of time-marching methods for convolution integrals in other contexts are given in [7], [8], [42], [43], [44] and [34].

With an exponential kernel, our derivation of a time-marching scheme relies on a Duhamel-type lemma:

Lemma 5.1. *Let $f(t)$ be continuous and define the convolution $\mathcal{F}(t) \equiv \int_0^t e^{\omega(t-\tau)} f(\tau) d\tau$. Then, we have $\mathcal{F}'(t) = \omega\mathcal{F}(t) + f(t)$ with $\mathcal{F}(0) = 0$. Moreover, we have the marching scheme*

$$\mathcal{F}(t + \Delta t) = \mathcal{F}(t)e^{\omega\Delta t} + \mathcal{U}(t, \Delta t), \quad \text{with} \quad \mathcal{U}(t, \Delta t) \equiv e^{\omega\Delta t} \int_0^{\Delta t} e^{-\omega z} f(t + z) dz. \quad (5.69)$$

An exponential time differencing *ETD2* scheme (cf. [42]), ensuring that the update integral \mathcal{U} exact for linear functions $f(t)$, yields, with an error $\mathcal{O}((\Delta t)^3)$, the approximation

$$\mathcal{F}(t + \Delta t) \approx \mathcal{F}(t)e^{\omega\Delta t} + f(t) \left(\frac{e^{\omega\Delta t} - 1}{\omega} \right) + [f(t + \Delta t) - f(t)] \left(\frac{e^{\omega\Delta t} - 1 - \omega\Delta t}{\omega^2\Delta t} \right). \quad (5.70)$$

Proof. The proof of (5.69) is immediate. To derive (5.70) we substitute

$$f(t + z) = f(t) + \frac{z}{\Delta t} [f(t + \Delta t) - f(t)] + \mathcal{O}((\Delta t)^2),$$

into the update integral \mathcal{U} in (5.69) and integrate the resulting expression explicitly. \square

We now develop a time-marching scheme for (3.36b), which we write compactly as

$$D_j(t) = \eta_j B_j(t) + \gamma_j u_{1j}(t) + \sum_{\substack{k=1 \\ k \neq j}}^N C_{jk}(t), \quad (5.71)$$

where $C_{jk}(t)$ and $D_j(t)$ are defined in (4.46b) and (4.46c), respectively. We observe that both memory integrals $C_{jk}(t)$ and $D_j(t)$ are improper, as their kernels each have an integrable singularity at $t = \tau$.

5.1 Sum-of-Exponentials Approximation for $D_j(t)$ and $C_{jk}(t)$

We first develop a *sum-of-exponentials* approximation for $D_j(t)$. To do so, we use the sector analyticity of the Laplace transform of the exponential integral to deform the initial vertical Bromwich line Γ_B to the curve Γ , defined by (5.73), with endpoints at infinity in the left-half plane $\text{Re}(s) < 0$ (see Fig. 2 below). This yields that

$$E_1(\sigma t) = -\frac{1}{2\pi i} \int_{\Gamma} \mathcal{E}(s) e^{st} ds \quad \text{where} \quad \mathcal{E}(s) = \frac{\log(1 + s/\sigma)}{s}. \quad (5.72)$$

Observe that $\mathcal{E}(s)$ is analytic except along the branch cut $\text{Re}(s) \leq -\sigma$ with $\text{Im}(s) = 0$.

The *sum-of-exponentials* method following [7] (see also [34]) establishes rigorous results for the quadrature of (5.72) along a family of hyperbolic shaped curves

$$\Gamma \equiv \{s = \chi P(x), x \in \mathbb{R}\}, \quad \text{where} \quad P(x) \equiv 1 - \sin(\alpha + ix), \quad (5.73)$$

with $0 < \alpha < \pi/2$ and $\chi > 0$, where $s = \chi(1 - \sin \alpha) > 0$ at $x = 0$. The curve Γ has the limiting behavior

$$\text{Im}(s) \rightarrow \mp\infty, \quad \text{Re}(s) \rightarrow -\infty, \quad \frac{\text{Im}(s)}{\text{Re}(s)} \rightarrow \chi \cot \alpha, \quad \text{as } x \rightarrow \pm\infty.$$

To evaluate (5.72) on Γ we use $ds = \chi P'(x) dx$ and (5.73) for $P(x)$ to calculate that

$$E_1(\sigma t) = \frac{\chi}{2\pi} \int_{-\infty}^{\infty} e^{\chi P(x)t} \mathcal{E}[\chi P(x)] \cos(\alpha + ix) dx. \quad (5.74)$$

By discretizing (5.74) uniformly in x , with $x_\ell = \ell h$ for $|\ell| \leq n$, and by labeling $s_\ell = \chi P(x_\ell)$, we get

$$E_1(\sigma t) \approx E_n(t) \equiv \sum_{\ell=-n}^n e_\ell e^{s_\ell t}, \quad (5.75a)$$

where the coefficients are given explicitly by

$$e_\ell = \frac{\chi h}{2\pi} \cos(\alpha + i\ell h) \frac{\log(1 + s_\ell/\sigma)}{s_\ell}, \quad s_\ell = \chi [1 - \sin(\alpha) \cosh(\ell h)] - i\chi \cos(\alpha) \sinh(\ell h). \quad (5.75b)$$

Since $|\mathcal{E}(s)| \leq 1/(2|s|^{1/2})$ in the cut plane $\mathbb{C} \setminus (-\infty, 0)$ as $|s| \rightarrow \infty$, Lemma 1 and Corollary 1 of [34], as adapted from [44], provides the estimate for the difference $|E_1(\sigma t) - E_n(t)|$. The result is as follows.

Lemma 5.2. (cf. [34]) *Consider the time interval $0 < \delta \leq t \leq T_f$, with $T_f \geq 1000\delta$ and let ε_f with $0 < \varepsilon_f < 0.1$ be a prescribed error-tolerance. Then, for the choice of parameters h and χ defined by*

$$h = \frac{a(\theta)}{n}, \quad \chi = \frac{2\pi\beta n(1-\theta)}{T_f a(\theta)}, \quad \text{where} \quad a(\theta) \equiv \cosh^{-1} \left(\frac{2T_f}{\delta(1-\theta) \sin \alpha} \right), \quad (5.76)$$

with $0 < \alpha - \beta < \alpha + \beta < \pi/2$ and $0 < \theta < 1$, we have the uniform estimate

$$\|E_1(\sigma t) - E_n(t)\| \leq \frac{\varepsilon_f}{\sqrt{t}} \quad \text{on} \quad \delta \leq t \leq T_f, \quad (5.77)$$

when n is sufficiently large of the order

$$n = \mathcal{O}((-\log \varepsilon_f + \log \log(T_f/\delta)) \log(T_f/\delta)). \quad (5.78)$$

In (5.76), the parameters α , β and θ , satisfying the constraint in Lemma 5.2, can be optimized so as to minimize the number of terms needed to achieve a prescribed accuracy. As in [34], we chose $\alpha = 0.8$ and $\beta = 0.7$ in all the results below with θ in the range $[0.90, 0.95]$ (see below). The key conclusion is

that the number of terms in the sum grows very slowly as either the tolerance ε_f decreases or as T_f/δ increases.

In a similar way, we can develop a sum-of-exponentials approximation for $C_{jk}(t)$ defined in (4.46b). From the Laplace-transform pair

$$\mathcal{L}[G(a_{jk}, t)] = 2K_0 (2a_{jk}\sqrt{s + \sigma}), \quad \text{where} \quad G(a_{jk}, t) \equiv \frac{e^{-\sigma t}}{t} e^{-a_{jk}^2/t}, \quad a_{jk} \equiv \frac{|\mathbf{x}_j - \mathbf{x}_k|}{\sqrt{4D}}, \quad (5.79)$$

we observe that $K_0 (2a_{jk}\sqrt{s + \sigma})$ is analytic in the complex s -plane except across the branch cut $\text{Re}(s) \leq -\sigma$ with $\text{Im}(s) = 0$. Therefore, we can approximate $G(a_{jk}, t)$ by a sum of exponentials, similar to that done in (5.75), to obtain

$$G(a_{jk}, t) \approx G_n(a_{jk}, t) \equiv \sum_{\ell=-n}^n \omega_{jk\ell} e^{s_\ell t}, \quad (5.80a)$$

where the coefficients are

$$\omega_{jk\ell} = \frac{\chi h}{2\pi} \cos(\alpha + i\ell h) 2K_0 (2a_{jk}\sqrt{s_\ell + \sigma}), \quad s_\ell = \chi P(x_\ell). \quad (5.80b)$$

Owing to the same branch cut structure as for approximating $E_1(\sigma t)$, for simplicity in our approximation (5.80a) we choose the same values of the parameters $\alpha = 0.8$ and $\beta = 0.7$ used in (5.75), which provides a comparable accuracy. We emphasize that the coefficients $\omega_{jk\ell}$ will depend on j and k owing to the inter-cell distances $|\mathbf{x}_j - \mathbf{x}_k|$. For N cells, there are $N(N-1)/2$ sets $\{\omega_{jk\ell} \mid -n \leq \ell \leq n\}$ of coefficients that need to be calculated once and stored for the algorithm developed below in §5.4.

We now provide some numerical results for three *sum-of-exponentials* approximations. Under the conditions of Lemma 5.2 the difference between a function $f(x, t)$, with Laplace transform $\hat{f}(x, s)$, and its *sum-of-exponentials* approximation $f_a(x, t) = \sum_{-n}^n w_k e^{s_k t}$ with an error magnitude ε_f is

$$\|f(x, t) - f_a(x, t)\| \leq \frac{\varepsilon_f}{\sqrt{t}}, \quad \text{on} \quad t \in [\delta, T]. \quad (5.81)$$

In the tables below $f(x, t)$ is taken either as the 1-D heat-kernel $G_{1D}(x, t)$ considered in [34], the 2-D heat-kernel with bulk degradation $G_{2D}(x, t) \equiv (4\pi t)^{-1} e^{-x^2/(4t) - \sigma t} = (4\pi)^{-1} G(x, t)$, where $G(x, t)$ is given in (5.79), or the exponential integral $E_1(\sigma t)$. Recall that the discretization points are

$$w_k = \frac{\chi h}{2\pi} \cos(\alpha + ikh) \hat{f}(x, s_k), \quad \text{where} \quad s_k = \chi(1 - \sin(\alpha + ikh)).$$

In order to estimate $\sqrt{t} \|f(x, t) - f_a(x, t)\|$ depending on the number $2n + 1$ of terms in the *sum-of-exponentials* approximation we proceed as in [34]. We take a 50×1000 grid (x_j, t_k) where $x_0 = 0$, $x_j = 2^{-16+j}$ for $j \in \{1, \dots, 49\}$ (not applicable for $E_1(\sigma t)$), and $t_k = \delta e^{k\blacktriangle}$ with $\blacktriangle \equiv \log(T/\delta)/999$ for $k \in \{0, \dots, 999\}$ (equi-spaced on a logarithmic scale). We then compute $\max_{j,k} \sqrt{t} |f(x_j, t_k) - f_a(x_j, t_k)|$, which provides the error results given in the tables below on the three different intervals $I_1 \equiv [\delta, T] = [10^{-3}, 1]$, $I_2 \equiv [\delta, T] = [10^{-3}, 10^3]$ and $I_3 \equiv [\delta, T] = [10^{-5}, 10^4]$.

In Table 1 we first reproduce the numerical error table of [34] for the *sum-of-exponentials* approximation of the 1-D heat kernel $G_{1D}(x, t) \equiv (4\pi t)^{-1/2} e^{-x^2/(4t)}$.

In Table 2 and Table 3 we provide similar numerical error tables for the 2-D heat kernel with degradation $G_{2D}(x, t) = (4\pi t)^{-1} e^{-x^2/(4t) - \sigma t}$ with $\sigma = 1$ and for the exponential integral $E_1(\sigma t) = \int_{\sigma t}^{\infty} \eta^{-1} e^{-\eta} d\eta$ with $\sigma = 1$, respectively. For the 2-D heat kernel, we observe that we require a slightly higher number of terms in the *sum-of-exponentials* approximation than for the 1-D heat kernel or the exponential integral. However, this causes essentially no time constraint for our overall numerical scheme in §5.4 since the exponential sum representation has to be created only once at the beginning of the time marching stepping for a given spatial arrangement of cells. Creating these exponential sum approximations for both the 2-D heat kernel and the exponential integral takes less than $2s$ on a laptop for $n(I_2) = 77$.

ε_f	$n(I_1)$	$n(I_2)$	$n(I_3)$
10^{-3}	15 ($6.598 \cdot 10^{-4}$)	23 ($9.768 \cdot 10^{-4}$)	32 ($9.095 \cdot 10^{-4}$)
10^{-6}	31 ($7.795 \cdot 10^{-7}$)	50 ($8.709 \cdot 10^{-7}$)	68 ($9.643 \cdot 10^{-7}$)
10^{-9}	47 ($9.199 \cdot 10^{-10}$)	77 ($9.107 \cdot 10^{-10}$)	105 ($8.817 \cdot 10^{-10}$)

Table 1: The number $2n + 1$ of terms needed to approximate the 1-D heat kernel $G_{1D}(x, t) \equiv (4\pi t)^{-1/2} e^{-x^2/(4t)}$ with Laplace transform $\mathcal{L}[G_1(x, t)] = \frac{1}{2\sqrt{s}} e^{-\sqrt{s}|x|}$ to a precision ε_f corresponding to (5.81) for the three time intervals $I_1 = [10^{-3}, 1]$, $I_2 = [10^{-3}, 10^3]$ and $I_3 = [10^{-5}, 10^4]$. This table essentially reproduces Table 1 in [34] with a few additional explicit error values.

ε_f	$n(I_1)$	$n(I_2)$	$n(I_3)$
10^{-3}	31 ($8.085 \cdot 10^{-4}$)	49 ($8.663 \cdot 10^{-4}$)	91 ($8.089 \cdot 10^{-5}$)
10^{-6}	45 ($6.690 \cdot 10^{-7}$)	75 ($9.272 \cdot 10^{-7}$)	114 ($9.799 \cdot 10^{-7}$)
10^{-9}	64 ($7.028 \cdot 10^{-10}$)	110 ($8.417 \cdot 10^{-11}$)	150 ($9.343 \cdot 10^{-10}$)

Table 2: Number $2n + 1$ of terms needed to approximate the 2-D heat kernel with degradation $G_{2D}(x, t) = (4\pi t)^{-1} e^{-x^2/(4t) - \sigma t}$ with Laplace transform $\mathcal{L}[G_{2D}(x, t)] = (2\pi)^{-1} K_0(x\sqrt{s + \sigma})$ to a precision ε_f for $\sigma = 1$ corresponding to (5.81) for the three time intervals $I_1 = [10^{-3}, 1]$, $I_2 = [10^{-3}, 10^3]$ and $I_3 = [10^{-5}, 10^4]$.

ε_f	$n(I_1)$	$n(I_2)$	$n(I_3)$
10^{-3}	31 ($8.824 \cdot 10^{-5}$)	49 ($9.457 \cdot 10^{-5}$)	91 ($8.424 \cdot 10^{-5}$)
10^{-6}	45 ($8.362 \cdot 10^{-7}$)	75 ($7.902 \cdot 10^{-7}$)	114 ($9.532 \cdot 10^{-7}$)
10^{-9}	64 ($9.620 \cdot 10^{-10}$)	110 ($9.229 \cdot 10^{-10}$)	150 ($9.525 \cdot 10^{-10}$)

Table 3: Number $2n + 1$ of terms needed to approximate the exponential integral $E_1(\sigma t)$ for $\sigma = 1$ with Laplace transform $\mathcal{L}[E_1(\sigma t)] = \log(1 + s/\sigma)/s$ to a precision ε_f corresponding to (5.81) for the three time intervals $I_1 = [10^{-3}, 1]$, $I_2 = [10^{-3}, 10^3]$ and $I_3 = [10^{-5}, 10^4]$.

We remark that $\theta = 0.95$ was chosen for Table 2 while $\theta = 0.90$ was chosen for Table 3. For Table 1, $\theta = 0.9$ was chosen only for I_1 , with $\theta = 0.95$ otherwise. In our time-stepping algorithm developed below in §5.4 and implemented in §6 for Sel'kov reaction kinetics, we primarily used $\theta = 0.95$ and $n = 75$ for the *sum-of-exponentials* approximation for $E_1(\sigma t)$ and $G_{2D}(x, t)$, so that the discretization points s_ℓ were common to both approximations. Overall, this achieved an accuracy of roughly 10^{-9} for $E_1(\sigma t)$ on the time interval $[10^{-3}, 10^3]$. In §6.6 below, where we will study the phase coherence of intracellular oscillations by computing the Kuramoto order parameter over long time intervals, we will use $n = 114$.

5.2 Time-marching scheme for $D_j(t)$

We first decompose $D_j(t)$ into the sum of a local term $D_{Lj}(t)$ near the singularity of the kernel and a history term $D_{Hj}(t)$ as

$$D_j(t) = D_{Hj}(t) + D_{Lj}(t), \quad (5.82a)$$

where for some Δt , with $0 < \Delta t \ll 1$, we define

$$D_{Hj}(t) \equiv \int_0^{t-\Delta t} B'_j(\tau) E_1[\sigma(t-\tau)] d\tau, \quad (5.82b)$$

$$D_{Lj}(t) \equiv \int_{t-\Delta t}^t B'_j(\tau) E_1[\sigma(t-\tau)] d\tau = \int_0^{\Delta t} B'_j(t-z) E_1(\sigma z) dz. \quad (5.82c)$$

The approximation given in the next lemma for the local contribution $D_{Lj}(t)$ ensures that the quadrature is exact for linear functions on ranges where $B'_j(\tau)$ is continuous. However, the estimate for $D_{Lj}(\Delta t)$ is more delicate since, owing to the singular behavior for $B'_j(\tau)$ given in (3.39) when $u_{1j}(0) \neq 0$, we cannot in general assume that $B'_j(\tau)$ is approximately linear on $0 < \tau < \Delta t$.

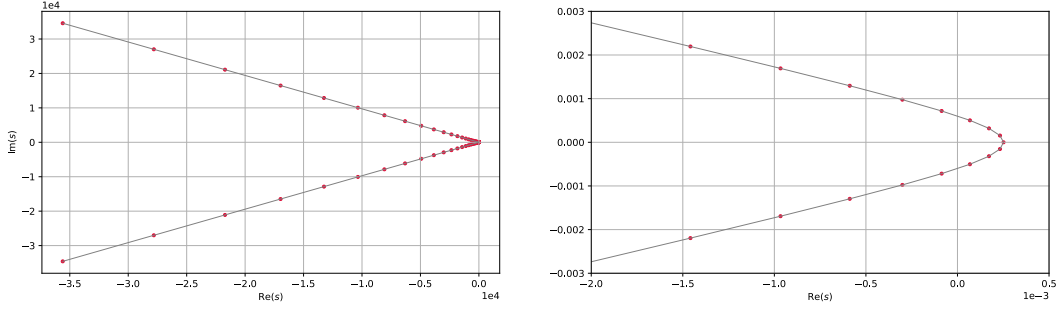


Figure 2: Left: Plot of the hyperbolic-shaped contour Γ in the Laplace transform plane defined by (5.73) with $\theta = 0.95$, $\alpha = 0.8$ and $\beta = 0.7$ in (5.76). The discretization points $\{s_\ell\}$ for the sum-of-exponentials approximation of $E_1(\sigma t)$ with $\sigma = 1$ and $n = 75$ are the red dots. Right: Zoomed plot showing the discretization near the origin.

Lemma 5.3. For $0 < \Delta t \ll 1$ and for $t \geq 2\Delta t$, we have

$$D_{L_j}(t) = B'_j(t)b_1 + B'_j(t - \Delta t)b_2 + \mathcal{O}((\Delta t)^3), \quad (5.83a)$$

where b_2 and b_1 are defined by

$$b_2 = \frac{\Delta t}{2}E_1(\sigma\Delta t) - \frac{e^{-\sigma\Delta t}}{2\sigma} + \frac{(1 - e^{-\sigma\Delta t})}{2\sigma^2\Delta t}, \quad b_1 = \Delta t E_1(\sigma\Delta t) + \frac{(1 - e^{-\sigma\Delta t})}{\sigma} - b_2. \quad (5.83b)$$

Moreover, for $t = \Delta t$, and with B_j satisfying the limiting behavior in (3.39), we have the exact relation

$$D_{L_j}(\Delta t) = E_1(\sigma\Delta t)B_j(\Delta t) + \int_0^{\Delta t} (B_j(\Delta t) - B_j(\Delta t - z)) \frac{e^{-\sigma z}}{z} dz. \quad (5.84)$$

Proof. On $0 \leq z \leq \Delta t$, and assuming $t \geq 2\Delta t$, we can approximate

$$B'_j(t - z) = B'_j(t) + \frac{z}{\Delta t} [B'_j(t - \Delta t) - B'_j(t)] + \mathcal{O}((\Delta t)^2),$$

in $D_{L_j}(t)$ of (5.82c). By integrating the resulting expression explicitly we get

$$D_{L_j}(t) = \frac{B'_j(t)}{\Delta t} \int_0^{\sigma\Delta t} E_1(\eta) d\eta + \frac{[B'_j(t - \Delta t) - B'_j(t)]}{\sigma^2\Delta t} \int_0^{\sigma\Delta t} \eta E_1(\eta) d\eta + \mathcal{O}((\Delta t)^3).$$

Using $\int_0^x E_1(\eta) d\eta = xE_1(x) + 1 - e^{-x}$ and $\int_0^x \eta E_1(\eta) d\eta = \frac{1}{2} [x^2 E_1(x) - (x+1)e^{-x} + 1]$, we get (5.83).

To derive (5.84), we integrate $D_{L_j}(\Delta t)$ by parts using $B_j(0) = 0$ to obtain

$$D_{L_j}(\Delta t) = -\lim_{z \rightarrow 0} E_1(\sigma z) [B_j(\Delta t) - B_j(\Delta t - z)] + E_1(\sigma\Delta t)B_j(\Delta t) + \int_0^{\Delta t} (B_j(\Delta t) - B_j(\Delta t - z)) \frac{e^{-\sigma z}}{z} dz. \quad (5.85)$$

Upon using the local behavior (3.39) for B_j , together with $E_1(\sigma z) \sim -\log(\sigma z) + \mathcal{O}(1)$ as $z \rightarrow 0$, we readily obtain that the first term on the right-hand side of (5.85) vanishes when either $u_{1j}(0) = 0$ or $u_{1j}(0) \neq 0$. This yields (5.84). In particular, for $u_{1j}(0) \neq 0$ we have the estimate

$$\lim_{z \rightarrow 0} E_1(\sigma z) [B_j(\Delta t) - B_j(\Delta t - z)] = -\frac{u_{1j}(0)\gamma_j}{\Delta t \log(\Delta t/(\kappa_j e^{-\gamma\epsilon}))} \lim_{z \rightarrow 0} [-z \log(\sigma z)] = 0.$$

□

For the history term $D_{Hj}(t)$, we substitute (5.75a) into (5.82b) to obtain

$$D_{Hj}(t) \approx \sum_{\ell=-n}^n e_{\ell} H_{Dj\ell}(t) \quad \text{where} \quad H_{Dj\ell}(t) \equiv \int_0^{t-\Delta t} B'_j(\tau) e^{s_{\ell}(t-\tau)} d\tau. \quad (5.86)$$

For each *history-mode* $H_{Dj\ell}(t)$ we adapt Lemma 5.1 to readily obtain for $t \geq \Delta t$ that

$$H_{Dj\ell}(t + \Delta t) = H_{Dj\ell}(t) e^{s_{\ell}\Delta t} + U_{Dj\ell}(t, \Delta t), \quad \text{with} \quad H_{Dj\ell}(\Delta t) = 0, \quad (5.87a)$$

where $U_{Dj\ell}(t, \Delta t) \equiv e^{2s_{\ell}\Delta t} \int_0^{\Delta t} e^{-s_{\ell}z} B'_j(t - \Delta t + z) dz.$

To approximate (5.87a) for $t \geq 2\Delta t$, we use the ETD2 scheme that ensures that the update integral $U_{Dj\ell}$ is exact for linear functions. This yields that

$$U_{Dj\ell}(t, \Delta t) \approx B'_j(t) b_{3\ell} + B'_j(t - \Delta t) b_{4\ell}, \quad \text{for} \quad t \geq 2\Delta t, \quad (5.87b)$$

where $b_{3\ell}$ and $b_{4\ell}$ are defined by

$$b_{3\ell} = \frac{e^{s_{\ell}\Delta t}}{s_{\ell}^2 \Delta t} (e^{s_{\ell}\Delta t} - 1 - s_{\ell}\Delta t), \quad b_{4\ell} = e^{s_{\ell}\Delta t} \frac{(e^{s_{\ell}\Delta t} - 1)}{s_{\ell}} - b_{3\ell}. \quad (5.87c)$$

For $t = \Delta t$, we integrate $U_{Dj\ell}(\Delta t, \Delta t)$ from (5.87a) by parts and use $B_j(0) = 0$ to get

$$U_{Dj\ell}(\Delta t, \Delta t) = e^{s_{\ell}\Delta t} B_j(\Delta t) + s_{\ell} e^{2s_{\ell}\Delta t} \int_0^{\Delta t} e^{-s_{\ell}z} B_j(z) dz. \quad (5.87d)$$

By using an ETD1 scheme to estimate $\int_0^{\Delta t} e^{-s_{\ell}z} B_j(z) dz \approx B_j(\Delta t) \int_0^{\Delta t} e^{-s_{\ell}z} dz$, we readily obtain after calculating the integral $\int_0^{\Delta t} e^{-s_{\ell}z} dz$ explicitly that

$$U_{Dj\ell}(\Delta t, \Delta t) \approx B_j(\Delta t) e^{2s_{\ell}\Delta t}. \quad (5.87e)$$

In this way, by combining (5.86)–(5.87b), we obtain for $t \geq 2\Delta t$ that

$$D_{Hj}(t + \Delta t) \approx \sum_{\ell=-n}^n e_{\ell} e^{s_{\ell}\Delta t} H_{Dj\ell}(t) + \left(\sum_{\ell=-n}^n e_{\ell} b_{3\ell} \right) B'_j(t) + \left(\sum_{\ell=-n}^n e_{\ell} b_{4\ell} \right) B'_j(t - \Delta t). \quad (5.88)$$

Moreover, we have

$$D_{Hj}(2\Delta t) \approx \left(\sum_{\ell=-n}^n e_{\ell} e^{2s_{\ell}\Delta t} \right) B_j(\Delta t), \quad D_{Hj}(\Delta t) = 0. \quad (5.89)$$

Finally, by using (5.83), (5.88) and (5.89) we readily obtain the marching scheme

$$D_j(t + \Delta t) \approx B'_j(t + \Delta t) b_1 + B'_j(t) \left(b_2 + \sum_{\ell=-n}^n e_{\ell} b_{3\ell} \right) + \left(\sum_{\ell=-n}^n e_{\ell} b_{4\ell} \right) B'_j(t - \Delta t) \\ + \sum_{\ell=-n}^n e_{\ell} e^{s_{\ell}\Delta t} H_{Dj\ell}(t), \quad t \geq 2\Delta t, \quad (5.90a)$$

$$D_j(2\Delta t) \approx B'_j(2\Delta t) b_1 + B'_j(\Delta t) b_2 + \left(\sum_{\ell=-n}^n e_{\ell} e^{2s_{\ell}\Delta t} \right) B_j(\Delta t),$$

$$D_j(\Delta t) = E_1(\sigma\Delta t) B_j(\Delta t) + \int_0^{\Delta t} (B_j(\Delta t) - B_j(\Delta t - z)) \frac{e^{-\sigma z}}{z} dz.$$

From (5.87) we have the following update rule for the next time-step:

$$H_{Dj\ell}(t + \Delta t) = H_{Dj\ell}(t) e^{s_{\ell}\Delta t} + \begin{cases} B'_j(t) b_{3\ell} + B'_j(t - \Delta t) b_{4\ell}, & t \geq 2\Delta t, \\ B_j(\Delta t) e^{2s_{\ell}\Delta t}, & t = \Delta t. \end{cases} \quad (5.90b)$$

In (5.90), b_1 , b_2 , $b_{3\ell}$ and $b_{4\ell}$ are defined in (5.83b) and (5.87c).

5.3 Time-marching scheme for $C_{jk}(t)$

A similar approach can be used to derive a time-marching scheme for $C_{jk}(t)$ defined in (4.46b). As in (5.82), we decompose $C_{jk}(t)$ as

$$C_{jk}(t) = C_{Hjk}(t) + C_{Ljk}(t), \quad (5.91a)$$

where for some Δt , with $0 < \Delta t \ll 1$, we define the local and history-dependent terms as

$$C_{Hjk}(t) \equiv \int_0^{t-\Delta t} B_k(\tau) G(a_{jk}, t - \tau) d\tau, \quad (5.91b)$$

$$C_{Ljk}(t) \equiv \int_{t-\Delta t}^t B_k(\tau) G(a_{jk}, t - \tau) d\tau = \int_0^{\Delta t} B_k(t - z) G(a_{jk}, z) dz. \quad (5.91c)$$

The marching scheme for the history term is derived in the same way as in §5.2. We have

$$C_{Hjk}(t) \approx \sum_{\ell=-n}^n \omega_{jk\ell} H_{Ck\ell}(t) \quad \text{where} \quad H_{Ck\ell}(t) \equiv \int_0^{t-\Delta t} B_k(\tau) e^{s_\ell(t-\tau)} d\tau. \quad (5.92)$$

For each *history-mode* $H_{Ck\ell}(t)$ we use Lemma 5.1 to obtain the update scheme

$$H_{Ck\ell}(t + \Delta t) = H_{Ck\ell}(t) e^{s_\ell \Delta t} + U_{Ck\ell}(t, \Delta t), \quad \text{with} \quad H_{Ck\ell}(\Delta t) = 0, \quad (5.93)$$

where $U_{Ck\ell}(t, \Delta t) \equiv e^{2s_\ell \Delta t} \int_0^{\Delta t} e^{-s_\ell z} B_k(t - \Delta t + z) dz.$

To approximate (5.93) for $t \geq 2\Delta t$, we use the ETD2 scheme to obtain

$$U_{Ck\ell}(t, \Delta t) \approx B_k(t) b_{3\ell} + B_k(t - \Delta t) b_{4\ell}, \quad \text{for} \quad t \geq 2\Delta t, \quad (5.94)$$

where $b_{3\ell}$ and $b_{4\ell}$ are defined in (5.87c). For $t = \Delta t$, we use an ETD1 scheme to get

$$U_{Ck\ell}(\Delta t, \Delta t) \approx B_k(\Delta t) b_{40\ell}, \quad \text{where} \quad b_{40\ell} \equiv e^{s_\ell \Delta t} \left(\frac{e^{s_\ell \Delta t} - 1}{s_\ell} \right). \quad (5.95)$$

The approximation of the local contribution $C_{Ljk}(t)$ is simpler than for D_{Ljk} owing to the exponential decay of $G(a_{jk}, z)$ for $z > 0$. We use an ETD1 scheme and estimate

$$C_{Ljk}(t) \approx B_k(t) \int_0^{\Delta t} G(a_{jk}, z) dz \approx B_k(t) E_1 \left(\frac{a_{jk}^2}{\Delta t} \right). \quad (5.96)$$

By using $E_1(z) \sim e^{-z}/z$ as $z \rightarrow \infty$, we conclude that $C_{Ljk}(t)$ is exponentially small when $a_{jk}^2/\Delta t \gg 1$. However, if the diffusivity D is large so that $a_{jk}^2/\Delta t$ is not so large, then we may need to use the higher order approximation for $C_{Ljk}(t)$ given by

$$C_{Ljk}(t) \approx B_k(t) E_1 \left(\frac{a_{jk}^2}{\Delta t} \right) - \left(\Delta t e^{-a_{jk}^2/\Delta t} - a_{jk}^2 E_1 \left(\frac{a_{jk}^2}{\Delta t} \right) \right) \left(\sigma B_k(t) + \frac{B_k(t) - B_k(t - \Delta t)}{\Delta t} \right). \quad (5.97)$$

In this way, by combining (5.92)–(5.95) for the history modes and (5.96) for the local term, and using only the leading-order result for $C_{Ljk}(t)$, we obtain the following marching scheme for $C_{jk}(t)$ for $t \geq \Delta t$:

$$\begin{aligned}
C_{jk}(t + \Delta t) &\approx B_k(t + \Delta t) E_1 \left(\frac{a_{jk}^2}{\Delta t} \right) + \left(\sum_{\ell=-n}^n \omega_{jkl} b_{3\ell} \right) B_k(t) \\
&\quad + \left(\sum_{\ell=-n}^n \omega_{jkl} b_{4\ell} \right) B_k(t - \Delta t) + \sum_{\ell=-n}^n \omega_{jkl} e^{s_\ell \Delta t} H_{Ck\ell}(t), \quad \text{for } t \geq 2\Delta t, \\
C_{jk}(2\Delta t) &\approx B_k(2\Delta t) E_1 \left(\frac{a_{jk}^2}{\Delta t} \right) + \left(\sum_{\ell=-n}^n \omega_{jkl} b_{40\ell} \right) B_k(\Delta t), \\
C_{jk}(\Delta t) &\approx B_k(\Delta t) E_1 \left(\frac{a_{jk}^2}{\Delta t} \right).
\end{aligned} \tag{5.98a}$$

In addition, from (5.94) and (5.95), we have the update rule

$$H_{Ck\ell}(t + \Delta t) = \begin{cases} H_{Ck\ell}(t) e^{s_\ell \Delta t} + B_k(t) b_{3\ell} + B_k(t - \Delta t) b_{4\ell}, & t \geq 2\Delta t, \\ B_k(\Delta t) b_{40\ell}, & t = \Delta t. \end{cases} \tag{5.98b}$$

Here $b_{3\ell}$, $b_{4\ell}$ and $b_{40\ell}$ are defined in (5.83b), (5.87c) and (5.95), respectively.

5.4 Marching scheme for integro-differential system

By substituting (5.98) and (5.90) into (5.71), and recalling (3.36a) for the ODE intracellular dynamics, we now develop a time-marching algorithm for approximating solutions to (3.36). Let $\{t_0, \dots, t_q\}$ be a discretization of the time domain $[0, T]$ where T is some final time of choice. Then, $t_0 = 0$, $t_q = T$, $t_{i+1} - t_i = \Delta t$ for $i \in \{0, \dots, q-1\}$, where $\Delta t = T/q$ and $t_i = i\Delta t$. In the formulation of our algorithm we will use $B'_j(t_i) \approx (B_j(t_i) - B_j(t_{i-1})) / \Delta t$, for $i \geq 2$ in (5.90). Below, we denote the numerical approximation to $u_{1j}(t_i)$ by $u_{1j}^{(i)}$ and the vector of all $u_{1j}^{(i)}$ for $j \in \{1, \dots, N\}$ by $\mathbf{u}_1^{(i)}$. We use a similar notation for the reaction kinetic functions.

Step 1; $0 \curvearrowright \Delta t$: For this first time-step we discretize the reaction kinetics in each cell by the explicit Runge-Kutta RK4 method [66] and use

$$\begin{aligned}
\mathbf{u}_1^{(1)} &= \mathbf{u}_1^{(0)} + \frac{\Delta t}{6} (k_1^{(0)} + 2k_2^{(0)} + 2k_3^{(0)} + k_4^{(0)}) + \mathbf{B}^{(0)} \Delta t, \\
\mathbf{u}_2^{(1)} &= \mathbf{u}_2^{(0)} + \frac{\Delta t}{6} (\tilde{k}_1^{(0)} + 2\tilde{k}_2^{(0)} + 2\tilde{k}_3^{(0)} + \tilde{k}_4^{(0)}),
\end{aligned} \tag{5.99}$$

where the RK4 weights are

$$\begin{aligned}
k_1^{(0)} &= \mathbf{F}_1(\mathbf{u}_1^{(0)}, \mathbf{u}_2^{(0)}), \quad \tilde{k}_1^{(0)} = \mathbf{F}_2(\mathbf{u}_1^{(0)}, \mathbf{u}_2^{(0)}), \\
k_2^{(0)} &= \mathbf{F}_1(\mathbf{u}_1^{(0)} + \frac{\Delta t}{2} k_1^{(0)}, \mathbf{u}_2^{(0)} + \frac{\Delta t}{2} \tilde{k}_1^{(0)}), \quad \tilde{k}_2^{(0)} = \mathbf{F}_2(\mathbf{u}_1^{(0)} + \frac{\Delta t}{2} k_1^{(0)}, \mathbf{u}_2^{(0)} + \frac{\Delta t}{2} \tilde{k}_1^{(0)}), \\
k_3^{(0)} &= \mathbf{F}_1(\mathbf{u}_1^{(0)} + \frac{\Delta t}{2} k_2^{(0)}, \mathbf{u}_2^{(0)} + \frac{\Delta t}{2} \tilde{k}_2^{(0)}), \quad \tilde{k}_3^{(0)} = \mathbf{F}_2(\mathbf{u}_1^{(0)} + \frac{\Delta t}{2} k_2^{(0)}, \mathbf{u}_2^{(0)} + \frac{\Delta t}{2} \tilde{k}_2^{(0)}), \\
k_4^{(0)} &= \mathbf{F}_1(\mathbf{u}_1^{(0)} + \Delta t k_3^{(0)}, \mathbf{u}_2^{(0)} + \Delta t \tilde{k}_3^{(0)}), \quad \tilde{k}_4^{(0)} = \mathbf{F}_2(\mathbf{u}_1^{(0)} + \Delta t k_3^{(0)}, \mathbf{u}_2^{(0)} + \Delta t \tilde{k}_3^{(0)}).
\end{aligned}$$

In (5.99) we imposed the explicit short-time behavior for $\mathbf{B}^{(0)}$ given in (3.39), which is valid since $\mathcal{O}(\varepsilon^2) \ll \Delta t \ll \mathcal{O}(1)$. The truncation error for this approximation is $\mathcal{O}(\Delta t)$, whereas RK4 gives a truncation error of $\mathcal{O}(\Delta t^5)$ for the reaction kinetics.

In terms of the computed $\mathbf{u}_1^{(1)} \approx \mathbf{u}_1(t_1)$, in Appendix C we derive an improved approximation for $\mathbf{B}^{(1)} = (B_1^{(1)}, \dots, B_N^{(1)})^T$, in which the components are

$$B_j^{(1)} = -\frac{u_{1j}^{(1)} \gamma_j}{\log(\Delta t / (\kappa_j e^{-\gamma_e}))} \left(1 - \frac{\pi^2}{6 [\log(\Delta t / (\kappa_j e^{-\gamma_e}))]^2} \right). \tag{5.100}$$

Step 2; $\Delta t \rightsquigarrow 2\Delta t$: We use an RK4 scheme for the reaction kinetics with RK4 weights as given in the first time step, and use a lagged $\mathbf{B}^{(1)}$ so that

$$\begin{aligned}\mathbf{u}_1^{(2)} &= \mathbf{u}_1^{(1)} + \frac{\Delta t}{6}(k_1^{(1)} + 2k_2^{(1)} + 2k_3^{(1)} + k_4^{(1)}) + \mathbf{B}^{(1)}\Delta t, \\ \mathbf{u}_2^{(2)} &= \mathbf{u}_2^{(1)} + \frac{\Delta t}{6}(\tilde{k}_1^{(1)} + 2\tilde{k}_2^{(1)} + 2\tilde{k}_3^{(1)} + \tilde{k}_4^{(1)}).\end{aligned}\tag{5.101}$$

In terms of the computed $\mathbf{u}_1^{(2)}$, we determine \mathbf{B}^2 from the linear system

$$\mathbf{B}^{(2)} = A^{-1} \left(M_1 \mathbf{B}^{(1)} + \Delta t \Gamma \mathbf{u}_1^{(2)} - b_2 \Delta t \mathbf{B}'(\Delta t) \right), \tag{5.102}$$

where the components of $\mathbf{B}'(\Delta t)$ are given in (3.40). In (5.102), $\Gamma \equiv \text{diag}(\gamma_1, \dots, \gamma_N)$, while the matrices A and M_1 have the following entries for $k \neq j \in \{1, \dots, N\}$:

$$\begin{aligned}A_{jj} &= b_1 - \eta_j \Delta t, & A_{jk} &= -\Delta t E_1 \left(a_{jk}^2 / \Delta t \right), \\ M_{1,jj} &= b_1 - \Delta t \left(\sum_{\ell=-n}^n e_{\ell} e^{2s_{\ell} \Delta t} \right), & M_{1,jk} &= \Delta t \sum_{\ell=-n}^n \omega_{jk\ell} b_{40\ell}.\end{aligned}\tag{5.103}$$

Recursive step; $t_i \rightsquigarrow t_{i+1}$, for $i \geq 2$: We use the RK4 method with a lagged $\mathbf{B}^{(i)}$, so that

$$\begin{aligned}\mathbf{u}_1^{(i+1)} &= \mathbf{u}_1^{(i)} + \frac{\Delta t}{6}(k_1^{(i)} + 2k_2^{(i)} + 2k_3^{(i)} + k_4^{(i)}) + \mathbf{B}^{(i)}\Delta t, \\ \mathbf{u}_2^{(i+1)} &= \mathbf{u}_2^{(i)} + \frac{\Delta t}{6}(\tilde{k}_1^{(i)} + 2\tilde{k}_2^{(i)} + 2\tilde{k}_3^{(i)} + \tilde{k}_4^{(i)}).\end{aligned}\tag{5.104}$$

In terms of the computed $\mathbf{u}_1^{(i+1)}$ we calculate $\mathbf{B}^{(i+1)}$ as

$$\mathbf{B}^{(i+1)} = A^{-1} \left(M \mathbf{B}^{(i)} + \mathcal{N} \mathbf{B}^{(i-1)} + \left(\sum_{\ell=-n}^n e_{\ell} b_{4\ell} \right) \mathbf{B}^{(i-2)} + \Delta t \Gamma \mathbf{u}_1^{(i+1)} - \Delta t \mathbf{H}^{(i)} \right), \tag{5.105}$$

where the matrices M and \mathcal{N} have the entries

$$\begin{aligned}M_{jj} &= b_1 - b_2 - \sum_{\ell=-n}^n e_{\ell} b_{3\ell}, & M_{jk} &= \Delta t \sum_{\ell=-n}^n \omega_{jk\ell} b_{3\ell}, \\ \mathcal{N}_{jj} &= b_2 + \sum_{\ell=-n}^n e_{\ell} (b_{3\ell} - b_{4\ell}), & \mathcal{N}_{jk} &= \Delta t \sum_{\ell=-n}^n \omega_{jk\ell} b_{4\ell},\end{aligned}\tag{5.106}$$

for $k \neq j \in \{1, \dots, N\}$. In (5.105) the history vector $\mathbf{H}^{(i)} \equiv (H_1^{(i)}, \dots, H_N^{(i)})^T$ has entries

$$H_j^{(i)} = \sum_{\ell=-n}^n \left(e_{\ell} e^{s_{\ell} \Delta t} H_{Dj\ell}^{(i)} - \sum_{k=1, k \neq j}^N \omega_{jk\ell} e^{s_{\ell} \Delta t} H_{Ck\ell}^{(i)} \right), \tag{5.107a}$$

and is updated with the scheme

$$\mathbf{H}_{D\ell}^{(i)} = \mathbf{H}_{D\ell}^{(i-1)} e^{s_{\ell} \Delta t} + b_{3\ell} \frac{(\mathbf{B}^{(i-1)} - \mathbf{B}^{(i-2)})}{\Delta t} + \begin{cases} b_{4\ell} \frac{(\mathbf{B}^{(i-2)} - \mathbf{B}^{(i-3)})}{\Delta t}, & \text{if } i \geq 4, \\ \mathbf{B}'(\Delta t) b_{4\ell} & \text{if } i = 3, \end{cases} \tag{5.107b}$$

$$\mathbf{H}_{D\ell}^{(2)} = e^{2s_{\ell} \Delta t} \mathbf{B}(\Delta t),$$

together with

$$\begin{aligned}\mathbf{H}_{C\ell}^{(i)} &= \mathbf{H}_{C\ell}^{(i-1)} e^{s_{\ell} \Delta t} + b_{3\ell} \mathbf{B}^{(i-1)} + b_{4\ell} \mathbf{B}^{(i-2)}, & \text{if } i \geq 3, \\ \mathbf{H}_{C\ell}^{(2)} &= b_{40\ell} \mathbf{B}(\Delta t).\end{aligned}\tag{5.107c}$$

Overall, our formulation is an operator-splitting scheme of a semi-implicit kind in the sense that the right-hand sides of the reaction kinetic vector fields are treated explicitly using the RK4 method with a lagged $\mathbf{B}^{(i-1)}$, while in (5.105) $\mathbf{u}_1^{(i)}$ appears implicitly in the update to $\mathbf{B}^{(i)}$.

6 Numerical results: Sel'kov intracellular dynamics

To illustrate our analysis of (1.5), we will consider the two-component Sel'kov kinetics. For this choice, the intracellular kinetics $\mathbf{F}_j(u_{1j}, u_{2j}) \equiv (F_{1j}(u_{1j}, u_{2j}), F_{2j}(u_{1j}, u_{2j}))^T$ are given by

$$F_{1j} = \alpha_j u_{2j} + u_{2j} u_{1j}^2 - u_{1j}, \quad F_{2j} = \zeta_j [\mu_j - (\alpha_j u_{2j} + u_{2j} u_{1j}^2)]. \quad (6.108)$$

We refer to $\alpha_j > 0$, $\zeta_j > 0$ and $\mu_j > 0$ as the *reaction-kinetic parameters* for the j^{th} cell.

6.1 An Isolated Cell

For an isolated cell uncoupled from the bulk, the unique steady-state for $d\mathbf{u}_j/dt = \mathbf{F}_j$ is $u_{1j} = \mu_j$ and $u_{2j} = \mu_j / (\alpha_j + \mu_j^2)$. At this steady-state we calculate

$$\det(J_j) = \zeta_j (\alpha_j + \mu_j^2), \quad \text{tr}(J_j) = \frac{1}{\alpha_j + \mu_j^2} (2\mu_j \mu_j - (\alpha_j + \mu_j^2) - \zeta_j (\alpha_j + \mu_j^2)^2), \quad (6.109)$$

for the determinant and trace of the Jacobian J_j of the kinetics. Since $\det(J_j) > 0$, the unique steady-state for an isolated cell is linearly stable if and only if $\text{tr}(J_j) < 0$. The Hopf bifurcation boundary in the α_j versus μ_j parameter plane occurs when $\text{tr}(J_j) = 0$. From the Poincaré-Bendixson theorem, we conclude that whenever the steady-state is unstable the isolated cell will have limit cycle oscillations. For $\zeta_j = 0.15$, in Fig. 3(a) we show the region in the α_j versus μ_j plane where limit cycle oscillations occur. In Fig. 3(b) we plot the limit cycle in the u_{2j} versus u_{1j} plane for $\alpha_j = 0.4$ and $\mu_j = 2.0$.

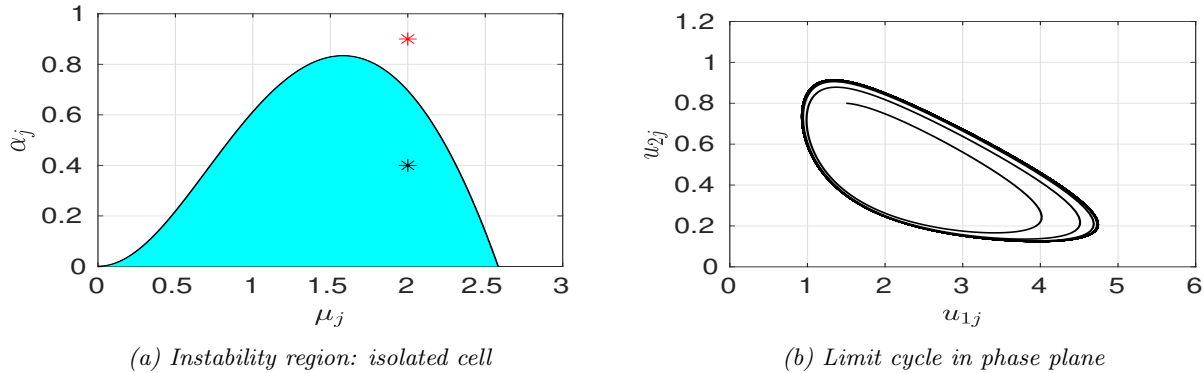


Figure 3: Left: Blue-shaded region of instability in the α_j versus μ_j plane for the steady-state of an isolated cell when $\zeta_j = 0.15$. In this region, since $\text{tr}(J_j) > 0$ the unique steady-state is unstable, and a time-periodic (limit cycle) solution occurs for an isolated cell. In the unshaded region the steady-state is linearly stable for an isolated cell. Right: For $\alpha_j = 0.4$ and $\mu_j = 2.0$ (black star in left panel), there is a limit cycle in the u_{2j} versus u_{1j} plane.

Next, we determine how the instability region for an isolated cell changes when we include the effect of efflux across the cell membrane, but neglect any influx from the bulk medium (recall the schematic in Fig. 1(b)). Setting $U = 0$ in (1.5c), for an isolated cell with boundary efflux the unique steady-state for $d\mathbf{u}_j/dt = \mathbf{F}_j - 2\pi d_{2j} u_{1j} \mathbf{e}_1$ is now $u_{1j} = \mu_j / (1 + 2\pi d_{2j})$ and $u_{2j} = \mu_j / (\alpha_j + u_{1j}^2)$. The Hopf bifurcation boundary in the α_j versus d_{2j} plane occurs when $\text{tr}(J_j) = 0$, which yields

$$\alpha_j = -\frac{\mu_j^2}{(1 + 2\pi d_{2j})^2} + \frac{1}{2\zeta_j} \left[-(1 + 2\pi d_{2j}) + \sqrt{(1 + 2\pi d_{2j})^2 + \frac{8\mu_j^2 \zeta_j}{1 + 2\pi d_{2j}}} \right]. \quad (6.110)$$

For $\zeta_j = 0.15$ and $\mu_j = 2.0$, in Fig. 4 we show that when d_{2j} increases past a threshold, the range of α_j where intracellular oscillations occur decreases significantly when there is efflux from an isolated cell.

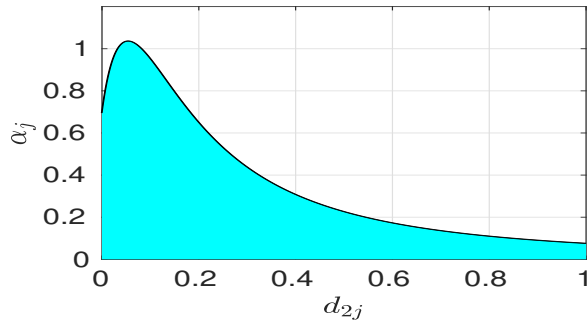


Figure 4: Blue-shaded region of instability in the α_j versus d_{2j} plane for the steady-state of an isolated cell with boundary efflux when $\zeta_j = 0.15$ and $\mu_j = 2.0$. As d_{2j} increases past a threshold, the range in α_j where limit cycle oscillations will occur for the isolated cell decreases.

6.2 Steady-states and their stability with cell-bulk coupling

With cell-bulk coupling, the steady-state solutions of (1.5) are obtained from the solution to the NAS (4.52) and (4.54) where \mathbf{F}_j is given in (6.108). We readily obtain that

$$u_{1js} = \mu_j + B_{js}, \quad u_{2js} = \frac{\mu_j}{\alpha_j + u_{1js}^2}, \quad (6.111a)$$

where, with η_j and γ_j as defined in (3.36c), the steady-state source strengths B_{js} satisfy

$$(\gamma_j + \eta_j) B_{js} + 2 \sum_{\substack{k=1 \\ k \neq j}}^N B_{ks} K_0 \left(\sqrt{\frac{\sigma}{D}} |\mathbf{x}_j - \mathbf{x}_k| \right) = -\gamma_j \mu_j, \quad j \in \{1, \dots, N\}. \quad (6.111b)$$

We remark that although (4.54) and (4.52) generally yields a nonlinear algebraic system characterizing steady-state solutions, with Sel'kov kinetics one must only solve the linear algebraic system (6.111b).

To analyze the linear stability of this steady-state solution, we must solve the nonlinear eigenvalue problem (4.64a) of Proposition 3. In calculating $\mathcal{M}(\lambda)$ from (4.64b), it is only the diagonal matrix $\mathcal{K}(\lambda)$ defined in (4.65b) that depends on the choice of the intracellular kinetics. For the Sel'kov kinetics (6.108),

$$\mathcal{K}(\lambda) \equiv \text{diag}(K_1, \dots, K_N), \quad \text{where} \quad K_j \equiv \frac{\lambda + \det(J_j)}{\lambda^2 - \text{tr}(J_j)\lambda + \det(J_j)}, \quad (6.112)$$

where $\det(J_j)$ and $\text{tr}(J_j)$, evaluated at the steady-state of the cell-bulk model, are now given by

$$\det(J_j) = \zeta_j (\alpha_j + u_{1js}^2) > 0, \quad \text{tr}(J_j) = \frac{1}{\alpha_j + u_{1js}^2} \left(2\mu_j u_{1js} - (\alpha_j + u_{1js}^2) - \zeta_j (\alpha_j + u_{1js}^2)^2 \right). \quad (6.113)$$

Here $u_{1js} = \mu_j + B_{js}$, where B_{js} for $j \in \{1, \dots, N\}$ are obtained from (6.111b). Since the linear system (6.111b) is always solvable, there are no transcritical or fold bifurcation points along the steady-state solution branch as parameters are varied for Sel'kov kinetics. As such, since $\lambda = 0$ is never a root of $\det \mathcal{M}(\lambda) = 0$, the steady-state solution is never destabilized by a zero-eigenvalue crossing (see Proposition 1 of [33]).

In this way, for reaction-kinetic parameters for which each isolated cell has a stable steady-state, any instability that arises from the cell-bulk coupling must occur through a Hopf bifurcation. As a result, we will identify stability boundaries in the $1/\sigma$ versus D parameter plane for steady-state solutions with Sel'kov kinetics by seeking Hopf bifurcation (HB) thresholds for which $\lambda = i\lambda_I \in \Lambda(\mathcal{M})$ with $\lambda_I \in \mathbb{R}$. For arbitrary locations \mathbf{x}_j , with $j \in \{1, \dots, N\}$, of a collection of non-identical cells, with possibly cell-dependent permeability and reaction-kinetic parameters, we must compute all paths in the $1/\sigma$ versus D parameter space where $\det \mathcal{M}(i\lambda_I) = 0$ for some $\lambda_I > 0$. HB boundaries in parameter space can

readily be computed numerically for a ring arrangement of identical cells, with and without a defective center cell, as the matrix spectrum of $\mathcal{M}(\lambda)$ is known analytically (cf. [33]). When explicit analytical formulae are known for the eigenvalues of $\mathcal{M}(\lambda)$, simple scalar root-finding algorithms can be used to determine the HB thresholds in parameter space using a pseudo-arclength continuation scheme in D (see [33] for details). However, for a general spatial arrangement of non-identical cells, the numerical solution of the nonlinear matrix eigenvalue problem $\det \mathcal{M}(i\lambda_I) = 0$ in the $1/\sigma$ versus D parameter space is highly challenging. Nonlinear matrix eigenvalue problems and effective solution strategies for various classes of matrices are discussed in [6], [5] and [28].

To determine regions of instability in open sets of the $1/\sigma$ versus D parameter plane off of the HB boundaries and to count the number, \mathcal{Z} , of destabilizing eigenvalues of the linearization of the cell-bulk model (1.5) around the steady-state, as defined by the number of $\lambda \in \Lambda(\mathcal{M})$ with $\text{Re}(\lambda) > 0$ (counting multiplicity), we use the argument principle of complex analysis applied to $\mathcal{F}(\lambda) \equiv \det(\mathcal{M}(\lambda))$, where $\mathcal{M}(\lambda)$ is the complex symmetric GCEP matrix (4.64b) in which $\mathcal{K}(\lambda)$ is given in (6.112). In the right-half plane, we take the contour $\Gamma_{\mathcal{R}}$ as the union of the imaginary axis $\Gamma_I = i\lambda_I$, for $|\lambda_I| \leq \mathcal{R}$, and the semi-circle $C_{\mathcal{R}}$, defined by $|\lambda| = \mathcal{R} > 0$ with $|\arg(\lambda)| \leq \pi/2$. Provided that there are no zeroes or poles on $\Gamma_{\mathcal{R}}$ for $\mathcal{F}(\lambda)$, the argument principle yields that the number $\mathcal{Z}_{\mathcal{R}}$ of zeroes of $\mathcal{F}(\lambda) = 0$ inside $\Gamma_{\mathcal{R}}$ is

$$\mathcal{Z}_{\mathcal{R}} = \frac{1}{2\pi} [\arg \mathcal{F}(\lambda)]_{\Gamma_{\mathcal{R}}} + \mathcal{P}_{\mathcal{R}}. \quad (6.114)$$

Here $\mathcal{P}_{\mathcal{R}}$ is the number of poles of $\mathcal{F}(\lambda)$ inside $\Gamma_{\mathcal{R}}$, while $[\arg \mathcal{F}(\lambda)]_{\Gamma_{\mathcal{R}}}$ denotes the change in the argument of $\mathcal{F}(\lambda)$ over the counter-clockwise oriented contour $\Gamma_{\mathcal{R}}$. We pass to the limit $\mathcal{R} \rightarrow \infty$ and use (6.112) to obtain that $\mathcal{K}(\lambda) \rightarrow 0$ as $\mathcal{R} \rightarrow \infty$ on the semi-circle $C_{\mathcal{R}}$. Moreover, for $\mathcal{R} \gg 1$, (4.66) and (4.64b) yields that $\mathcal{M}(\lambda) \approx -(\nu/2) \log(\mathcal{R}) I + \mathcal{O}(1)$ on $C_{\mathcal{R}}$. As a result, we conclude that $\lim_{\mathcal{R} \rightarrow \infty} [\arg \mathcal{F}(\lambda)]_{C_{\mathcal{R}}} = 0$. Finally, to evaluate the change of argument on the imaginary axis we use $\mathcal{F}(\bar{\lambda}) = \overline{\mathcal{F}(\lambda)}$ with $\lambda = i\lambda_I$ to reduce the computation to the positive imaginary axis. In this way, by letting $\mathcal{R} \rightarrow \infty$ we get that the number of zeroes \mathcal{Z} of $\mathcal{F}(\lambda)$ in $\text{Re}(\lambda) > 0$ is

$$\mathcal{Z} = \mathcal{P} - \frac{1}{\pi} [\arg \mathcal{F}(i\lambda_I)]_{\Gamma_{I+}}, \quad (6.115)$$

where \mathcal{P} denotes the number of poles (counting multiplicity) of $\mathcal{F}(\lambda)$ in $\text{Re}(\lambda) > 0$, and Γ_{I+} denotes the entire positive imaginary axis now directed upwards starting from $\lambda_I = 0$. To determine \mathcal{P} , we observe that since \mathcal{G}_{λ} is analytic in $\text{Re}(\lambda) > 0$ any singularity of $\mathcal{F}(\lambda)$ must arise from the poles of the diagonal matrix $\mathcal{K}(\lambda)$ with entries given in (6.112). Since $\det(J_j) > 0$, we conclude that $\mathcal{P} = 2p$ where p is the total number of integers $j \in \{1, \dots, N\}$ for which $\text{tr}(J_j) > 0$. For a given parameter set, we will use (6.115) to numerically calculate \mathcal{Z} in a fine discretization of the $1/\sigma$ versus D parameter plane. Below, we refer to this “phase diagram” as a *scatter plot*. For the cell configurations considered below, where the matrix spectrum of $\mathcal{M}(\lambda)$ is known, the determinant is readily evaluated at a fine discretization along the imaginary axis. The axis-crossing algorithm of [3] can then be used to compute the winding number.

In the results given below in §6.3–6.6 we have fixed the cell radius as $\varepsilon = 0.03$ and the Sel’kov reaction-kinetic parameters as $\mu_j = 2$ and $\zeta_j = 0.15$ for $j \in \{1, \dots, N\}$. We will explore the effect of changing the kinetic parameter α_j and the influx and efflux parameters d_{1j} and d_{2j} , respectively. More specifically, we will study the effect of choosing pairs (d_{2j}, α_j) either inside or outside the blue-shaded region of instability, as shown in Fig. 4, for an isolated cell with boundary efflux. Initial conditions will be chosen near the steady-state values so that the scatter plots are informative for predicting the onset of any instability.

6.3 Two-Cell Configurations

For the linearization of the steady-state for the two-cell configuration of Fig. 5(a), and for three values of the influx parameter d_{1j} , in Fig. 6 we plot the HB boundaries for the in-phase mode (solid curves) and the anti-phase mode (dashed curves) in the $1/\sigma$ versus D parameter plane when two identical cells

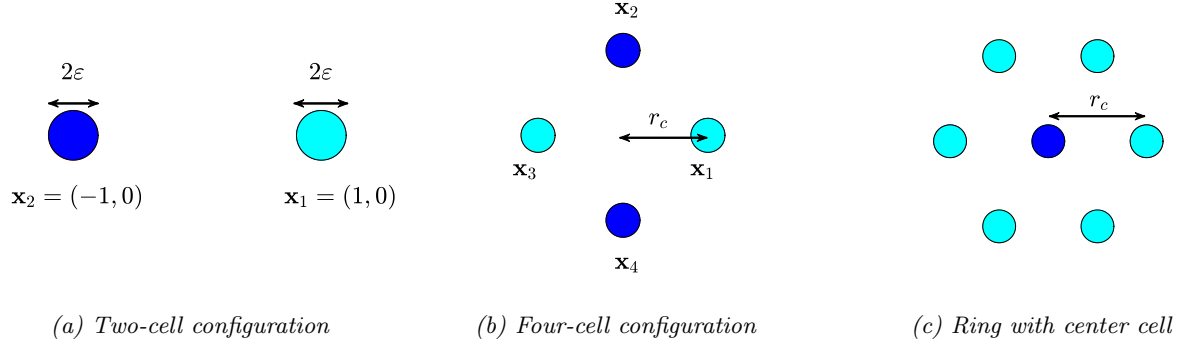


Figure 5: Left: A two-cell configuration. Middle: four equally-spaced cells on a ring of radius r_c . Right: Hexagonal ring arrangement of identical cells where the center cell is a pacemaker or signaling cell. Equally-colored pairs of cells are taken to have identical permeabilities and reaction-kinetic parameters.

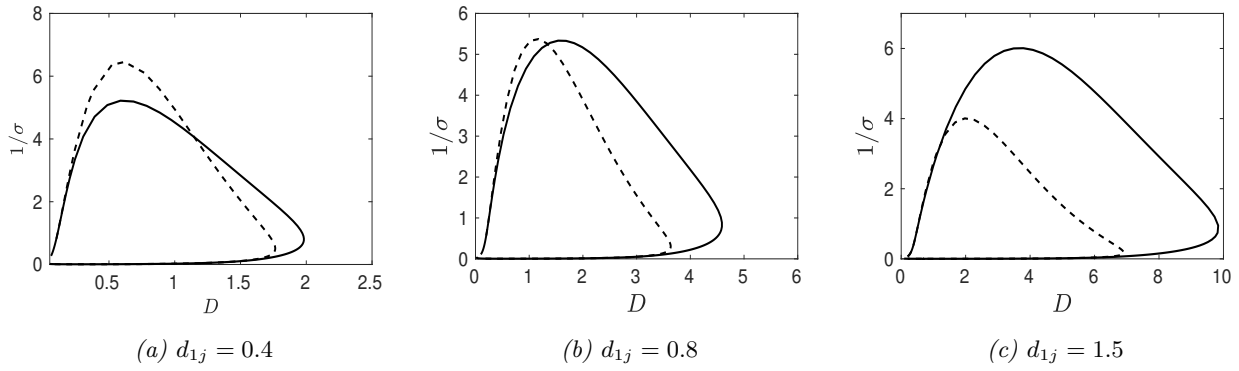


Figure 6: Left: HB boundaries in the $1/\sigma$ versus D parameter plane for the linearization of the steady-state for the two-cell configuration of Fig. 5(a) for identical cells with permeabilities $d_{1j} = 0.4$, $d_{2j} = 0.2$ and kinetic parameter $\alpha_j = 0.9$. The HB boundaries for the in-phase $\mathbf{c} = (1, 1)^T$ and anti-phase $\mathbf{c} = (1, -1)^T$ modes are the solid and dashed curves, respectively. The steady-state is unstable to the specific mode inside each lobe. Middle: $d_{1j} = 0.8$. Right: $d_{1j} = 1.5$. The range in D of the lobes of instability increases with the influx parameter d_{1j} .

are initially in a quiescent state when uncoupled from the bulk. The other parameters are given in the figure caption. The steady-state is unstable to in-phase and the anti-phase perturbations only inside the corresponding lobes, while the steady-state is linearly stable outside the union of the two lobes. From Fig. 6 we observe the possibility of either a purely anti-phase instability or a purely in-phase instability for some parameter pairs $(1/\sigma, D)$. Upon comparing Figs. 6(a)–6(c), the range in D where the lobes of instability occur become larger as d_{1j} is increased.

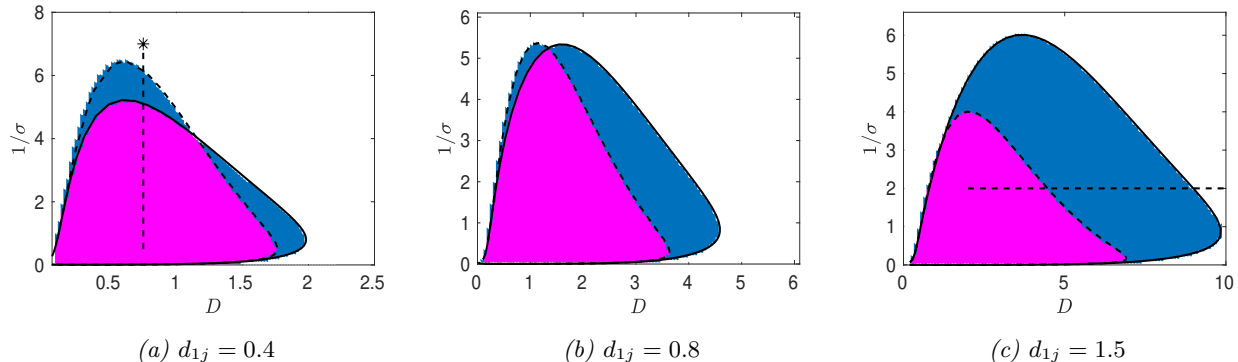


Figure 7: Scatter plot of the number \mathcal{Z} of destabilizing eigenvalues satisfying $\text{Re}(\lambda) > 0$ in the $1/\sigma$ versus D parameter plane corresponding to the linearization of the steady-state for the two-cell configuration of Fig. 5(a) for identical cells with parameter values $d_{1j} = 0.4$ (left), $d_{1j} = 0.8$ (middle), $d_{1j} = 1.5$ (right). Here, $\mathcal{Z} = 0$ is white, $\mathcal{Z} = 2$ is blue, and $\mathcal{Z} = 4$ is magenta. The HB boundaries are superimposed. Remaining parameters are as in Fig. 6.

For Fig. 7 we numerically implemented the winding number criterion (6.115) to provide a scatter plot in the $1/\sigma$ versus D plane that indicates the number of destabilizing eigenvalues in $\text{Re}(\lambda) > 0$ associated with the linearization of the steady-state. In Fig. 8 we plot the path of both the real and imaginary parts of the two dominant eigenvalues $\lambda \in \mathbb{C}$ along the parameter path indicated by the vertical and horizontal dotted lines in Fig. 7(a) and Fig. 7(c), respectively. Along the vertical path in Fig. 7(a), we observe from Fig. 8(a) that the in-phase and anti-phase modes of instability have comparable growth rates when $D = 0.75$ and $\sigma = 0.5$ and that the in-phase mode becomes stable before the anti-phase mode as $1/\sigma$ is increased. Since the imaginary part $\text{Im}(\lambda)$ is roughly the same for both modes, and shows little variation with σ , we conclude that the temporal frequencies of small amplitude oscillations are roughly similar for both modes. In contrast, along the horizontal parameter path in Fig. 7(c), we observe from Fig. 8(c) that the growth rate for the in-phase mode is larger than that for the anti-phase mode as D is increased.

We now compare our numerical solution of the reduced integro-differential system (3.36), as computed using our algorithm in §5.4, with that of the full cell-bulk system (1.5), as computed with the commercial PDE solver FlexPDE Professional 6.50/L64 [18] using the domain-truncation approach given in Appendix D. The comparison is made at the star-labeled point shown in Fig. 7(a) where rather intricate long-time dynamics occur. For the algorithm in §5.4, we used a time step size $\Delta t = 0.002$ and chose $n = 75$ for the discretization of the Laplace space contour for the sum-of-exponentials approximation (see Fig. 2). In Fig. 9 we show a very close qualitative agreement between our hybrid asymptotic-numerical results and the full numerical results. We observe that our hybrid approach is able to capture a transiently decaying oscillation, which transitions to a mixed-mode oscillation on some intermediate time scale, and that ultimately tends to a steady-state solution as obtained from the solution to (6.111b). These final steady-state values correctly approximate the FlexPDE computed steady-state to several decimal places of accuracy. This intricate mixed-mode behavior over the rather long time scale seen in Fig. 9 stems from the proximity to the anti-phase Hopf bubble in parameter space as shown in Fig. 7(a), together with the two dominant, but rather small magnitude, closely-spaced eigenvalues shown in Fig. 8(a) with $\sigma = 1/7$. As a more quantitative validation of our hybrid approach, in Fig. 10 we show a very close comparison for the amplitude and period of the intracellular species u_{11} and u_{12} as extracted numerically from both our fast algorithm for (3.36) and from the full FlexPDE solution to

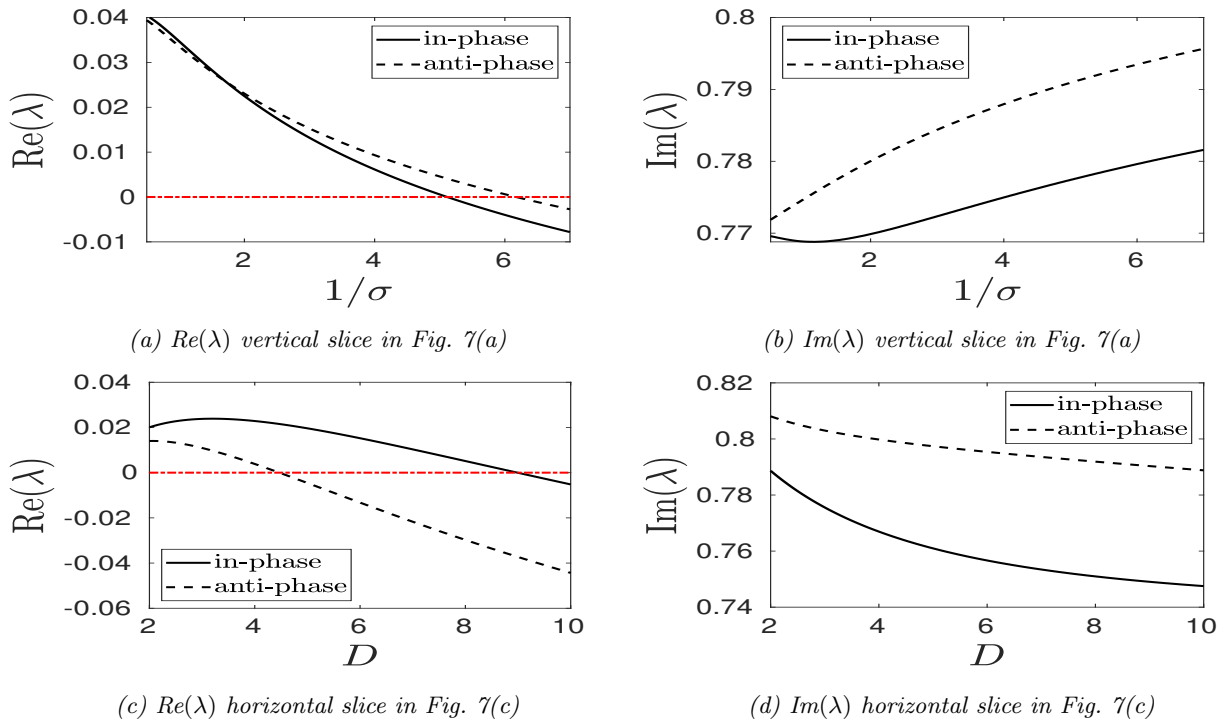


Figure 8: Top row: two dominant eigenvalues, $\text{Re}(\lambda)$ (left) and $\text{Im}(\lambda)$ (right), computed by solving $\det \mathcal{M}(\lambda) = 0$ along the vertical dotted path with $D = 0.75$ indicated in Fig. 7(a). Bottom row: two dominant eigenvalues, $\text{Re}(\lambda)$ (left) and $\text{Im}(\lambda)$ (right), computed by solving $\det \mathcal{M}(\lambda) = 0$ along the horizontal dotted path with $\sigma = 0.5$ as shown in Fig. 7(c). The horizontal red lines in the left panels is the marginal stability threshold $\text{Re}(\lambda) = 0$.

(1.5).

Overall we conclude that both the integro-differential system, as derived in (3.36) under the asymptotic assumption $\varepsilon \ll 1$, and the mixed-order numerical time-marching scheme formulated in §5.4, are able to replicate with a high degree of accuracy detailed fine features in intracellular oscillations for the full cell-bulk model (1.5) over long time intervals. We emphasize that for the FlexPDE solution, the time-integration to $t \approx 669$ took many hours of CPU time, owing to the need for a fine spatial mesh in the boundary layers near the two cells at each time step. In contrast, our fast algorithm, implemented in *Fortran77* on a *Dell Precision* laptop with an *Intel Core I7* processor, completed in roughly one minute.

Next, we consider the same parameters as in Figs. 6(c) and 7(c) except that we now modify the kinetic parameter to $\alpha_1 = 0.4$ for the first cell centered at $\mathbf{x}_1 = (1, 0)$. For $\alpha_1 = 0.4$, an isolated cell with no boundary efflux would have limit cycle oscillations (see the blue star in Fig. 3(a)). Since $d_{21} = 0.2$, we further observe from Fig. 4 that the cell centered at \mathbf{x}_1 would have limit cycle oscillations even with boundary efflux when it is uncoupled from the bulk. As a result, we refer to this cell as the *signaling cell*. In the scatter plot shown in Fig. 11(a) we observe that the steady-state is always unstable in the $1/\sigma$ versus D parameter plane. In the blue-shaded region, the unique destabilizing mode is the one for which the amplitude of intracellular oscillations for the signaling cell centered at \mathbf{x}_1 is large, and where the second cell centered at \mathbf{x}_2 has very small oscillations, and so is effectively silent. In Fig. 11(a) there is only one HB boundary and it corresponds to a marginal mode where intracellular oscillations emerge in the otherwise silent cell centered at $\mathbf{x}_2 = (-1, 0)$ and where the signaling cell centered at \mathbf{x}_1 is effectively silent. However, by plotting the path of the two dominant eigenvalues in Fig. 11(b) and Fig. 11(c) along the horizontal and vertical slices shown in Fig. 11(a), respectively, we observe that the mode with the largest growth rate is always the one for which the cell centered at \mathbf{x}_2 has only very small amplitude oscillations in comparison to that for the signaling cell. By computing the eigenvector \mathbf{c} for the two modes at some points along the horizontal slice in Fig. 11(a), we use the criterion in (4.68b) to determine the relative magnitude of the intracellular oscillations in the two cells for the linearized problem. As shown in Table 4, the mode with the largest growth rate is the one for which the second

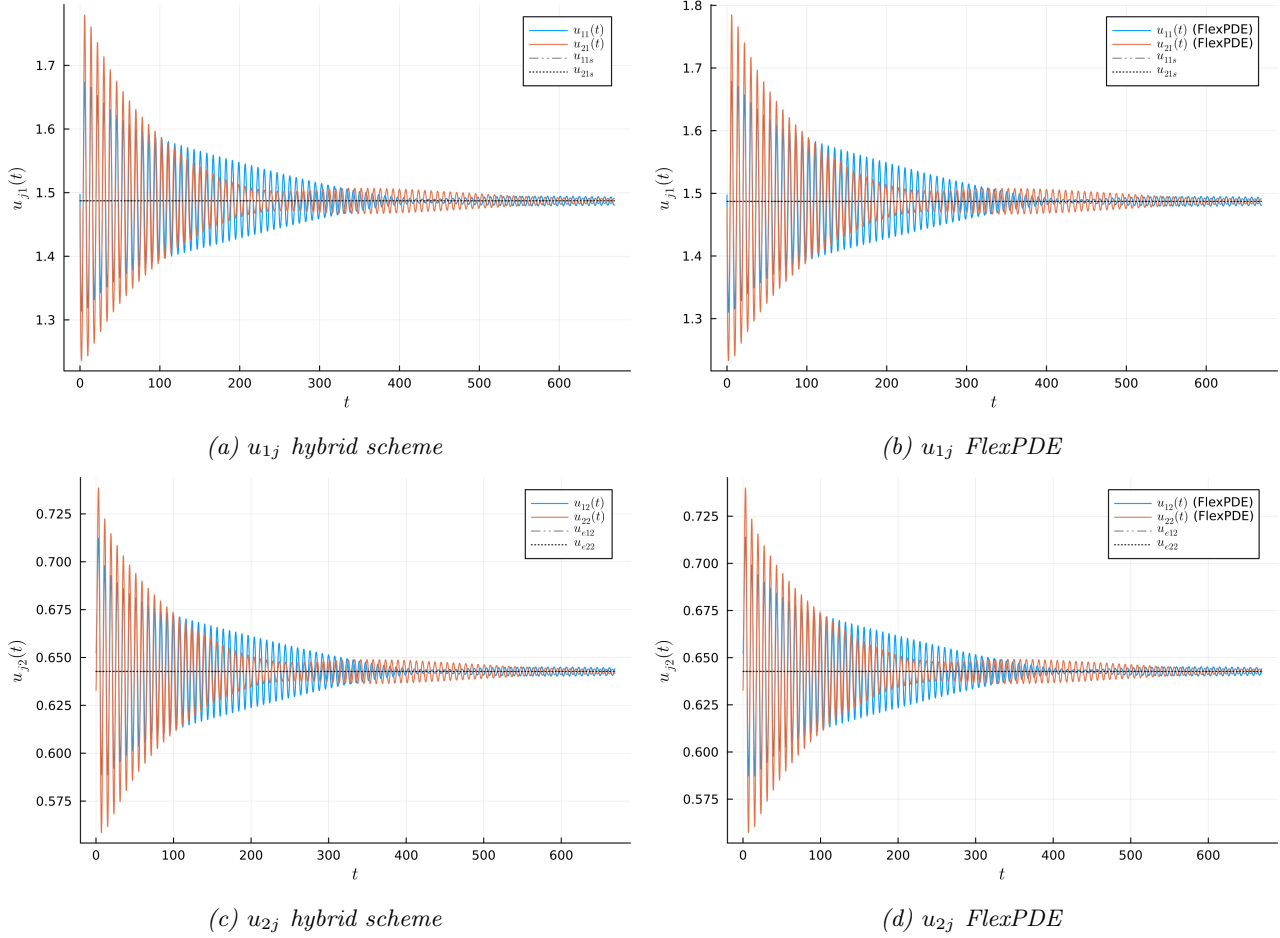


Figure 9: Comparison of the numerical solutions computed from the integro-differential system (3.36) using the algorithm in §5.4 with that computed from the cell-bulk model (1.5) using FlexPDE [18] with the artificial boundary condition given in (D.10) of Appendix D. Parameters: $D = 0.75$, $\sigma = 1/7$ with $d_{1j} = 0.4$, $d_{2j} = 0.2$ and $\alpha_j = 0.9$ corresponding to the star-labeled point in Fig. 7(a). The initial condition imposed was the steady-state with an anti-phase perturbation: $\mathbf{u}_1^{(0)} = (u_{11s}, u_{21s})^T + 0.01 \cdot (1, -1)^T$, and similarly for $\mathbf{u}_2^{(0)}$. The initial bulk solution for (1.5) was $U(\mathbf{x}, 0) = 0$. The steady-state is the black horizontal line.

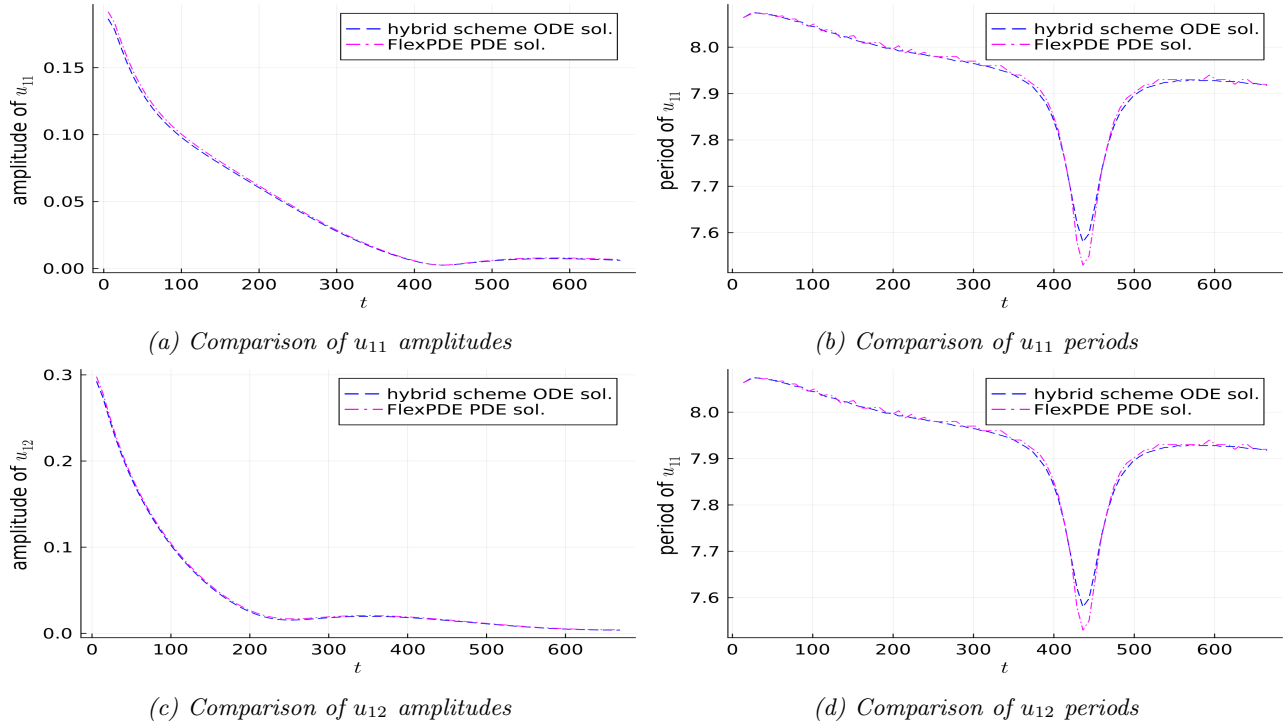


Figure 10: Comparison of the amplitude and period of the numerical solutions to u_{1j} for $j \in \{1, 2\}$ as computed from the integro-differential system (3.36) using the fast algorithm in §5.4 with that computed from the cell-bulk model (1.5) using FlexPDE [18]. The parameters are as in in Fig. 9.

cell is effectively quiet.

By using our algorithm in §5.4 with $\Delta t = 0.002$, and with random initial values near the steady-state of magnitude 0.01, in Fig. 12 we plot u_{2j} versus t on the time window $600 < t < 800$ at the three star-labeled points along the horizontal and vertical slices in Fig. 11(a). We conjecture that when both the in-phase and anti-phase modes are destabilizing for the linearization of the steady-state solutions, such as for $D = 2$, $\sigma = 1/2$ in Fig. 12(a) and for $D = 4$, $\sigma = 1/2$ in Fig. 12(b), the oscillations for the second cell centered at \mathbf{x}_2 are of wave-packet type, as is characteristic of mixed-mode oscillations.

D	$ \mathbf{c}_1 $	$ \mathbf{c}_2 $	$\Delta\theta_c(\text{rad})$	$ (K\mathbf{c})_1 $	$ (K\mathbf{c})_2 $	$\Delta\theta_k(\text{rad})$	$\text{Re}(\lambda)$	Quiet
2	1.0000	0.0078	2.71	0.9989	0.0467	0.78	0.215	cell 2
2	0.1018	0.9948	2.31	0.0468	0.9989	2.25	0.017	cell 1
4	0.9999	0.0127	1.26	0.9973	0.0736	0.59	0.252	cell 2
4	0.1422	0.9898	3.77	0.0731	0.9973	2.46	0.0135	cell 1
6	0.9998	0.0182	0.93	0.9965	0.0838	0.49	0.269	cell 2
6	0.1556	0.9878	3.69	0.0834	0.9965	2.56	0.0010	cell 1
8	0.9998	0.0210	0.80	0.9962	0.0872	0.45	0.278	cell 2
8	0.1588	0.9873	3.64	0.0804	0.9963	2.60	-0.013	cell 1

Table 4: Moduli of the components c_j of the eigenvector $\mathbf{c} = (c_1, c_2)^T$, normalized by $\mathbf{c}^H \mathbf{c} = 1$, and of the normalized components of $K\mathbf{c}$ at some specific points along the horizontal path through the scatter plot in Fig. 11(a) for the two roots of $\det \mathcal{M}(\lambda) = 0$ with the largest real part. $\Delta\theta_c$ and $\Delta\theta_k$ denote the phase shift for the eigenvector \mathbf{c} and for $K\mathbf{c}$, respectively, between the cells. The dominant mode of instability always corresponds to the cell at \mathbf{x}_2 having very small amplitude oscillations as compared to that for the signaling cell. Parameters are as in Fig. 11.

For $D = 3$ and $\sigma = 1/2$ in the scatter plot of Fig. 11(a), in Fig. 13 we show that our fast algorithm with $\Delta t = 0.002$ is able to reproduce with high accuracy the delicate wave-packet type oscillations for cell 2 over long time scales that occurs in the FlexPDE numerical solution of (1.5). The FlexPDE results

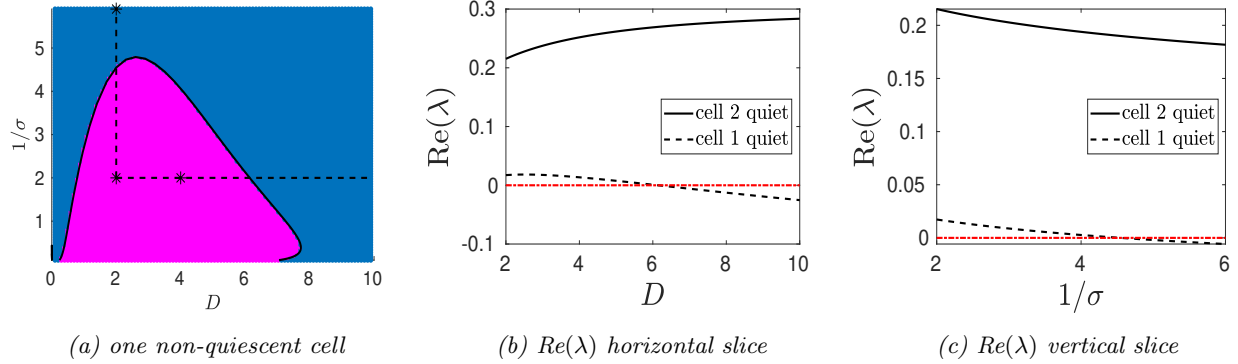


Figure 11: Left: Scatter plot of the number Z of destabilizing eigenvalues, with $Z = 2$ (blue) and $Z = 4$ (magenta), for the linearization of the steady-state in the $1/\sigma$ versus D plane for two non-identical cells with different kinetics parameter $\alpha_1 = 0.4$ and $\alpha_2 = 0.9$. The remaining parameters are $d_{1j} = 1.5$ and $d_{2j} = 0.2$ for $j \in \{1, 2\}$. Only the cell with $\alpha_1 = 0.4$ (signaling cell) would have limit cycle oscillations with boundary efflux when it is uncoupled to the bulk. The sole HB boundary is superimposed. The steady-state is now always unstable. Middle: $\text{Re}(\lambda)$ versus D along the horizontal slice. Right: $\text{Re}(\lambda)$ versus $1/\sigma$ along the vertical slice. The dominant mode of instability is for intracellular oscillations to be concentrated to the first cell, while the second cell is essentially quiescent.

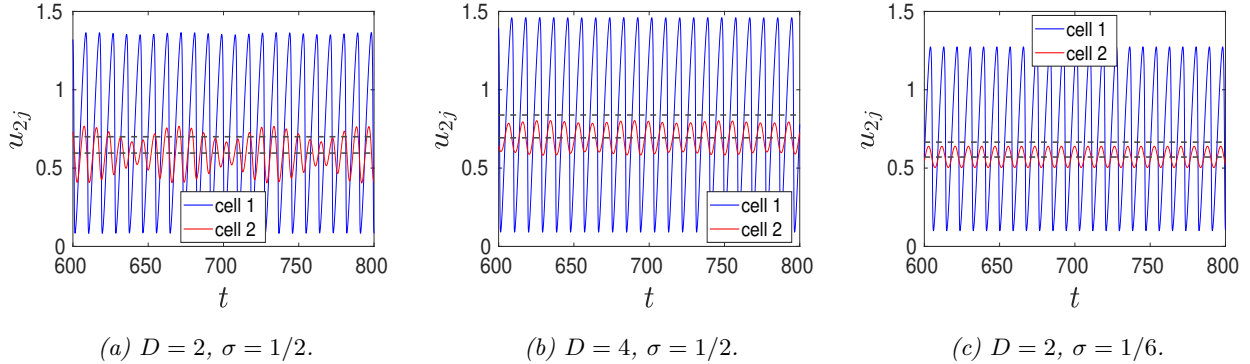


Figure 12: Intracellular dynamics $u_{2j}(t)$ between $600 < t < 800$ at the three star-labeled points along the vertical and horizontal slices in Fig. 11(a). Left: $D = 2$, $\sigma = 1/2$: wave-packet solution for second cell. Middle: $D = 4$, $\sigma = 1/2$: wave-packet solution transitions to regular oscillations. Right: $D = 2$, $\sigma = 1/6$: regular oscillations occur for the second cell but with smaller amplitude. The dashed horizontal lines are the unstable steady-state values for u_{2j} . Parameters: $\alpha_1 = 0.4$, $\alpha_2 = 0.9$, with $d_{1j} = 1.5$ and $d_{2j} = 0.2$ for $j \in \{1, 2\}$.

required hours of CPU time, whereas the hybrid algorithm completed in less than a minute on a laptop.

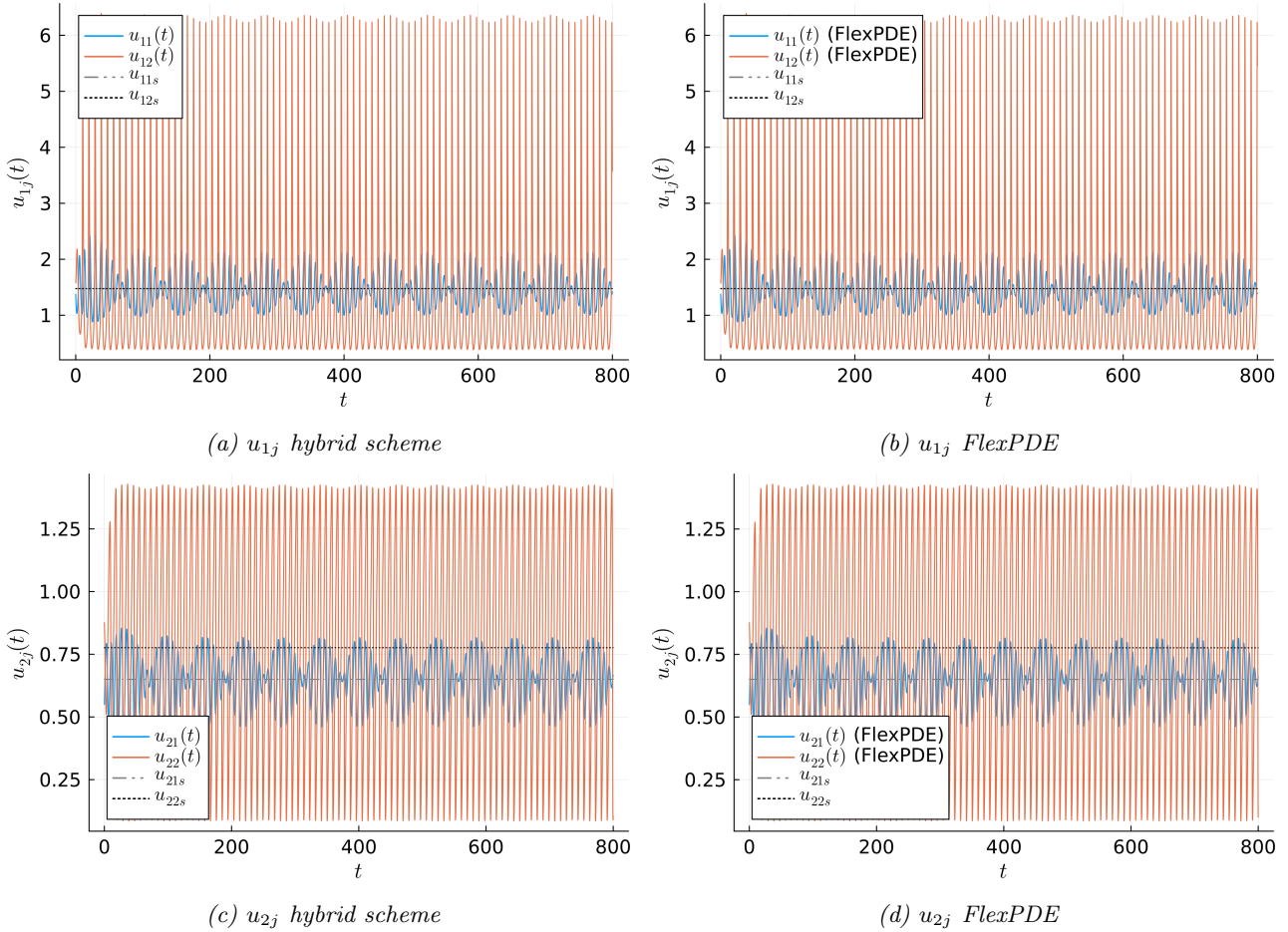


Figure 13: Same caption as in Fig. 9 except that parameters are now $D = 3$, $\sigma = 1/2$. $\alpha_1 = 0.4$, $\alpha_2 = 0.9$ and $d_{1j} = 1.5$ and $d_{2j} = 0.2$ for $j \in \{1, 2\}$ corresponding to the scatter plot in Fig. 11(a). The initial condition imposed was the steady-state with an anti-phase perturbation: $\mathbf{u}_1^{(0)} = (u_{11s}, u_{21s})^T + 0.1 \cdot (1, -1)^T$, and similarly for $\mathbf{u}_2^{(0)}$. The initial bulk solution for (1.5) was $U(\mathbf{x}, 0) = 0$. The hybrid algorithm accurately reproduces the wave-packet oscillations of cell 2 over long time intervals. The unstable steady-states for cell 1 and cell 2 are the upper and lower black horizontal lines, respectively.

Next, we consider the effect on intracellular oscillations of increasing the efflux permeability for the prior signaling cell centered at \mathbf{x}_1 to $d_{21} = 0.5$. From Fig. 4 we observe that limit cycle oscillations no longer occur for this cell when it is uncoupled from the bulk, and so we refer to this cell as being *deactivated*. Moreover, we decrease the influx parameter for this cell to $d_{11} = 0.4$, so that there is less influx from the bulk medium as compared to the cell at \mathbf{x}_2 . In Fig. 14(a) we show the resulting scatter plot in the $1/\sigma$ versus D plane. We now observe that there is a parameter range (i.e. the white region) where the steady-state is linearly stable. Along the dotted parameter path shown in Fig. 14(a), in Figs. 14(b)-14(c) we plot $\text{Re}(\lambda)$ on the left vertical axis for each of the two dominant modes. On the right vertical axes we plot our criterion in (4.68b) that predicts which cell will have larger amplitude oscillations near the steady-state. In contrast to the behavior in Fig. 11 for the case where the permeabilities were identical for the two cells, we observe from the right vertical axes in Figs. 14(b)-14(c) that, as D is increased with $\sigma = 2$, the dominant mode of instability is the one for which the deactivated cell with $\alpha_1 = 0.4$ now has much smaller intracellular oscillations than the cell with $\alpha_2 = 0.9$.

With the algorithm in §5.4 using $\Delta t = 0.005$, and with uniformly random initial conditions near the steady-state values, in Fig. 15 we show u_{2j} versus t at the three star-labeled points with increasing D along the parameter path in Fig. 14(a). As D increases, the amplitude of the intracellular oscillations in

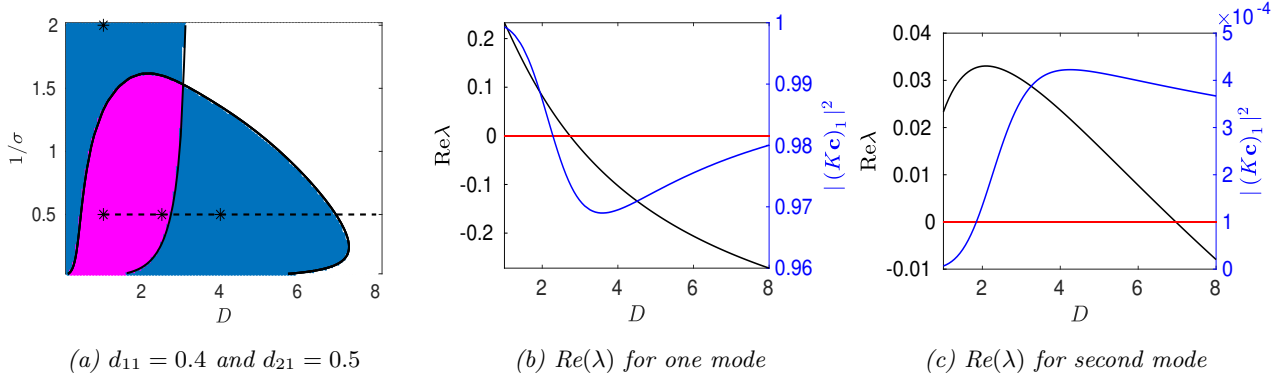


Figure 14: Left: Scatter plot after decreasing the influx parameter to $d_{11} = 0.4$ and increasing the efflux parameter to $d_{21} = 0.5$ for the cell centered at \mathbf{x}_1 with $\alpha_1 = 0.4$. Remaining parameter are as in Fig. 11. The number \mathcal{Z} of destabilizing eigenvalues for the linearization of the steady-state is: $\mathcal{Z} = 0$ (white), $\mathcal{Z} = 2$ (blue) and $\mathcal{Z} = 4$ (magenta). Middle: Left vertical axis is $\text{Re}(\lambda)$ along the dotted path in the left panel for the mode where oscillations have larger amplitude in cell 1. The right vertical axis is $|(K\mathbf{c})_1|^2$ (see (4.68b)) that measures the relative amplitude of the oscillations near the steady-state for cell 1. Here we normalized $\sum_{j=1}^2 |(K\mathbf{c})_j|^2 = 1$. Right: Same as middle plot but now for the other dominant mode where oscillations are predicted to be much larger in cell 2 since $|(K\mathbf{c})_1|^2 = \mathcal{O}(10^{-4}) \ll 1$. The red horizontal lines denote the stability threshold $\text{Re}(\lambda) = 0$.

the deactivated cell 1 decreases as predicted by Figs. 14(b)-14(c). However, when $D = 1$ and $\sigma = 1/2$, the deactivated cell will have much larger amplitude oscillations than for the other cell centered at \mathbf{x}_2 .

6.4 A ring configuration of cells

Next, we consider the four-cell configuration shown in Fig. 5(b) where there are two pairs of cells with common kinetic parameters and permeabilities. For this case, and where a , b , h , and d can be identified from (4.64b), the GCEP matrix \mathcal{M} in (4.64b) has the form

$$\mathcal{M} = \begin{pmatrix} a & h & d & h \\ h & b & h & d \\ d & h & a & h \\ h & d & h & b \end{pmatrix}. \quad (6.116)$$

Omitting the details of the derivation, the matrix spectrum of \mathcal{M} is readily obtained as follows:

Lemma 6.1. *For the matrix in (6.116), we have*

$$\det \mathcal{M} = (a - d)(b - d) [(a + d)(b + d) - 4h^2]. \quad (6.117)$$

The matrix spectrum for $\mathcal{M}\mathbf{c} = \chi\mathbf{c}$ is

$$\begin{aligned} \mathbf{c}_1 &= (1, 0, -1, 0)^T, & \chi_1 &= a - d; & \mathbf{c}_2 &= (0, 1, 0, -1)^T, & \chi_2 &= b - d, \\ \mathbf{c}_\pm &= (1, f_\pm, 1, f_\pm)^T, & \chi_\pm &= (a + d) + 2hf_\pm; & f_\pm &\equiv \frac{(b - a)}{4h} \pm \sqrt{\frac{(b - a)^2}{(4h)^2} + 1}. \end{aligned} \quad (6.118a)$$

To determine the eigenvalues λ of the linearization of the steady-state, which satisfy $\det \mathcal{M}(\lambda) = 0$, we need only find the union of the roots of the scalar root-finding problems $a = d$, $b = d$ and $4h^2 = (a + d)(b + d)$. The HB boundaries in the $1/\sigma$ versus D plane are obtained by setting $\lambda = i\lambda_I$. For identical cells where $a = b$, the modes \mathbf{c}_1 and \mathbf{c}_2 are degenerate since $a = b$. For identical cells, where $f_\pm = \pm 1$, the in-phase and anti-phase modes are $\mathbf{c}_+ = (1, 1, 1, 1)^T$ and $\mathbf{c}_- = (1, -1, 1, -1)^T$, respectively.

For identical cells with $d_{1j} = 0.4$, $d_{2j} = 0.2$ and $\alpha_j = 0.9$ for $j \in \{1, \dots, 4\}$, and with a ring radius $r_c = 1$, the scatter plot is shown in Fig. 16(a). In Fig. 16(b) we plot the real parts of the three dominant eigenvalues of $\det \mathcal{M}(\lambda) = 0$ along the horizontal path shown in Fig. 16(a). In the blue-shaded region,

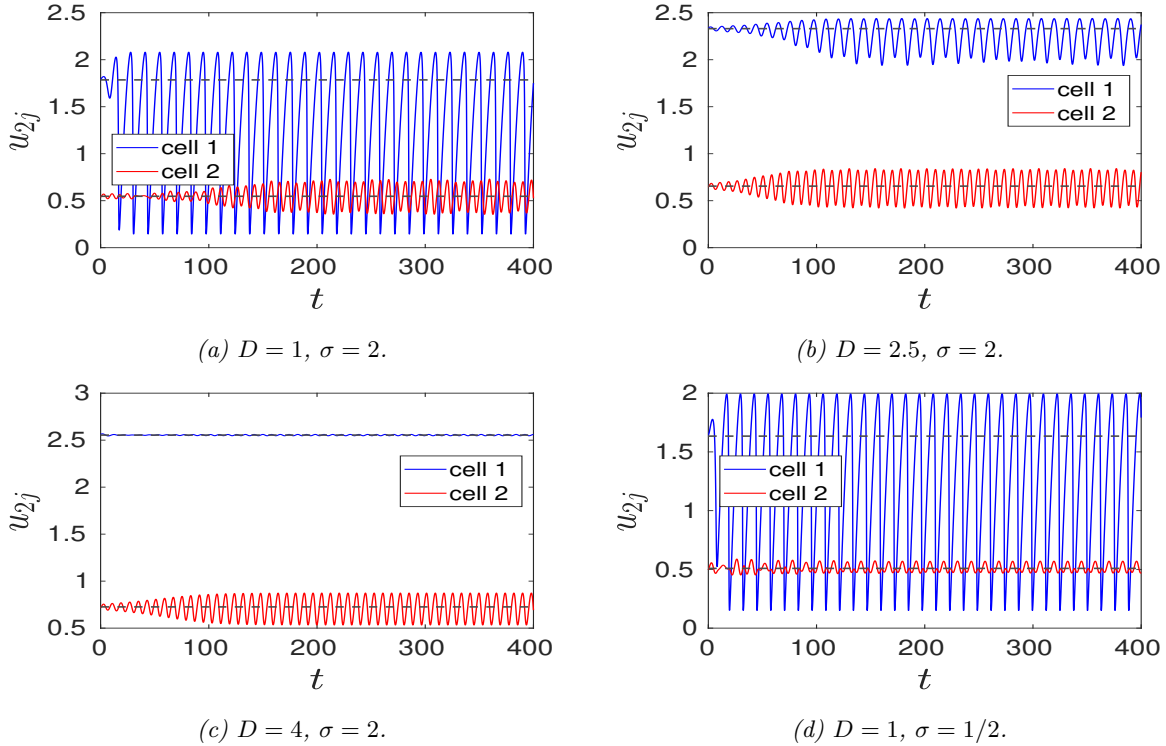


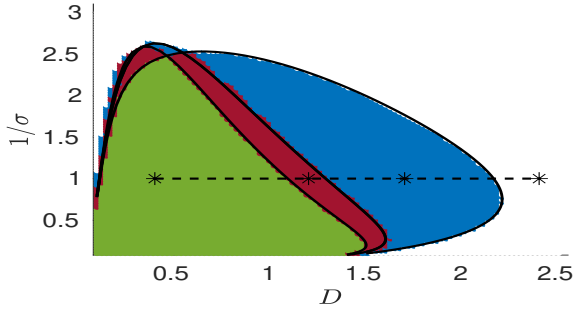
Figure 15: Top left, top right, bottom left: intracellular dynamics $u_{2j}(t)$ at the three star-labeled points along the path in Fig. 14(a). As D increases, the amplitude of oscillations in the deactivated cell 1 decreases. Bottom right: $u_{2j}(t)$ when $D = 1$ and $\sigma = 1/2$ (see Fig. 14(a)), where large oscillations in the deactivated cell occur. Dashed horizontal lines are the steady-states. Parameters: $\alpha_1 = 0.4$, $\alpha_2 = 0.9$, $d_{11} = 0.4$, $d_{21} = 0.5$, $d_{12} = 1.5$, $d_{22} = 0.2$.

only the in-phase mode is destabilizing, while in the green-shaded region all modes are destabilizing. Moreover, for $D = 0.4$, all the destabilizing modes have comparable growth rates. For this parameter set, Fig. 4 shows that no intracellular oscillations would occur when there is no coupling to the bulk.

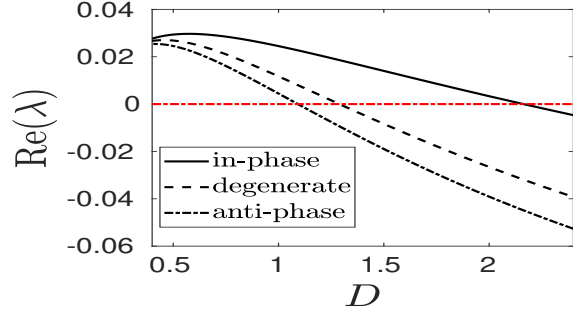
In Fig. 17 we plot u_{2j} versus t at the star-labeled points shown along the parameter path in Fig. 16(a) as computed using the algorithm of §5.4 with $\Delta t = 0.005$. The choice of initial conditions imposed near the steady-state values are indicated in the figure subcaptions. As predicted by the large growth rate of the in-phase mode in Fig. 16(b), the intracellular oscillations become synchronous as time increases for $D = 2.4$, $D = 1.7$ and $D = 1.2$. This is confirmed by the top row in Fig. 17. Furthermore, for $D = 0.4$, where all the destabilizing modes have comparable growth rates, the bottom row of Fig. 17 shows, as predicted, that the long-term dynamics depends on the precise form of the initial conditions imposed.

Next, we consider two pairs of identical cells with $\alpha_2 = \alpha_4 = 0.5$, $\alpha_1 = \alpha_3 = 0.9$, and with the same permeabilities $d_{1j} = 0.4$ and $d_{2j} = 0.2$ for $j \in \{1, \dots, 4\}$ as in Fig. 16(a). For this parameter set, from Fig. 4 we observe that cells 2 and 4 would exhibit limit-cycle oscillations when uncoupled from the bulk. We refer to these two cells as signaling cells. In Fig. 18(a) we show the scatter plot, while in Fig. 18(b) we plot the real parts of the four dominant eigenvalues of $\det \mathcal{M}(\lambda) = 0$ along the parameter path shown in Fig. 18(a). In the magenta-shaded region the dominant instability is where the signaling cells are activated. For $D = 0.4$, there are four destabilizing modes. In Fig. 19 we plot u_{2j} versus t at the two star-labeled points along the parameter path in Fig. 18(a) as computed using the algorithm of §5.4 with $\Delta t = 0.005$. For $D = 1.75$, the non-signaling cells 1 and 3 have in-phase small amplitude oscillations. However, for $D = 0.5$, as a result of the multiple destabilizing modes shown in Fig. 18(b), the type of oscillation that occurs in the non-signaling cells depends on the choice of initial condition near the steady-state that is imposed (see Fig. 19(b)–19(c)).

Finally, we explore the effect of increasing the efflux to $d_{22} = d_{24} = 0.5$ for the signaling cells with $\alpha_2 = \alpha_4 = 0.5$, while also increasing the influx to $d_{11} = d_{13} = 2.0$ for the non-signaling cells where

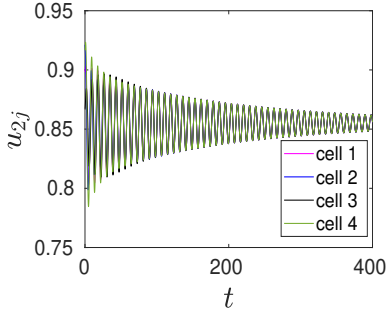


(a) Four identical cells on a ring

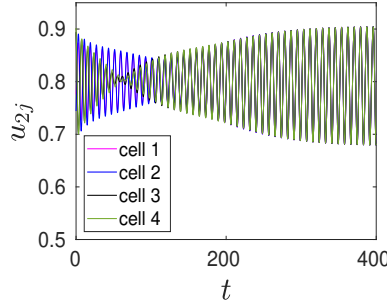


(b) $\text{Re}(\lambda)$ on horizontal slice

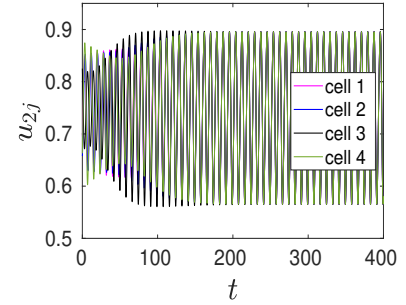
Figure 16: Left: Scatter plot of the number Z of destabilizing eigenvalues, with $Z = 0$ (white), $Z = 2$ (blue), $Z = 6$ (rust) and $Z = 8$ (green) for the linearization of the steady-state for four identical cells with a ring radius $r_c = 1$ (see Fig. 5(b)), with $d_{1j} = 0.4$, $d_{2j} = 0.2$ and $\alpha_j = 0.9$ for $j \in \{1, \dots, 4\}$. The HB boundaries (solid black curves) are superimposed. Right: Real part of the dominant eigenvalues of $\det \mathcal{M}(\lambda) = 0$ along the horizontal path with $\sigma = 1$ in the left panel. Owing to the circulant matrix structure of $\mathcal{M}(\lambda)$ there is mode degeneracy. In the blue region only the in-phase mode is destabilizing. For $D = 0.4$, the three destabilizing modes have similar growth rates.



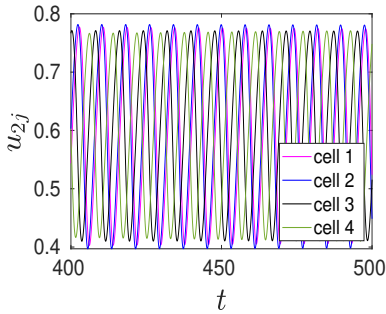
(a) $D = 2.4$ (random)



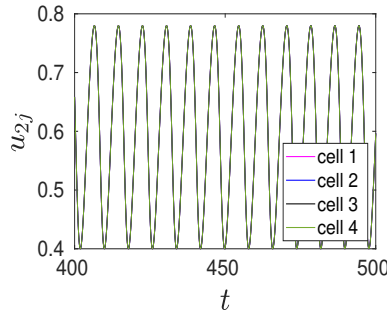
(b) $D = 1.7$ (random)



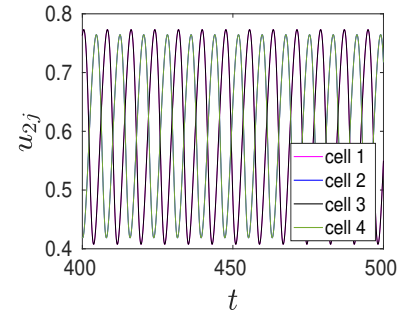
(c) $D = 1.2$ (random)



(d) $D = 0.4$ (random)



(e) $D = 0.4$ (in-phase)



(f) $D = 0.4$ (anti-phase)

Figure 17: Intracellular dynamics $u_{2j}(t)$ at the star-labeled points along the horizontal slice with $\sigma = 1$ in Fig. 16(a) computed using the algorithm in §5.4 with $\Delta t = 0.005$. The type of initial condition (IC) is indicated in the captions: Random: perturbing the steady-state values for u_{1j} and u_{2j} by $0.1 \cdot U$, where U is uniformly distributed on $[-1, 1]$. In-phase: perturbing steady-states by $0.1 \cdot (1, 1, 1, 1)^T$. Anti-phase: perturbing steady-states by $0.1 \cdot (1, -1, 1, -1)^T$. Top left: For $D = 2.4$, random IC lead to synchronous oscillations that slowly decay to the steady-state limit. Top middle and top right: For $D = 1.7$ and $D = 1.2$, random IC lead to persistent in-phase oscillations. Bottom row: For $D = 0.4$, the choice of IC imposed leads to distinctly different long-time dynamics as suggested by Fig. 16(b). Parameters: Identical cells with $\alpha_j = 0.9$, $d_{1j} = 0.4$ and $d_{2j} = 0.2$ for $j \in \{1, \dots, 4\}$.

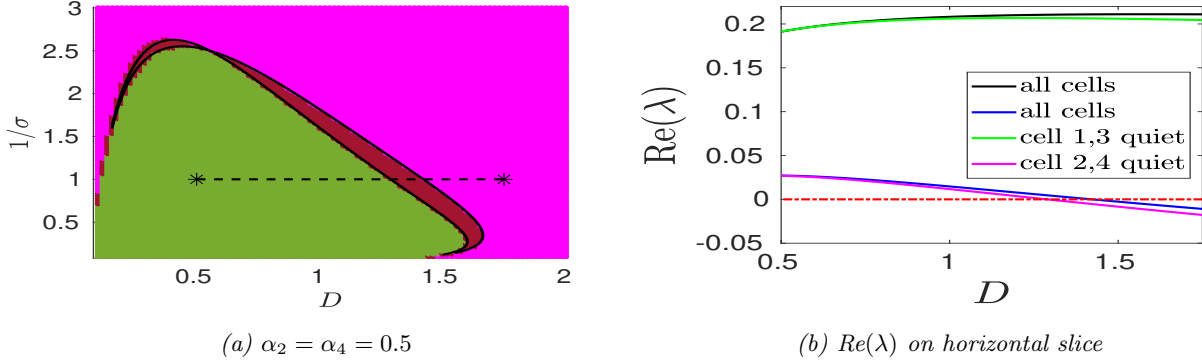


Figure 18: Left: Scatter plot of the number Z of destabilizing eigenvalues, with $Z = 4$ (magenta), $Z = 6$ (rust) and $Z = 8$ (green) for the linearization of the steady-state for two pairs of identical cells with $r_c = 1$ where $\alpha_2 = \alpha_4 = 0.5$ and $\alpha_1 = \alpha_3 = 0.9$. The HB boundaries are superimposed. Same permeabilities d_{1j} and d_{2j} as in Fig. 16(a). Cells 2 and 4 admit limit cycle oscillations when uncoupled from the bulk. Right: Real part of the four dominant eigenvalues of $\det \mathcal{M}(\lambda) = 0$ on the horizontal path with $\sigma = 1$ in the left panel. The labels for the eigenmodes from (6.118a) are $\mathbf{c}_1 = (1, 0, -1, 0)^T$ (cells 2, 4 silent), $\mathbf{c}_2 = (0, 1, 0, -1)^T$ (cells 1, 3 silent), and $\mathbf{c}_{\pm} = (1, f_{\pm}, 1, f_{\pm})^T$ (all cells active). There are two destabilizing modes when $D = 1.75$ and four when $D = 0.5$.

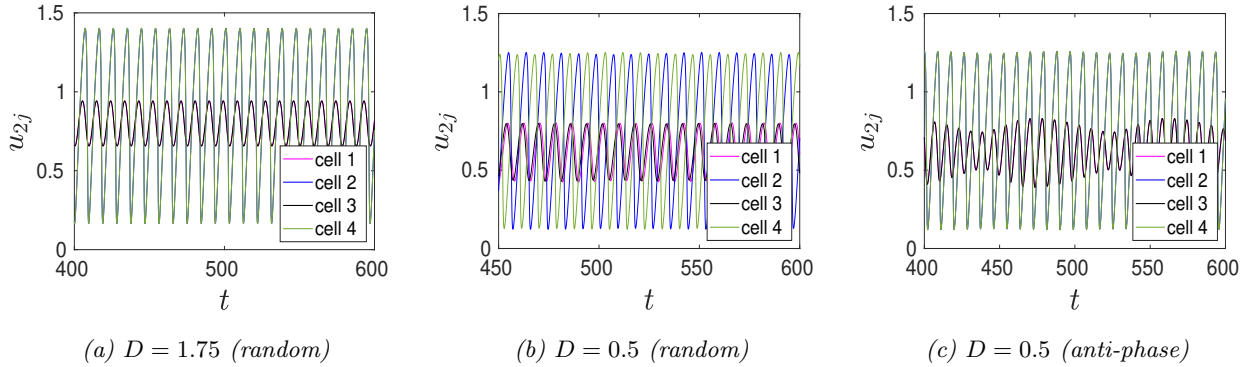


Figure 19: Intracellular dynamics $u_{2j}(t)$ at the two star-labeled points along the horizontal path with $\sigma = 1$ in Fig. 18(a) computed using the algorithm in §5.4 with $\Delta t = 0.005$. The choice of initial condition (IC) is indicated (see caption of Fig. 19 for details). Left: For $D = 1.75$ cells 2 and 4 trigger small amplitude oscillations in cells 1 and 3. Middle: for $D = 0.5$ with a uniformly random IC, there is a phase shift in the oscillations of the signaling cells. Incoherent oscillations occur in the other cells. Right: For $D = 0.5$ with anti-phase IC, the signaling cells oscillate in-phase. Cells 1 and 3 exhibit mixed-mode type oscillations.

$\alpha_1 = \alpha_3 = 0.9$. For this modified parameter set, Fig. 4 shows that cells 2 and 4 no longer exhibit limit cycle oscillations when uncoupled from the bulk. As such, these two cells have now been deactivated. In Fig. 20(a) we show how the scatter plot of Fig. 18(a) is modified, while in Fig. 20(b) we plot the real parts of the four dominant eigenvalues of $\det \mathcal{M}(\lambda) = 0$. In contrast to Fig. 18(b), we now observe that the dominant instability at the right-end of the horizontal path where $D = 2$ and $\sigma = 4$ in Fig. 20(a) is where the deactivated cells 2 and 4 are now effectively quiet. In Fig. 21 we plot u_{2j} versus t at the four star-labeled points in Fig. 20(a), as computed using the algorithm of §5.4 with $\Delta t = 0.005$. For $D = 2$ and $\sigma = 4$, in Fig. 21(a) we observe that the non-signaling cells, cells 1 and 3 (which would not oscillate without cell-bulk coupling), have much larger amplitude oscillations than do the deactivated signaling cells, as is consistent with the prediction from Fig. 18(b). Moreover, when both D and σ are smaller, i.e. $D = \sigma = 1$, Fig. 21(c) shows that the non-signaling cells have a much small amplitude oscillation in comparison with the deactivated signaling cells. To interpret this behavior, for smaller bulk diffusivity and with a lower degradation rate, the spatial gradient in (4.68a) that occurs in the vicinity of the deactivated cells can be large. Owing to the influx permeability, this large signaling gradient can effectively re-activate these cells when D is small. We suggest that this behavior is related to the qualitative mechanism of *diffusion-sensing* (cf. [30]). By increasing D to $D = 1.65$, Fig. 21(d) shows that both pairs of cells exhibit only small amplitude oscillations. Overall, the distinct time-dependent behaviors observed in Fig. 21 illustrate how the components of the eigenvector \mathbf{c} of the GCEP matrix encodes key predictive information on which cells will have larger oscillations near an unstable steady-state.

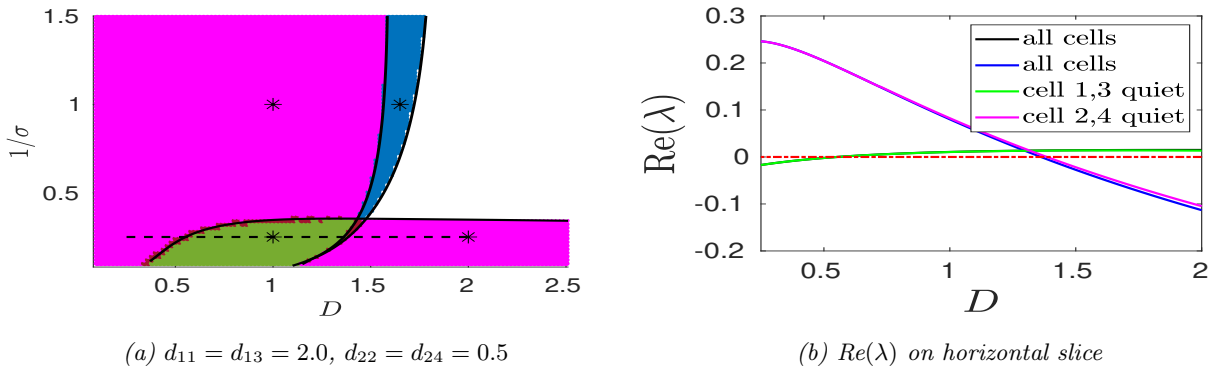


Figure 20: Left: Scatter plot with $r_c = 1$, $\alpha_2 = \alpha_4 = 0.5$ and $\alpha_1 = \alpha_3 = 0.9$, but now $d_{11} = d_{13} = 2.0$ and $d_{22} = d_{24} = 0.5$. Remaining parameters are $d_{12} = d_{14} = 0.4$ and $d_{21} = d_{23} = 0.2$. The deactivated signaling cells 2 and 4 now have an increased efflux and no longer admit limit cycle oscillations when uncoupled from the bulk. The influx permeability for the other two cells is much larger than in Fig. 18(a). Right: Real part of the four dominant eigenvalues of $\det \mathcal{M}(\lambda) = 0$ on the horizontal path with $\sigma = 0.25$ in the left panel.

6.5 A ring configuration with a center cell

Next, we consider the centered-hexagonal cell configuration shown in Fig. 5(c). We label the ring cells in a counterclockwise orientation by $\mathbf{x}_j = r_c (\cos(\pi(j-1)/3), \sin(\pi(j-1)/3))^T$ for $j \in \{1, \dots, 6\}$, while the center-cell at the origin is $\mathbf{x}_7 = \mathbf{0}$. The ring cells are assumed to be identical with $d_{1j} = d_{1r}$, $d_{2j} = d_{2r}$ and $\alpha_j = \alpha_r$ for $j \in \{1, \dots, 6\}$. The center cell can have different permeabilities d_{17} and d_{27} and a distinct kinetic parameter α_7 .

For this cell configuration, the GCEP matrix \mathcal{M} in (4.64b) can be partitioned as

$$\mathcal{M}(\lambda) = \left(\begin{array}{c|c} \mathcal{M}_6 & \begin{matrix} a \\ \vdots \\ a \end{matrix} \\ \hline a & \dots & a & b \end{array} \right), \quad (6.119a)$$

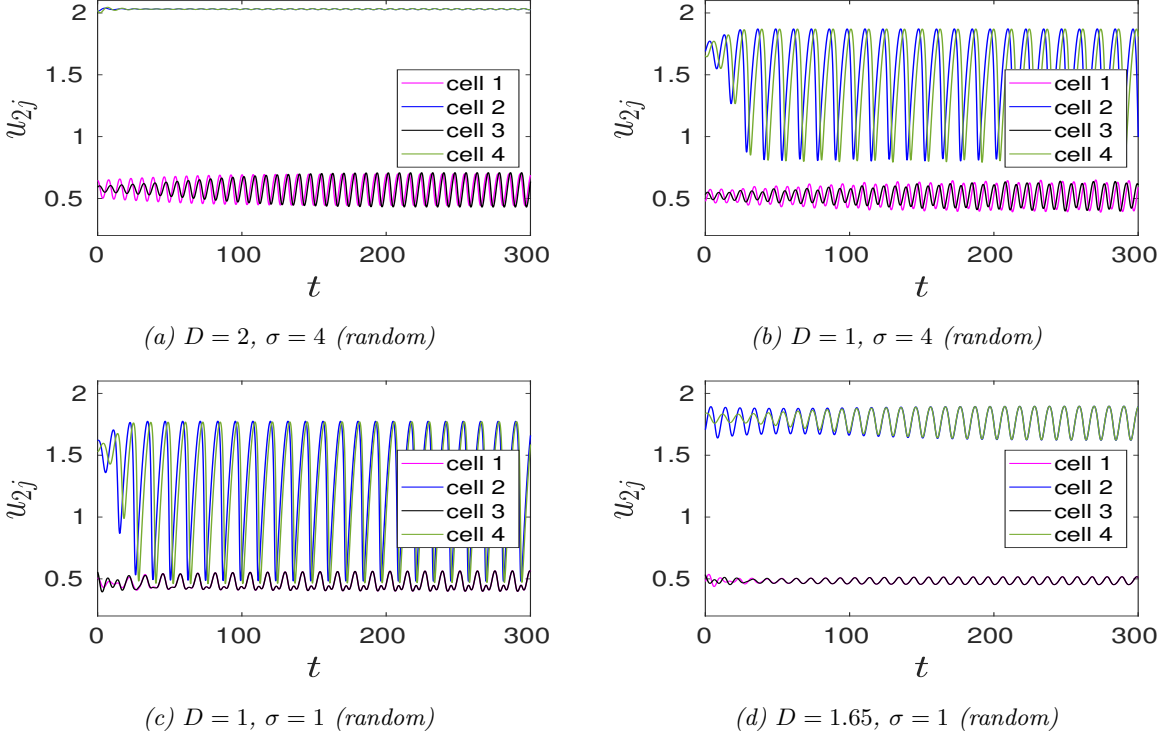


Figure 21: Intracellular dynamics $u_{2j}(t)$ at the four star-labeled points in Fig. 20(a), as computed using the algorithm in §5.4 with $\Delta t = 0.005$. Uniformly random initial perturbations of magnitude 0.1 were used. Top left: Synchronized oscillations occur in cells 1 and 3, while the deactivated cells 2 and 4 are quiet. Top right: The deactivated cells oscillate out of phase, and mixed-mode oscillations occur in the other cells. Bottom left: Large amplitude in-phase oscillations occur in the deactivated cells, with very small in-phase oscillations in the other cells. Bottom right: both pairs of cells have only small amplitude in-phase oscillations. Parameters as in Fig. 20.

where $\mathcal{M}_6 \in \mathbb{C}^{6,6}$ is both circulant and symmetric. Here a and b are defined by

$$a \equiv \nu K_0 \left(\sqrt{\frac{\sigma + \lambda}{D}} |\mathbf{x}_1 - \mathbf{x}_7| \right), \quad b \equiv 1 + \nu \left(\log \left(2 \sqrt{\frac{D}{\sigma + \lambda}} \right) - \gamma_e \right) + \frac{\nu D}{d_{17}} (1 + 2\pi d_{27} K_7), \quad (6.119b)$$

with $\nu = -1/\log \varepsilon$ and K_7 as given in (6.112). In (6.119a), \mathcal{M}_6 is a cyclic permutation of its first row, labeled by (m_1, \dots, m_6) , in which $m_2 = m_6$ and $m_3 = m_5$ since \mathcal{M}_6 is symmetric. The matrix spectrum of \mathcal{M}_6 consists of an in-phase eigenvector $\mathbf{e}_6 \equiv (1, \dots, 1)^T \in \mathbb{R}^6$ and five anti-phase eigenvectors, two of which are degenerate, which are all orthogonal to \mathbf{e}_6 . For \mathcal{M} , these anti-phase modes are lifted to \mathbb{R}^7 by requiring that the center cell is silent. The in-phase mode for \mathcal{M}_6 will lead to two eigenmodes in \mathbb{R}^7 for \mathcal{M} where the center cell is active. The matrix spectrum of \mathcal{M} is characterized as follows:

Lemma 6.2. *The matrix eigenvalues for $\mathcal{M}\mathbf{c} = \chi\mathbf{c}$, with \mathcal{M} as in (6.119a), are*

$$\chi_j = \sum_{k=1}^6 \cos \left(\frac{\pi j(k-1)}{3} \right) m_k, \quad j \in \{1, \dots, 5\}, \quad (6.120a)$$

$$\chi_{\pm} = \omega_6 + af_{\pm}, \quad f_{\pm} \equiv \frac{(b - \omega_6)}{2a} \pm \sqrt{\frac{(b - \omega_6)^2}{(2a)^2} + 6},$$

where $\det \mathcal{M} = (\chi + \chi_-) \left(\prod_{j=1}^5 \chi_j \right) = (b\omega_6 - 6a^2) \left(\prod_{j=1}^5 \chi_j \right)$. Here ω_6 is defined by $\mathcal{M}_6 \mathbf{e}_6 = \omega_6 \mathbf{e}_6$ with $\mathbf{e}_6 \equiv (1, \dots, 1)^T \in \mathbb{R}^6$, while (m_1, \dots, m_6) is the first row of \mathcal{M}_6 . The corresponding eigenvectors are

$$\mathbf{c}_j = \left(1, \cos \left(\frac{\pi j}{3} \right), \dots, \cos \left(\frac{5\pi j}{3} \right), 0 \right)^T, \quad j \in \{1, 2\}; \quad \mathbf{c}_3 = (1, -1, 1, -1, 1, -1, 0)^T,$$

$$\mathbf{c}_{6-j} = \left(0, \sin \left(\frac{\pi j}{3} \right), \dots, \sin \left(\frac{5\pi j}{3} \right), 0 \right)^T, \quad j \in \{1, 2\}; \quad \mathbf{c}_{\pm} = (1, \dots, 1, f_{\pm})^T, \quad (6.120b)$$

where \mathbf{c}_3 is referred to as the sign-alternating anti-phase mode. Since $\chi_j = \chi_{6-j}$ for $j \in \{1, 2\}$, two pairs of anti-phase modes for which the center cell is silent are degenerate. The roots λ to $\det \mathcal{M}(\lambda) = 0$ are obtained from the union of the five scalar root-finding problems $\chi_1 = 0$, $\chi_2 = 0$, $\chi_3 = 0$ and $\chi_{\pm} = 0$. Setting $\chi_{\pm} = 0$, yields the parameter constraint $6a^2 = b\omega_6$ and $f_{\pm} = \mp \sqrt{6\omega_6/b}$.

Proof. The proof of this result for χ_j and \mathbf{c}_j for $j \in \{1, \dots, 5\}$ is immediate since \mathcal{M}_6 is a circulant matrix and $\mathbf{e}^T \mathbf{c}_j = 0$ for $j \in \{1, \dots, 5\}$, where $\mathbf{e} = (\mathbf{e}_6, 1)^T \in \mathbb{R}^7$. For the remaining two eigenmodes, we let $\mathbf{c} = (\mathbf{e}_6, f)^T$ and calculate using $\mathcal{M}_6 \mathbf{e}_6 = \omega_6 \mathbf{e}_6$ that

$$\mathcal{M}\mathbf{c} = \begin{pmatrix} \mathcal{M}_6 \mathbf{e}_6 + af \mathbf{e}_6 \\ 6a + bf \end{pmatrix} = \begin{pmatrix} (\omega_6 + af) \mathbf{e}_6 \\ 6a + bf \end{pmatrix} = \chi \begin{pmatrix} \mathbf{e}_6 \\ f \end{pmatrix}. \quad (6.121)$$

This yields that $\omega_6 + af = \chi$ and $6a + bf = \chi f$, which gives a quadratic equation for f . The solution yields (6.120a) and (6.120b) for χ_{\pm} and f_{\pm} . Setting $\chi = 0$ in (6.121) we readily obtain the constraint $6a^2 = b\omega_6$. \square

Fixing $d_{1r} = 0.8$, $d_{2r} = 0.9$ and $\alpha_r = 0.9$ for each of the six ring cells, and with influx permeability $d_{17} = 0.4$ and kinetic parameter $\alpha_7 = 0.5$ for the center cell, in Fig. 22(a) and Fig. 22(b) we show the scatter plots when the efflux permeability for the center cell is either $d_{27} = 0.2$ or $d_{27} = 0.5$, respectively. When $d_{27} = 0.2$ the center cell is a signaling cell (see Fig. 4) and would have limit cycle oscillations when uncoupled from the bulk. However, when $d_{27} = 0.5$ this signaling cell is deactivated. For comparison, in Fig. 22(c) we show the scatter plot for seven identical cells with parameter values $d_{1j} = 0.4$, $d_{2j} = 0.2$ and $\alpha_j = 0.9$ for $j \in \{1, \dots, 7\}$. These cells would all be in a quiescent state without any cell-bulk coupling. In generating the scatter plots in Fig. 22 we used the analytical expression in Lemma 6.2 for $\det \mathcal{M}$ to calculate \mathcal{Z} from (6.115). In Fig. 22 the HB boundaries for the various modes are shown.

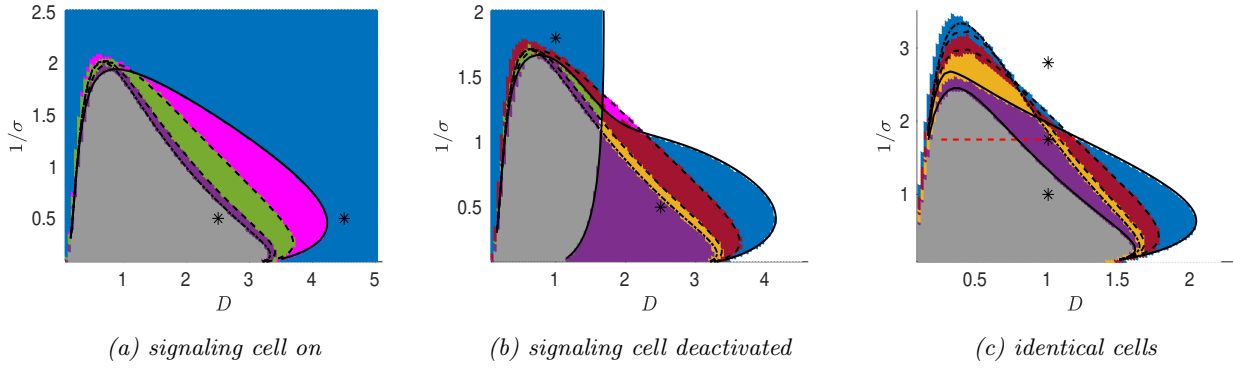


Figure 22: Scatter plots for the ring and center cell configuration of Fig. 5(c) with $r_c = 2$. The number of destabilizing eigenvalues \mathcal{Z} for the linearization of (1.5) around the steady-state solution is additionally coded as $\mathcal{Z} = 10$ (orange), $\mathcal{Z} = 12$ (purple) and $\mathcal{Z} = 14$ (gray). The HB boundaries are shown: dashed black curves are degenerate anti-phase modes, dot-dashed black curve is the sign-alternating anti-phase mode, and solid black curves are the HB modes where the center cell is active. Left: Identical ring cells have $d_{1r} = 0.8$, $d_{2r} = 0.2$ and $\alpha_r = 0.9$. The center cell is signaling with $d_{17} = 0.4$, $d_{27} = 0.2$ and $\alpha_7 = 0.5$. Middle: Same parameters as in the left panel except that the efflux from the center cell is increased to $d_{27} = 0.5$. The center cell is now deactivated. Right: All cells are identical with $d_{1r} = d_{17} = 0.4$, $d_{2r} = d_{27} = 0.2$ and $\alpha_r = \alpha_7 = 0.9$. Each cell would be in a quiescent state without any cell-cell coupling. The Kuramoto order parameter is computed on the red-dashed line.

Setting $\lambda = i\lambda_I$, the degenerate anti-phase HB modes occur on the black dashed curves, for which $\chi_1 = 0$ or $\chi_3 = 0$, the black dot-dashed curve corresponds to the sign-alternating anti-phase HB mode, for which $\chi_3 = 0$, while the solid black curves are the HB boundaries where the center cell is active, as obtained from setting $\chi_{\pm} = 0$. The slight raggedness in Fig. 22 shows that our winding number algorithm has some challenges in correctly calculating \mathcal{Z} very close to the HB boundaries where the eigenvalues associated with the degenerate anti-phase modes simultaneously cross the imaginary axis of the spectral plane.

In Fig. 23 we plot u_{2j} versus t at the star-labeled points in the scatter plots of Fig. 22, as computed using the algorithm of §5.4 with $\Delta t = 0.005$ and with uniformly random initial conditions of magnitude 0.1 about the steady-state. For $D = 2.5$ and $\sigma = 2$ in the scatter plot of Fig. 22(a) where all the modes are destabilizing, in Figs. 23(a)–23(b) we show that the ring cells synchronize on a wave packet solution and that large oscillations occur in the center signaling cell. By increasing D to $D = 4.5$, Fig. 23(c) shows that the ring cells now exhibit regular in-phase oscillations but with rather small amplitude. In contrast, when the center signaling cell has been deactivated, for the values $D = 2.5$ and $\sigma = 2$ in the scatter plot of Fig. 22(b) the results in Figs. 23(d)–23(e) show that the ring cells eventually synchronize to a rather large in-phase oscillation in comparison to that of the deactivated center cell. Observe from the HB boundaries in Fig. 22(b) that when $D = 2.5$ and $\sigma = 2$ only one of the two modes where the center cell is active is destabilizing. This is different than in Fig. 22(a) where, for $D = 2.5$ and $\sigma = 2$, both modes where the center cell are active are destabilizing. For the pair $D = 1$ and $\sigma = 5/9$ in Fig. 22(b) all anti-phase modes where the center cell is silent are linearly stable, while exactly one mode for which the center cell is not quiescent and the ring cells are in-phase is destabilizing. As expected, Fig. 23(f) shows that the center cell has much larger amplitude oscillations than do the ring cells, which oscillate in-phase. Finally, for identical cells that are all quiescent without cell-bulk coupling, the last row of Fig. 23 shows the intracellular dynamics at the three star-labeled points in Fig. 22(c). For $D = 1$ and $\sigma = 1$, Fig. 23(g) shows that all cells eventually oscillate in-phase and with a comparable amplitude. For $\sigma = 4/7$ (purple-shaded region in the scatter plot), where there are twelve destabilizing eigenvalues for the linearization of the steady-state, Fig. 23(h) shows that the ring cells have incoherent oscillations while the center cell has a small amplitude regular oscillation. When the degradation is decreased further to $\sigma = 5/14$, Fig. 23(i) shows that the amplitudes of the center cell and of the mixed-mode oscillations for the ring cells decay to their steady-state limits, as predicted by the scatter plot in Fig. 22(c).

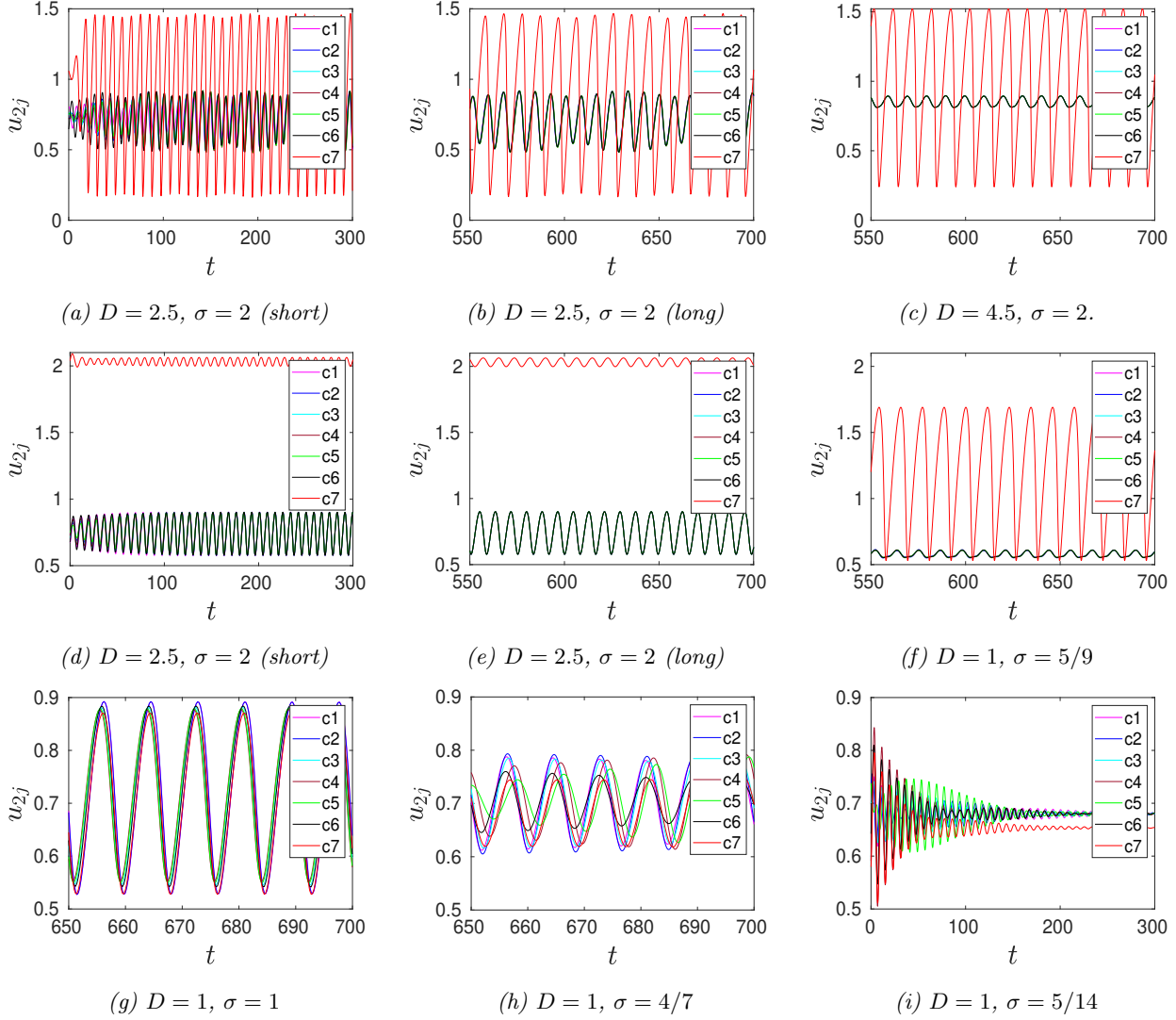


Figure 23: Intracellular dynamics $u_{2j}(t)$ for the ring and center cell configuration of Fig. 5(c) with $r_c = 2$ computed using the algorithm of §5.4 with $\Delta t = 0.005$ at the star-labeled points in Fig. 22 using uniformly random initial conditions of magnitude 0.1. The center cell is labeled as C7. Top row: Short- and long-time dynamics for $D = 2.5$ and $\sigma = 1$ in Fig. 22(a) is shown. A synchronous wave-packet solution emerges for the ring cells as t increases. For $D = 4.5$, the ring cells synchronize to a small amplitude regular oscillation. Middle row: For $D = 2.5$ and $\sigma = 2$ (left and middle) in Fig. 22(b) the multiple destabilizing anti-phase modes of the ring cells eventually synchronize to a periodic oscillation that is larger than that of the center cell. For $D = 1$ and $\sigma = 5/9$, the center cell now has much larger amplitude oscillations than do the ring cells. Bottom row: For the identical cells in Fig. 22(c) all cells exhibit roughly in-phase oscillations with a similar amplitude when $D = \sigma = 1$. For $D = 1$, but with a smaller bulk degradation $\sigma = 4/7$, the ring cells show large amplitude incoherent oscillations (middle). The center cell has a small amplitude regular oscillation. For the smaller value $\sigma = 5/14$, the mixed-mode oscillations in the ring cells and the regular oscillation of the center cell tend to their linearly stable steady-state values.

6.6 Measuring phase synchronization

For several cell configurations we now quantify the phase synchronization or coherence of intracellular oscillations based on the Kuramoto order parameter

$$Q(t) \equiv \frac{1}{N} \sum_{j=1}^N e^{i\theta_j}, \quad \text{where } \theta_j \equiv \arctan \left(\frac{u_{2j}(t) - u_{2js}}{u_{1j}(t) - u_{1js}} \right) \in (0, 2\pi). \quad (6.122)$$

Here u_{2js} and u_{1js} are the steady-state values obtained from (6.111). To safely disregard the effect of transients, we compute a time-averaged order parameter Q_{ave} , which we define by

$$Q_{ave} = \frac{1}{t_{up} - t_{low}} \int_{t_{low}}^{t_{up}} Q(t) dt, \quad (6.123)$$

and where we chose $t_{low} = 1300$ and $t_{up} = 1500$ for the simulations described below. To use our fast marching algorithm in §5.4 with $\Delta t = 0.005$ for the longer time interval $t \leq 1500$, we set $n = 114$, which gives 229 quadrature points for discretizing the Laplace space contour (see Tables 2 and 3).

For the ring with center cell configuration of identical cells, in Fig. 24 we plot Q_{ave} versus D along the parameter path $0.25 \leq D \leq 1.25$ with $\sigma = 4/7$ in the scatter plot in Fig. 22(c) (red-dashed path) for two choices of initial condition. For either choice of initial condition, we observe an apparent transition to complete phase coherence when D is near unity. This transition to phase coherence is further illustrated for $D = 0.75$, $D = 1$ and $D = 1.25$ in Fig. 25, where we plot the trajectories $u_{j2}(t)$ versus t on both short- and long-time intervals, as computed from our fast algorithm of §5.4. Overall, this example shows that a ring and center cell configuration, where each cell would be in a quiescent state without any cell-bulk coupling, can exhibit fully phase coherent intracellular oscillations due to the intercellular communication, as mediated by the bulk diffusion field, when the bulk diffusivity exceeds a threshold.

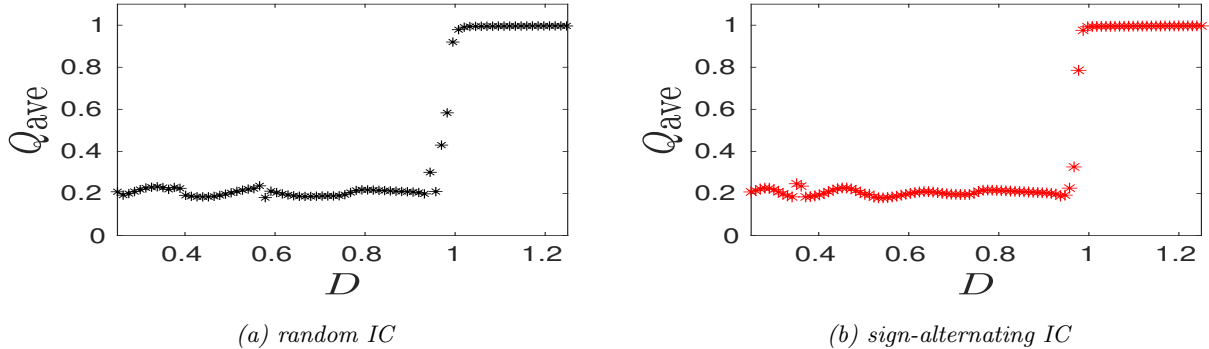


Figure 24: Averaged order parameter (6.123) for the ring and center cell configuration of identical cells in Fig. 5(c) along the red-dashed path in the scatter plot of Fig. 22(c) with $\sigma = 4/7$ and $0.25 < D < 1.25$. Black (left panel) and red (right panel) marked points are for either a uniformly random initial perturbation or a sign-alternating initial perturbation of the steady-state of magnitude 0.1. A transition to phase coherence occurs for D near unity for either choice of initial condition. Parameters: $r_c = 2$, $d_{1j} = 0.4$, $d_{2j} = 0.2$ and $\alpha_j = 0.9$ for $j \in \{1, \dots, 7\}$.

Next, we consider the two-ring configuration of cells shown in Fig. 26(a). For the rightmost ring, the cells are identical with $d_{1j} = 1.5$, $d_{2j} = 0.2$ and $\alpha_j = 0.9$ for $j \in \{1, \dots, 4\}$, and the cell centers are at $\mathbf{x}_1 = (4.5, 0)$, $\mathbf{x}_2 = (2.5, 2)$, $\mathbf{x}_3 = (0.5, 0)$ and $\mathbf{x}_4 = (2.5, -2)$. These cells are in a quiescent state when uncoupled from the bulk. For the leftmost ring, with cell centers at $\mathbf{x}_5 = (-0.5, 0)$, $\mathbf{x}_6 = (-1.5, 1)$, $\mathbf{x}_7 = (-2.5, 0)$ and $\mathbf{x}_8 = (-1.5, -1)$, the cells have identical permeabilities $d_{1j} = 0.4$ and $d_{2j} = 0.2$ for $j \in \{5, \dots, 8\}$, but are chosen to have distinct kinetic parameters $\alpha_5 = 0.6$, $\alpha_6 = 0.45$, $\alpha_7 = 0.4$ and $\alpha_8 = 0.5$. From Fig. 4, we observe that, when uncoupled from the bulk, these leftmost ring cells are activated and would have different frequencies of intracellular oscillations.

By using our fast algorithm of §5.4, numerical results for Q_{ave} , defined in (6.123), are given in Table 5 for various pairs of (D, σ) . For $\sigma = 1$, the intracellular dynamics are shown for three values of D

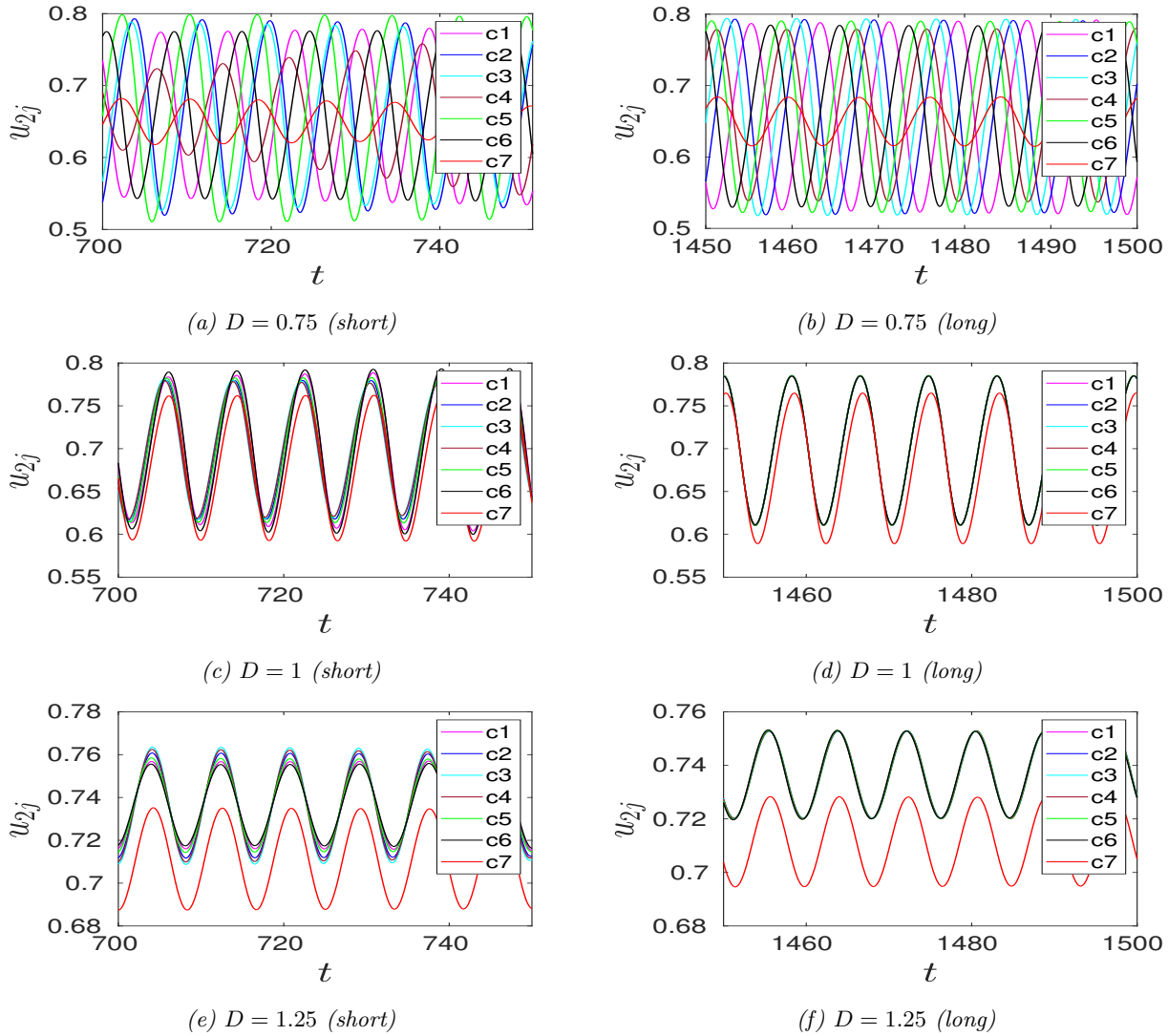


Figure 25: Intracellular dynamics $u_{2j}(t)$ for the ring and center cell configuration of Fig. 5(c) computed using the algorithm of §5.4 with $\Delta t = 0.005$ at three values of D along the red-dashed path in Fig. 22(c). Uniformly random initial conditions of magnitude 0.1 near the steady-state were used. The center cell is C7. Short- and long-time dynamics are shown. There is a transition to phase coherence near $D = 1$. Parameters as in Fig. 24.

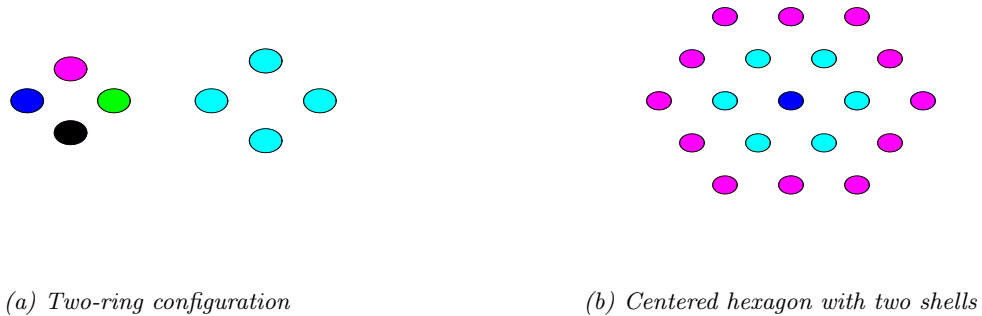


Figure 26: Left: Two non-concentric rings of cells, where the two rings have different radii. The rightmost ring has identical cells, while the other ring has cell-dependent parameters. Right: A centered hexagonal configuration of cells with two shells. Each shell has identical cells, while the center cell is the signaling or pacemaker cell.

in Fig. 27. We observe that an increase in the bulk diffusivity D has the dual effect of enhancing the phase coherence of the activated cells in the leftmost ring as well as for triggering large intracellular oscillations in the otherwise quiescent cells in the rightmost ring. Moreover, as σ decreases, there is a stronger intercellular communication via the bulk medium owing to the weaker spatial decay for the bulk species. As a result, a more pronounced phase coherence is expected when σ decreases. This trend is confirmed in Table 5.

D	Q_{ave}	
	$\sigma = 1$	$\sigma = 0.5$
0.5	0.329	0.427
1.0	0.419	0.540
2.0	0.496	0.624
5.0	0.596	0.826
10.0	0.763	0.875

Table 5: Averaged Kuramoto order parameter Q_{ave} from (6.123) for the two-ring configuration of Fig. 26(a) for various bulk diffusivities D when either $\sigma = 1$ or $\sigma = 0.5$. The IC's were the steady-state values. Phase coherence increases as D increases for fixed σ . Moreover, when the bulk degradation rate σ is smaller, the bulk signal has a weaker spatial decay and so is more able to enhance phase synchronization.

For our last numerical experiment we consider the centered hexagonal arrangement of cells shown in Fig. 26(b) that has two shells of cells and a center cell. The generators for this finite lattice are taken to be $\mathbf{l}_1 = \left(\left(\frac{4}{3} \right)^{1/4}, 0 \right)^T$ and $\mathbf{l}_2 = \left(\frac{4}{3} \right)^{1/4} \left(\frac{1}{2}, \frac{\sqrt{3}}{2} \right)^T$, so that the area $|\mathbf{l}_1 \times \mathbf{l}_2|$ of the primitive cell is unity.

We fix $d_{1j} = 0.8$ and $d_{2j} = 0.2$ for all cells, i.e. for $j \in \{1, \dots, 19\}$, and we set the bulk degradation rate as $\sigma = 1$. For the center cell we take $\alpha_1 = 0.5$, so that from Fig. 4 this cell is activated when uncoupled from the the bulk. For the cells on the inner and outer shells we take $\alpha_j = 0.7$ for $j \in \{2, \dots, 7\}$ and $\alpha_j = 0.8$ for $j \in \{8, \dots, 19\}$, respectively. These cells are quiescent when uncoupled from the bulk.

D	Q_{ave}	D	Q_{ave}
0.2	0.171	0.6	0.798
0.3	0.237	0.7	0.935
0.4	0.498	0.8	0.958
0.5	0.664	0.9	0.973

Table 6: Averaged Kuramoto order parameter Q_{ave} from (6.123) for the finite hexagonal lattice configuration of Fig. 26(b) for various bulk diffusivities D . Uniformly random IC's of magnitude 0.1 were used. The phase coherence increases significantly with D . Parameter values as in the caption of Fig. 28.

The numerical results for Q_{ave} in Table 6 show that the intracellular oscillations become increasingly phase-coherent as D increases. In Fig. 27 we plot $u_{j2}(t)$ versus t for three values of D as computed using our algorithm in §5.4 with $\Delta t = 0.005$, and with uniformly random initial conditions of magnitude 0.1. For $D = 0.3$, in Figs. 28(a)–28(b) we observe that the cells on each ring now oscillate with different amplitudes and phases, and that there is little phase coherence. However, upon increasing D to $D = 0.7$ for which $Q_{ave} = 0.935$, in Figs. 28(e)–28(f) we observe that cells on each of the two shells oscillate with a common amplitude and phase, and that there is only relatively minor phase differences between the intracellular oscillations on the two shells and the center cell. Overall, this example clearly show that a single activated cell at the center can trigger intracellular oscillations in the otherwise quiescent cells that form the inner and outer shells of a truncated lattice, and that the coherence of these oscillations increases strongly as the bulk diffusivity increases.

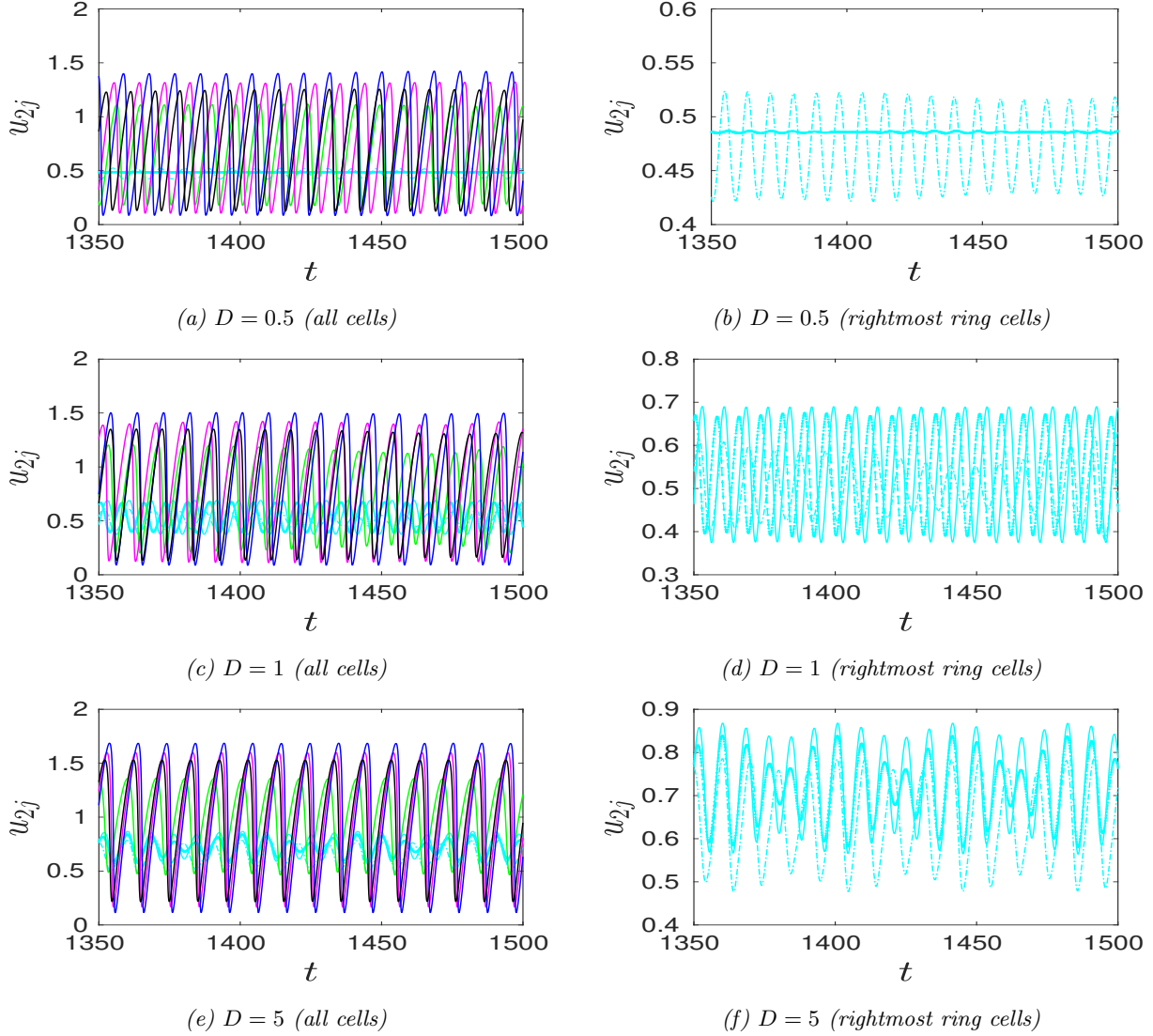


Figure 27: Intracellular dynamics $u_{2j}(t)$ for the two-ring configuration of cells in Fig. 26(a) computed using the algorithm of §5.4 with $\Delta t = 0.005$ for three values of D when $\sigma = 1$. The left panels show the dynamics in all the cells, identified according to the colors in Fig. 26(a). The right panels show the intracellular dynamics for the cells in the rightmost ring, where the solid cyan curve is for the rightmost cell \mathbf{x}_1 . With a counterclockwise orientation, solid-dashed, dashed-dotted and dotted curves identifies the dynamics in the cells \mathbf{x}_2 , \mathbf{x}_3 and \mathbf{x}_4 , respectively. Top row: For $D = 0.05$, the leftmost ring cells show little phase coherence (left panel), and the only cell in the rightmost ring that exhibits oscillations is \mathbf{x}_3 (which is the cell closest to the leftmost ring). Middle row: For $D = 1$ there is enhanced phase coherence in the leftmost ring cells, and all cells in the rightmost ring now have significant oscillations. Bottom row: For $D = 5$, the cells on the leftmost ring show significant phase coherence, while the rightmost ring cells exhibit in-phase mixed-mode oscillations. Parameter values are given in the text.

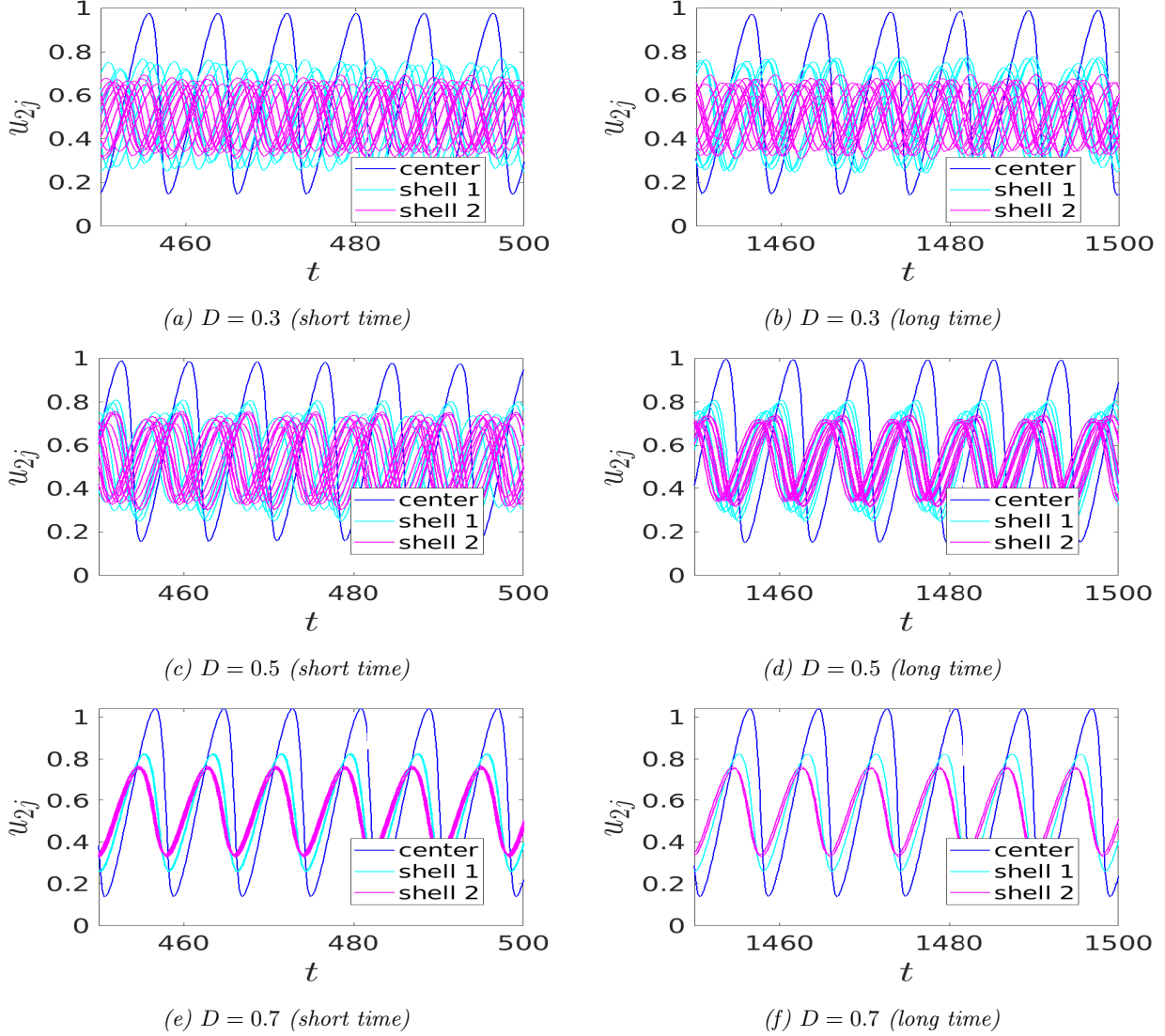


Figure 28: Short- (left panels) and long-time (right panels) intracellular dynamics $u_{2j}(t)$ for the finite lattice configuration in Fig. 26(b) as computed using the algorithm of §5.4 with $\Delta t = 0.005$ and for three values of D . The cell at the center and on the two shells are identified by the colours in Fig. 26(b). Only the center cell is activated when uncoupled from the bulk. Uniformly random IC of magnitude 0.1 around the steady-state intracellular values were given. Phase coherence increases substantially near $D = 0.5$. Parameters: $\sigma = 1$, $d_{1j} = 0.8$, $d_{2j} = 0.2$ for $j \in \{1, \dots, 19\}$, $\alpha_1 = 0.5$, $\alpha_j = 0.7$ for $j \in \{2, \dots, 7\}$ (inner shell) and $\alpha_j = 0.8$ for $j \in \{8, \dots, 19\}$ (outer shell).

7 Discussion

The hybrid asymptotic-numerical theory developed herein has provided new theoretical and computationally efficient approaches for studying how oscillatory dynamics associated with spatially segregated dynamically active “units” or “cells” are regulated by a PDE bulk diffusion field that is produced and absorbed by the entire cell population. For the cell-bulk model (1.5) we extended the strong localized perturbation theory, surveyed in [74], to a time-dependent setting in order to derive a new integro-differential ODE system that characterizes intracellular dynamics in a memory-dependent bulk-diffusion field. For this nonlocal system, a fast time-marching scheme, relying on the *sum-of-exponentials* method of [34] and [7], was developed to reliably numerically compute solutions over long time intervals.

For the special case of Sel’kov reaction kinetics, we have used our hybrid approach to investigate the effect that the influx and efflux permeability parameters, the bulk degradation rate and bulk diffusivity, and the reaction-kinetic parameters have in both triggering intracellular oscillations and in mediating oscillator synchronization for the entire collection of cells. Quorum- and diffusion-sensing behavior were illustrated for various cell configurations. Comparisons of numerical results from our fast time-marching algorithm for the integro-differential ODE system with the numerical results for the full cell-bulk system (1.5) computed using the commercial solver FlexPDE [18] have shown that our hybrid asymptotic-numerical theory accurately reproduces, within roughly a minute of CPU time on a laptop, the intricate mixed-mode oscillatory dynamics that can occur for the full system (1.5) over long-time intervals. From a computation of the Kuramoto order parameter, we have exhibited an apparent phase transition to complete phase coherence for a hexagonal arrangement of identical cells (see Fig. 24). These cells would not exhibit intracellular oscillations without any inter-cell coupling. Moreover, in Fig.28 we have shown that a single pacemaker or signaling cell can trigger intracellular oscillations for all cells on a truncated lattice, and that these oscillations become increasingly phase-coherent as the bulk diffusivity increases.

Although we have only illustrated and benchmarked our theory for a moderate number of cells, with our fast time-marching scheme, possibly applied to Fitzhugh-Nagumo kinetics, it is viable numerically to compute target or spiral wave patterns of oscillatory dynamics, or to seek to identify chimera states, associated with a large $N \geq 100$ collection of cells. We emphasize that our integro-differential ODE system can also be used for specific multi-component reaction kinetics such as those modeling the initiation and synchronization of glycolysis oscillations (see [29] for a recent survey) or for those modeling quorum-sensing transitions between bistable states that are believed to be responsible for bioluminescence phenomena for the marine bacterium *Aliivibrio fischeri* (cf. [67], [45], [59] see also the references therein).

Moreover, our new theoretical and computational approaches for first deriving and then computing solutions to integro-differential systems of ODE’s for cell-bulk models with one diffusing species can readily be extended to \mathbb{R}^3 and to the case of finite domains $\Omega \in \mathbb{R}^d$ with $d \in \{1, 2, 3\}$. In a 1-D setting, steady-states and their linear stability properties for cell-bulk models consisting of discrete oscillators located at either the domain boundaries or at interior points in the domain, and which are coupled by a bulk diffusion field, have been studied in [23], [22] and [51] (see also the references therein). Our approach is also readily extended to cell-bulk models with two bulk diffusing species, such as in [54] and [53], where the focus was mainly on describing bifurcation and pattern-formation properties of the model. Cell-bulk models, allowing for a spatially uniform bulk drift velocity, such as in [73], should also be tractable to analyze with our approach. The main two features that we require to derive the fast time-marching algorithm are an exact analytical representation of the Laplace-transformed bulk diffusion field and that this representation has singularities only along the negative real axis in the Laplace transform space. These properties are inherent for Green’s functions for heat-type equations with bulk degradation in either bounded or unbounded domains.

Finally, we discuss three numerical challenges that warrant further investigation. Firstly, the primary numerical errors in our time-marching scheme of §5.4 are due to the ETD2 discretization of the Duhamel integrals as well as the Forward-Euler discretization in (5.104) for the dynamics. By increasing the truncation order of this aspect of our algorithm it should be possible to take larger time steps than we have done while still preserving a comparable level of accuracy. Secondly, the computation of

roots of $\det \mathcal{M}(\lambda) = 0$ for the GCEP in (4.64b), which determines the HB boundaries and oscillation frequencies near the steady-state, becomes highly challenging when the number of cells becomes large. As a result, efficient numerical methods to compute path-dependent solutions to nonlinear matrix eigenvalue problems that are complex-symmetric, but non-Hermitian, are required. Finally, the computation of the winding number in (6.115) for an arbitrary cell configuration with a large number of cells is highly challenging as there is typically no analytical expression for $\det \mathcal{M}(\lambda)$. To overcome this difficulty, a Takagi factorization (cf. [31]) of the complex symmetric matrix $\mathcal{M}(\lambda)$ that smoothly depends on a bifurcation parameter may provide a numerically well-conditioned approach to compute the winding number (cf. [16]).

Appendix A Non-dimensionalization of the cell-bulk model

We summarize the non-dimensionalization of (1.4) into the form (1.5). Labeling $[\gamma]$ as the dimensions of the variable γ , we have

$$\begin{aligned} [\mathcal{U}] &= \frac{\text{moles}}{(\text{length})^2}, & [\mu_j] &= \text{moles}, & [\mu_c] &= \text{moles}, & [D_B] &= \frac{(\text{length})^2}{\text{time}}, \\ [k_B] = [k_R] &= \frac{1}{\text{time}}, & [\beta_1] &= \frac{\text{length}}{\text{time}}, & [\beta_2] &= \frac{1}{\text{length} \times \text{time}}, \end{aligned} \quad (\text{A.1})$$

for the dimensions of the terms in (1.4). We introduce the dimensionless variables t , \mathbf{x} , U and \mathbf{u} as

$$t = k_R T, \quad \mathbf{x} = \mathbf{X}/L, \quad U = L^2 \mathcal{U}/\mu_c, \quad \mathbf{u}_j = \mu_j/\mu_c, \quad \text{where } L \equiv \min_{i \neq j} |\mathbf{x}_i - \mathbf{x}_j|. \quad (\text{A.2})$$

We define the small parameter $\varepsilon = R_0/L$ where R_0 is the common cell radius. By noting that $dS_{\mathbf{x}} = L dS_{\mathbf{x}}$, we readily obtain (1.5) where the dimensionless parameters are defined in (1.6).

Appendix B Long-Time Dynamics of the Transient solution

We follow [41] and summarize some results for inverting the Laplace transform in (2.9a). We first define $\hat{H}(s) \equiv 1/[s \log s]$, with a branch cut along the negative real axis. To determine $H(\tau) = \mathcal{L}^{-1}[\hat{H}]$ we integrate over a Bromwich contour

$$H(\tau) = \frac{1}{2\pi i} \int_{c-i\infty}^{c+i\infty} \frac{e^{s\tau}}{s \log s} ds, \quad \text{where } c > 1.$$

By calculating the residue at the simple pole $s = 1$ and from deforming the integration path we obtain

$$H(\tau) = e^\tau + \frac{1}{2\pi i} \int_0^\infty \left(\frac{e^{-\xi\tau}}{\xi (\log \xi + i\pi)} - \frac{e^{-\xi\tau}}{\xi (\log \xi - i\pi)} \right) d\xi,$$

where the two integrand terms represent contributions from the top and the bottom of the branch cut along the negative real axis. In this way, we obtain the identity

$$N(\tau) \equiv \int_0^\infty \frac{e^{-\tau\xi}}{\xi [\pi^2 + (\log \xi)^2]} d\xi = e^\tau - H(\tau), \quad (\text{B.3})$$

where $N(\tau)$ is Ramanujan's integral. By taking the Laplace transform of (B.3) we obtain the identity

$$\hat{N}(s) = \frac{1}{s-1} - \frac{1}{s \log s}.$$

Upon using $\log s \sim (s-1) - (s-1)^2/2$ as $s \rightarrow 1$, we get $\hat{N}(s) \sim 1/2$ as $s \rightarrow 1$, so that $s = 1$ is a removable singularity for \hat{N} . Therefore, \hat{N} is analytic in $\text{Re}(s) > 0$ and satisfies $\hat{N}(s) \sim -[s \log s]^{-1} + \mathcal{O}(1)$ as $s \rightarrow 0$. By the scaling relation $\mathcal{L}[N(\tau/c)] = c\hat{N}(cs)$ for the Laplace transform with $c = \kappa_{0j} > 0$, we obtain (2.10).

Appendix C Improved approximation for $B_j(\Delta t)$

For $u_{1j}(0) \neq 0$, we derive the approximation $B_j(\Delta t)$ in (5.100) that is an improvement of that given in (3.39).

By substituting $D_j(\Delta t)$ and $C_{jk}(\Delta t)$ from (5.90a) and (5.98a) into (5.71), we obtain

$$[E_1(\sigma\Delta t) - \eta_j] B_j(\Delta t) = \gamma_j u_{1j}(\Delta t) - I + \sum_{k \neq j}^N B_k(\Delta t) E_1(a_{jk}^2/\Delta t), \quad \text{for } j \in \{1, \dots, N\}, \quad (\text{C.4})$$

where

$$I \equiv \int_0^{\Delta t} (B_j(\Delta t) - B_j(\Delta t - z)) \frac{e^{-\sigma z}}{z} dz. \quad (\text{C.5})$$

We let $\Delta t \ll 1$, and use $E_1(\sigma\Delta t) = -\log(\sigma\Delta t) - \gamma_e + \mathcal{O}(\Delta t)$, and neglect the last term on the right-hand side of (C.4) since $E_1(z)$ is exponentially small for $z \gg 1$. This yields that

$$B_j(\Delta t) = -\frac{u_{1j}(\Delta t)\gamma_j}{\log(\Delta t/(\kappa_j e^{-\gamma_e}))} + \frac{I}{\log(\Delta t/(\kappa_j e^{-\gamma_e}))}, \quad (\text{C.6})$$

where we used $\sigma e^{\eta_j} = 1/\kappa_j$. Upon substituting the two-term expansion for $B_j(\Delta t)$, given by

$$B_j(\Delta t) = \frac{c_j}{\log(\Delta t/(\kappa_j e^{-\gamma_e}))} + \frac{d_j}{[\log(\Delta t/(\kappa_j e^{-\gamma_e}))]^2}, \quad (\text{C.7})$$

with $c_j = -u_{1j}(\Delta t)\gamma_j$ into (C.6) and (C.5), we determine d_j as

$$d_j = c_j \int_0^{\Delta t} \frac{\log(1 - z/\Delta t) e^{-\sigma z}}{z \log((\Delta t - z)/(\kappa_j e^{-\gamma_e}))} dz = c_j \int_0^1 \frac{\log(1 - \xi) e^{-\sigma \xi \Delta t}}{\xi \log\left(\frac{\Delta t}{\kappa_j e^{-\gamma_e}}(1 - \xi)\right)} d\xi. \quad (\text{C.8})$$

By using $e^{-\sigma \xi \Delta t} \approx 1$ and $|\log(\Delta t/(\kappa_j e^{-\gamma_e}))| \gg 1$, we obtain for $\Delta t \ll 1$ that

$$d_j \sim \frac{c_j}{\log\left(\frac{\Delta t}{\kappa_j e^{-\gamma_e}}\right)} \int_0^1 \frac{\log(1 - \xi)}{\xi} d\xi. \quad (\text{C.9})$$

Using $\int_0^1 \xi^{-1} \log(1 - \xi) d\xi = -\pi^2/6$, we substitute (C.9) and $c_j = -u_{1j}(\Delta t)\gamma_j$ into (C.7) to get (5.100).

Appendix D An artificial boundary condition for full PDE simulations

To numerically solve the cell-bulk system (1.5) using FlexPDE 6.50 [18], we must truncate \mathbb{R}^2 by both choosing and formulating a boundary condition on a confining boundary $\partial\Omega$ that encloses all of the cells.

For the full PDE computations shown in Fig. 9 and Fig. 13 we chose the artificial boundary $\partial\Omega$ to have approximately the same shape as the asymptotic levels sets of the steady-state solution away from the two cells. Assuming that the solution is approximately radially symmetric due to the cell arrangement with center of mass at $\mathbf{x}_c = \mathbf{0}$, we took $\Omega = \{\mathbf{x} \in \mathbb{R}^2 \mid |\mathbf{x}| \leq R_a\}$ with $R_a \gg 1$. The steady-state far away from the asymptotic support of the two cells satisfies $\Delta U_s - \omega^2 U_s \approx C_1 \delta(\mathbf{x})$, for some C_1 where $\omega \equiv \sqrt{\sigma/D}$. This yields the asymptotic behavior $U_s = C_2 K_0(\omega|\mathbf{x}|)$ where $C_2 = -C_1/(2\pi)$. Upon using $K_0(z) \sim \sqrt{\pi/2} z^{-1/2} e^{-z} (1 + \mathcal{O}(z^{-1}))$ for $z \gg 1$, we let $r = |\mathbf{x}|$, and readily calculate

$$\frac{d}{dr} U_s \sim -\left(\omega + \frac{1}{2r}\right) U_s + \mathcal{O}\left(\frac{1}{r^2}\right) U_s, \quad \text{for } r \gg 1.$$

Neglecting the $\mathcal{O}(r^{-2})$ term, the artificial boundary condition that we imposed in our FlexPDE simulations, which asymptotically approximates the steady-state on \mathbb{R}^2 , was

$$\partial_r U(r, t) = - \left(\omega + \frac{1}{2r} \right) U(r, t) \quad \text{on} \quad r = R_a, \quad (\text{D.10})$$

where $\omega = \sqrt{\sigma/D}$. We chose $R_a = 6$ for the results shown in Fig. 9 and Fig. 13.

More sophisticated, memory-dependent, artificial boundary conditions for parabolic PDE problems have been formulated in [65]. However, owing to the very close agreement between our asymptotic and FlexPDE results using (D.10), we did not find it essential to implement the approach in [65].

Acknowledgments

Merlin Pelz was partially supported by a UBC Four-Year Doctoral Fellowship. Michael Ward gratefully acknowledges the support of the NSERC Discovery Grant Program.

References

- [1] M. Abramowitz and I. Stegun. *Handbook of mathematical functions, with formulas, graphs and mathematical tables*. Dover Publications, NY, USA, 1974.
- [2] J. A. Acebrón, L. Bonilla, C. J. Vicente, F. Ritort, and Renato Spigler. The Kuramoto model: A simple paradigm for synchronization phenomena. *Rev. of Modern Phys.*, 77(1):137, 2005.
- [3] D. Alciatore and R. Miranda. A winding number and point-in-polygon algorithm. *Glaxo Virtual Anatomy Project Research Report, Department of Mechanical Engineering, Colorado State University*, 1995.
- [4] R. P. Aristides and R. L. Viana. An integro-differential equation for dynamical systems with diffusion-mediated coupling. *Nonlinear Dynamics*, 100(4):3759–3770, 2020.
- [5] T. Betcke, N. G. Higham, V. Mehrmann, G. M. N. Porzio, C. Schröder, and Tisseur F. NLEVP: A collection of nonlinear eigenvalue problems. users’ guide. *MIMS EPring 2011.117, Manchester Institute for Mathematical Sciences, The University of Manchester, UK*, page 10 pages, 2019.
- [6] T. Betcke, N. G. Higham, V. Mehrmann, C. Schröder, and Tisseur F. NLEVP: A collection of nonlinear eigenvalue problems. *ACM Trans. Math. Software*, 39(2):7.1–7.28, 2013.
- [7] G. Beylkin and L. Monzón. On approximation of functions by exponential sums. *Appl. and Comput. Harm. Anal.*, 19(1):17–48, 2005.
- [8] G. Beylkin and L. Monzón. Approximation by exponential sums revisited. *Appl. and Comput. Harm. Anal.*, 28(2):131–140, 2010.
- [9] C. J. Bouwkamp. Note on an asymptotic expansion. *Indiana U. Math. J.*, 21:547–549, 1971.
- [10] M. Breakspear, S. Heitmann, and A. Daffertshofer. Generative models of cortical oscillations: neurobiological implications of the Kuramoto model. *Frontiers in human neuroscience*, 4:190, 2010.
- [11] B. M Czajkowski, C. A. S. Batista, and R. L. Viana. Synchronization of phase oscillators with chemical coupling: Removal of oscillators and external feedback control. *Physica A*, 610:128418, 2023.
- [12] J. D. Da Fonseca and C. V. Abud. The Kuramoto model revisited. *J. Stat. Mech.: Theory and Experiment*, 2018(10):103204, 2018.

- [13] S. Danø, M. F. Madsen, and P. G. Sørensen. Quantitative characterization of cell synchronization in yeast. *Proceedings of the National Academy of Sciences*, 104(31):12732–12736, 2007.
- [14] S. Danø, P. G. Sørensen, and F. Hynne. Sustained oscillations in living cells. *Nature*, 402(6759):320–322, 1999.
- [15] S. De Monte, F. d’Ovidio, S. Danø, and P. G. Sørensen. Dynamical quorum sensing: Population density encoded in cellular dynamics. *Proceedings of the National Academy of Sciences*, 104(47):18377–18381, 2007.
- [16] L. Dieci, A. Papini, and A. Pugliese. Takagi factorization of matrices depending on parameters and locating degeneracies of singular values. *SIAM J. Matrix Analysis*, 43(3):1148–1161, 2022.
- [17] G. M. Dunny and B. Leonard. Cell-cell communication in gram-positive bacteria. *Annual Rev. Microbiology*, 51(1):527–564, 1997.
- [18] PDE FlexPDE. Solutions inc. URL <http://www.pdesolutions.com>, 2015.
- [19] A. Goldbeter. *Biochemical oscillations and cellular rhythms: the molecular bases of periodic and chaotic behaviour*. Cambridge University Press, 1997.
- [20] D. Gomez, S. Iyaniwura, F. Paquin-Lefebvre, and M. J. Ward. Pattern forming systems coupling linear bulk diffusion to dynamically active membranes or cells. *Phil. Trans. Roy. Soc. A.*, 379:20200276, 2021.
- [21] A. Gomez-Marin, J. Garcia-Ojalvo, and J. M. Sancho. Self-sustained spatiotemporal oscillations induced by membrane-bulk coupling. *Phys. Rev. Lett.*, 98:168303, Apr 2007.
- [22] J. Gou, W.-Y. Chiang, P.-Y. Lai, M. J. Ward, and Y.-X. Li. A theory of synchrony by coupling through a diffusive chemical signal. *Physica D*, 339:1–17, 2017.
- [23] J. Gou, Y. X. Li, W. Nagata, and M. J. Ward. Synchronized oscillatory dynamics for a 1-D model of membrane kinetics coupled by linear bulk diffusion. *SIAM J. Appl. Dyn. Sys.*, 14(4):2096–2137, 2015.
- [24] J. Gou and M. J. Ward. An asymptotic analysis of a 2-D model of dynamically active compartments coupled by bulk diffusion. *Journal of Nonlinear Science*, 26(4):979–1029, 2016.
- [25] J. Gou and M. J. Ward. Oscillatory dynamics for a coupled membrane-bulk diffusion model with Fitzhugh-Nagumo kinetics. *SIAM J. Appl. Math.*, 76(2):776–804, 2016.
- [26] T. Gregor, K. Fujimoto, N. Masaki, and S. Sawai. The onset of collective behavior in social amoebae. *Science*, 328(5981):1021–1025, 2010.
- [27] J. Grzybowski, E. Macau, and T. Yoneyama. On synchronization in power-grids modelled as networks of second-order Kuramoto oscillators. *Chaos: An Interdisciplinary J. of Nonlin. Sci*, 26(11), 2016.
- [28] S. Güttel and F. Tisseur. The nonlinear eigenvalue problem. *Acta Numerica*, 26(1):1–94, 2017.
- [29] M. J. B. Hauser. Synchronization of glycolytic activity in yeast cells. *Curr. Genet.*, 68(1):69–81, 2022.
- [30] B. A. Hense, C. Kuttler, J. Müller, M. Rothballer, A. Hartmann, and J. U. Kreft. Does efficiency sensing unify diffusion and quorum sensing? *Nature Reviews. Microbiology*, 5:230–239, 2007.
- [31] R. Horn and C. Johnson. *Matrix Analysis*. Cambridge University Press, 1985.

- [32] S. Iyaniwura and M. J. Ward. Localized signaling compartments in 2-D coupled by a bulk diffusion field: Quorum sensing and synchronous oscillations in the well-mixed limit. *Europ. J. Appl. Math.*, 32(5):1001–1031, 2021.
- [33] S. Iyaniwura and M. J. Ward. Synchrony and oscillatory dynamics for a 2-d PDE-ODE model of diffusion-mediated communication between small signaling compartments. *SIAM J. Appl. Dyn. Sys.*, 20(1):438–499, 2021.
- [34] S. Jiang, L. Greengard, and S. Wang. Efficient sum-of-exponentials approximations for the heat kernel and their applications. *Adv. Comput. Math.*, 41:529–551, 2015.
- [35] Y. Kuramoto. International symposium on mathematical problems in theoretical physics. In H. Arakai, editor, *Lecture Notes in Physics*, p. 420, volume 39. Springer, New York, NY, 1975.
- [36] Y. Kuramoto. *Chemical oscillations, waves, and turbulence*. Springer-Verlag, New York, 1984.
- [37] Y. Kuramoto. Scaling behavior of turbulent oscillators with non-local interaction. *Progress of Theoretical Physics*, 94(3):321–330, 1995.
- [38] Y. Kuramoto and H. Nakao. Phase reduction approach to synchronisation of nonlinear oscillators. *Contemporary Physics*, 57(2):188–214, 2015.
- [39] Y. Kuramoto and H. Nakao. On the concept of dynamical reduction: the case of coupled oscillators. *Phil. Trans. R. Soc. A.*, 377, 20190041.
- [40] H. Levine and W. J. Rappel. Membrane-bound Turing patterns. *Phys. Rev. E*, 72(6):061912, 2005.
- [41] S. G. Llewellyn Smith. The asymptotic behavior of Ramanujan’s integral and its application to two-dimensional diffusion-like equations. *Europ. J. Appl. Math.*, 11:13–28, 2000.
- [42] M. López-Fernández, C. Lubich, and A. Schädle. Adaptive, fast, and oblivious convolution in evolution equations with memory. *SIAM J. Sci. Comput.*, 30(2):1015–1037, 2008.
- [43] M. López-Fernández and C. Palencia. On the numerical inversion of the Laplace transform of certain holomorphic mappings. *Applied Numer. Math.*, 51(2-3):289–303, 2004.
- [44] M. López-Fernández, C. Palencia, and A. Schädle. A spectral order method for inverting sectorial Laplace transforms. *SIAM J. Numer. Anal.*, 44(3):1332–1350, 2006.
- [45] P. Melke, P. Sahlin, A. Levchenko, and H. Jonsson. A cell-based model for quorum sensing in heterogeneous bacterial colonies. *PLoS Computational Biology*, 6(6):e1000819, 2010.
- [46] J. Müller, C. Kuttler, B. A. Hense, M. Rothballer, and A. Hartmann. Cell–cell communication by quorum sensing and dimension-reduction. *Journal of Mathematical Biology*, 53(4):672–702, 2006.
- [47] J. Müller and H. Uecker. Approximating the dynamics of communicating cells in a diffusive medium by odes—homogenization with localization. *Journal of Mathematical Biology*, 67(5):1023–1065, 2013.
- [48] H. Nakao. Anomalous spatio-temporal chaos in a two-dimensional system of nonlocally coupled oscillators. *Chaos*, 9(4):902–909, 1999.
- [49] H. Nakao. Phase reduction approach to synchronisation of nonlinear oscillators. *Contemporary Physics*, 57(2):188–214, 2015.
- [50] V. Nanjundiah. Cyclic AMP oscillations in Dictyostelium Discoideum: Models and observations. *Biophysical chemistry*, 72(1-2):1–8, 1998.

- [51] F. Paquin-Lefebvre, W. Nagata, and M. J Ward. Pattern formation and oscillatory dynamics in a two-dimensional coupled bulk-surface reaction-diffusion system. *SIAM J. Appl. Dyn. Sys.*, 18(3):1334–1390, 2019.
- [52] F. Paquin-Lefebvre, W. Nagata, and M. J Ward. Pattern formation and oscillatory dynamics in a two-dimensional coupled bulk-surface reaction-diffusion system. *SIAM J. Appl. Math.*, 80(3):1520–1545, 2020.
- [53] M. Pelz and M. J. Ward. The emergence of spatial patterns for compartmental reaction kinetics coupled by two bulk diffusing species with comparable diffusivities. *Philosophical Transactions of the Royal Society A*, 381(2245):20220089, 2023.
- [54] M. Pelz and M. J. Ward. Symmetry-breaking bifurcations for compartmental reaction kinetics coupled by two bulk diffusing species with comparable diffusivities in 2-d. *Frontiers in Applied Mathematics and Statistics*, 9:1110497, 2023.
- [55] J. Pérez-Velázquez, M. Gölgeli, and R. García Contreras. Mathematical modelling of bacterial quorum sensing: a review. *Bull. Math. Bio.*, 78:1585–1639, 2016.
- [56] B. Pietras and A. Daffertshofer. Network dynamics of coupled oscillators and phase reduction techniques. *Physics Reports*, 819:1–105, 2019.
- [57] M. Raab, J. Zeininger, Y. Suchorski, K. Tokuda, and G. Ruppachter. Emergence of chaos in a compartmentalized catalytic reaction nanosystem. *Nature Communications*, 14:736, 2023.
- [58] E. M. Rauch and M. Millonas. The role of trans-membrane signal transduction in Turing-type cellular pattern formation. *J. Theor. Biol.*, 226:401–407, 2004.
- [59] W. Ridgway, M. J. Ward, and B. T. Wetton. Quorum-sensing induced transitions between bistable steady-states for a cell-bulk ODE-PDE model with Lux intracellular kinetics. *J. Math. Bio.*, 84(1-2), 2021.
- [60] D. J. Schwab, A. Baetica, and P. Mehta. Dynamical quorum-sensing in oscillators coupled through an external medium. *Physica D*, 241(21):1782–1788, 2012.
- [61] E. E. Sel’kov. Self-oscillations in glycolysis 1. a simple kinetic model. *European Journal of Biochemistry*, 4(1):79–86, 1968.
- [62] K. Showalter and I. R. Epstein. From chemical systems to systems chemistry: Patterns in space and time. *Chaos*, 25:097613, 2015.
- [63] F. A. Silva, S. R. Lopes, and R. L. Viana. Synchronization of biological clock cells with a coupling mediated by the local concentration of a diffusing substance. *Commun. Nonlinear Sci Numer. Simulat.*, 35:37–52, 2016.
- [64] S. H. Strogatz. From Kuramoto to Crawford: exploring the onset of synchronization in populations of coupled oscillators. *Physica D*, 143:1–20, 2000.
- [65] A. Y. Suhov and A. Ditkowski. Artificial boundary conditions for the simulation of the heat equation in an infinite domain. *SIAM J. Sci. Comput.*, 33:1765–1784, 2011.
- [66] E. Süli and D. Mayers. *An Introduction to Numerical Analysis*. Cambridge University Press, 2003.
- [67] M. E. Taga and B. L. Bassler. Chemical communication among bacteria. *Proceedings of the National Academy of Sciences*, 100(suppl 2):14549–14554, 2003.
- [68] A. F. Taylor, M. Tinsley, and K. Showalter. Insights into collective cell behavior from populations of coupled chemical oscillators. *Phys. Chemistry Chem Phys.*, 17(31):20047–20055, 2015.

- [69] A. F. Taylor, M. Tinsley, F. Wang, Z. Huang, and K. Showalter. Dynamical quorum sensing and synchronization in large populations of chemical oscillators. *Science*, 323(5914):614–6017, 2009.
- [70] M. R. Tinsley, A. F. Taylor, Z. Huang, and K. Showalter. Emergence of collective behavior in groups of excitable catalyst-loaded particles: Spatiotemporal dynamical quorum sensing. *Phys. Rev. Lett.*, 102:158301, 2009.
- [71] M. R. Tinsley, A. F. Taylor, Z. Huang, F. Wang, and K. Showalter. Dynamical quorum sensing and synchronization in collections of excitable and oscillatory catalytic particles. *Physica D*, 239(11):785–790, 2010.
- [72] N. Tompkins, N. Li, C. Girabwe, and S. Fraden. Testing Turing’s theory of morphogenesis in chemical cells. *PNAS*, 111(12):4397–4402, 2014.
- [73] H. Uecker, J. Müller, and B. A. Hense. Individual-based model for quorum sensing with background flow. *Bulletin of Mathematical Biology*, 76(7):1727–1746, 2014.
- [74] M. J Ward. Spots, traps, and patches: Asymptotic analysis of localized solutions to some linear and nonlinear diffusive systems. *Nonlinearity*, 31(8):R189, 2018.
- [75] M. Wyman and R. Wong. The asymptotic behavior of $\mu(z, \beta, \alpha)$. *Canad. J. Math.*, 21:1013–1023, 1969.
- [76] B. Xu and P. Bressloff. A PDE-DDE model for cell polarization in fission yeast. *SIAM J. Appl. Math.*, 76(3):1844–1870, 2016.